

# Isogeometric fluid-structure interaction: theory, algorithms, and computations

Y. Bazilevs · V. M. Calo · T. J. R. Hughes · Y. Zhang

Received: 25 May 2008 / Accepted: 16 June 2008 / Published online: 6 August 2008  
© Springer-Verlag 2008

**Abstract** We present a fully-coupled monolithic formulation of the fluid-structure interaction of an incompressible fluid on a moving domain with a nonlinear hyperelastic solid. The arbitrary Lagrangian–Eulerian description is utilized for the fluid subdomain and the Lagrangian description is utilized for the solid subdomain. Particular attention is paid to the derivation of various forms of the conservation equations; the conservation properties of the semi-discrete and fully discretized systems; a unified presentation of the generalized- $\alpha$  time integration method for fluid-structure interaction; and the derivation of the tangent matrix, including the calculation of shape derivatives. A NURBS-based isogeometric analysis methodology is used for the spatial discretization and three numerical examples are presented which demonstrate the good behavior of the methodology.

**Keywords** Blood flow · Cardiovascular modeling · Fluid-structure interaction · Hyperelastic solids · Incompressible fluids · Isogeometric analysis · Mesh movement · Moving domains · NURBS · Shape derivatives · Space-time Piola transformation

---

Y. Bazilevs (✉)  
Department of Structural Engineering,  
University of California, San Diego  
9500 Gilman Drive, La Jolla, CA 92093, USA  
e-mail: bazily@ices.utexas.edu

V. M. Calo · T. J. R. Hughes  
Institute for Computational Engineering and Sciences,  
The University of Texas at Austin, 201 East 24th Street,  
1 University Station C0200, Austin, TX 78712, USA

Y. Zhang  
Mechanical Engineering, Carnegie Mellon University, Scalfe Hall  
303, 5000 Forbes Avenue, Pittsburgh, PA 15213, USA

## Contents

1	Introduction	3
2	Conservation laws on moving domains	5
2.1	Space-time mapping and Piola transform	5
2.2	Master balance laws	7
2.3	Discussion of discretization choices for balance laws on moving domains	8
2.4	Specific forms of solid and fluid equations	10
3	Variational formulation of the coupled fluid-structure interaction problem at the continuous level	11
3.1	Solid problem	12
3.2	Motion of the fluid subdomain	12
3.3	Fluid problem	13
3.4	Coupled problem	13
4	Formulation of the fluid-structure interaction problem at the discrete level	14
4.1	Approximation spaces and enforcement of kinematic compatibility conditions	14
4.2	Semi-discrete problem	15
4.3	Discussion of conservation	16
4.4	Time integration of the fluid-structure interaction system	17
5	Linearization of the fluid-structure interaction equations: a methodology for computing shape derivatives	19
6	NURBS-based isogeometric analysis	23
7	Numerical examples: selected benchmark computations	23
7.1	Flow over an elastic beam attached to a fixed square block	23
7.2	Inflation of a balloon	24
8	Computation of vascular flows	26
8.1	Construction of the arterial geometry	26
8.2	Investigation of the solid model for a range of physiological stresses	29
8.3	Flow in a patient-specific abdominal aortic aneurysm	30
9	Conclusions	32
	Appendix A: A note on exterior calculus	33

## 1 Introduction

There are two major classes of discrete fluid-structure interaction (FSI) formulations: *staggered* and *monolithic*, which

are also referred to as loosely- and strongly-coupled, respectively.

In staggered approaches, the fluid, solid and mesh movement equations are solved sequentially, in uncoupled fashion. This enables the use of existing well-validated fluid and structural solvers, a significant motivation for adopting this approach. In addition, for many problems the staggered approach works well and is very efficient. However, difficulties in the form of lack of convergence have been noted in a number of situations and considerable recent literature has been devoted to a discussion of these problems and attempts to circumvent them. It seems that “light” structures interacting with “heavy” fluids are particularly problematic (see, e.g., [50, 52, 53]). Another situation that has proved difficult is when an *incompressible* fluid region is fully contained by a solid, such as for the filling of a balloon with water [42]. In cases like this, special modifications need to be introduced to achieve success. On the other hand, Farhat et al. [18] has reported consistent success for staggered approaches to *compressible* fluids. As of this writing, these claims have not been fully reconciled with those for incompressible fluids. It is somewhat puzzling because incompressible flows may be thought of as limiting phenomena within a compressible formulation.

In monolithic approaches, the fluid, solid and mesh movement equations are solved simultaneously in fully-coupled fashion. The main advantage is that monolithic solvers tend to be more robust. Many of the problems encountered with the staggered approach are completely avoided with the monolithic approach. Of course, there is a price to pay in that the monolithic approach necessitates writing a fully-integrated fluid-structure solver, precluding the use of existing fluid and structure software. However, recent attempts have been made to design schemes that could in principle use existing fluid and structure software in the context of fully-coupled approaches [24].

Our aim in this work was to develop a robust isogeometric analysis formulation for fluid-structure interaction. Consequently, we opted for a monolithic approach, but we note various staggered techniques can also be obtained from the fully-coupled formulation at the linearization stage by removing certain blocks from the tangent matrix and employing a fixed, small number of Newton steps (see, e.g., [49]).

Isogeometric analysis was introduced in Hughes et al. [30] and further developed in [2–5, 13, 14, 16, 74]. Isogeometric analysis is based on the technologies used in engineering design, animation, graphic art, and visualization. It is a generalization of finite element analysis and it is a relatively simple matter to develop an isogeometric code from an existing finite element code. The main change involves writing a new shape function routine (see Hughes [28, Chap. 3]). It also requires an element routine that is written in a parameterized way, in particular, the number of degrees-of-freedom per

element needs to be a parameter. The element routines described in Hughes [28] possess this property. Some additional simple data structures are also required. We plan to describe these implementational aspects in detail in future work. In addition to including finite element analysis as a special case, isogeometric analysis offers the following possibilities: Precise and efficient geometry modeling; simplified mesh refinement and order elevation procedures; superior approximation properties; smooth basis functions with compact support; and, ultimately, the integration of geometric design and analysis.

In Sect. 2, we begin with a presentation of general continuum mechanics on domains undergoing arbitrary motion. The motion is described in terms of a space-time mapping of an arbitrary reference domain. The description is specialized for the cases of interest, namely, the Lagrangian description of a solid and the arbitrary Lagrangian–Eulerian (ALE) description of the fluid [32]. In the ALE description the domain is in motion but the motion does not coincide with the motion of material particles. The material particles are in relative motion with respect to the motion of the referential domain (*mobilis mobili*). In the derivations, it is found helpful to employ a space-time Piola transformation. Several useful forms of the conservation equations are presented, specifically, the advective, conservative and mixed forms.

The mixed form seems to be the preferred one for implementing the ALE description in the semi-discrete format. A key relation is identified that influences the ability of the formulation to conserve momentum in the discrete case. Specific forms of the fluid and solid equations used in the sequel are presented.

In Sect. 3 the variational formulation is described. The constituent formulations for the solid, fluid, mesh motion, and coupled problems are presented. In Sect. 4 the discrete spaces and continuity conditions at the fluid-structure interface are described. The semi-discrete problem is then introduced and a discussion of conservation properties follows. The conservation laws of interest are mass, momentum, and the so-called geometric conservation law. It is argued that all these are satisfied in the semi-discrete case, and the mass and geometric conservation laws also hold in the fully-discrete case. Momentum conservation in the fully discrete case depends on whether or not the time integrator preserves the key relation alluded to previously. If it does not, then the momentum is conserved up to the truncation errors introduced by the time integration algorithm in this key relation. The time integration is performed by the generalized- $\alpha$  method [12, 36]. We present, apparently for the first time, a subfamily of the generalized- $\alpha$  family of methods that is dissipative, second-order accurate, and unconditionally stable for the coupled fluid-structure case. In Sect. 5 the linearization of the system is presented including a discussion of the calculation of shape derivatives, that is, derivatives taken with

respect to the motion of the reference domain, namely, the mesh motion. The tangent that is derived contains all terms in the consistent tangent except ones involving derivatives of stabilization parameters appearing in the fluid subproblem. This is a common practice in the solution of stabilized formulations and does not seem to adversely affect convergence of the nonlinear problem in each time step.

Some specific aspects of isogeometric analysis are described in Sect. 6. Two benchmark calculations are presented in Sect. 7, flow over an elastic beam attached to a fixed square block and the inflation of a balloon. The inflation of a balloon is a particularly stringent test for a fluid-structure formulation. In Sect. 8 the application of NURBS-based isogeometric analysis to patient-specific arterial configurations is described. A simple finite-deformation constitutive law is studied for arterial applications and justified on the basis of an elementary equilibrium analysis of a simple arterial configuration. This model is then used in the fluid-structure interaction analysis of a patient-specific abdominal aortic aneurysm. Conclusions are drawn in Sect. 9. The derivation of some fundamental relations used in Sect. 2 by exterior calculus methodology is presented in Appendix A.

## 2 Conservation laws on moving domains

We begin by introducing the concept of a space-time mapping and the associated mathematical apparatus. In particular, a space-time Piola transformation (see, e.g., [46, 47] for background) emerges as a key concept. We then turn our attention to generic scalar and vector balance laws and make use of the space-time Piola transformation to derive their various forms.

### 2.1 Space-time mapping and Piola transform

Let  $\Omega_y \in \mathbb{R}^3$  be an open and bounded domain, referred to as the referential domain. Let  $r$  denote a time coordinate and let  $]0, T[$  be a time interval of interest. We define a *space-time* referential domain as  $Q_y = \Omega_y \times ]0, T[ \subset \mathbb{R}^4$ .

Let  $\hat{\phi}^{(4)} : Q_y \rightarrow Q_x \subset \mathbb{R}^4$  be a space-time mapping onto a *space-time* spatial domain, given by

$$Q_x = \left( (x, t) \mid \begin{Bmatrix} t \\ x \end{Bmatrix} = \hat{\phi}^{(4)}(y, r) = \begin{Bmatrix} r \\ \hat{\phi}(y, r) \end{Bmatrix} \forall (y, r) \in Q_y \right) \quad (1)$$

where  $\hat{\phi} : \Omega_y \rightarrow \Omega_x \subset \mathbb{R}^3$  denotes a mapping of the referential domain onto its spatial counterpart. (See Fig. 1 for an illustration.) Note that in (1),  $t = r$ , that is the spatial and referential clocks are synchronized.

**Remark 2.1** It is convenient to think of  $Q_y$ ,  $Q_x$ ,  $\Omega_y$ , and  $\Omega_x|_t = \hat{\phi}(\Omega_y, r = t)$  as differential manifolds. Despite the

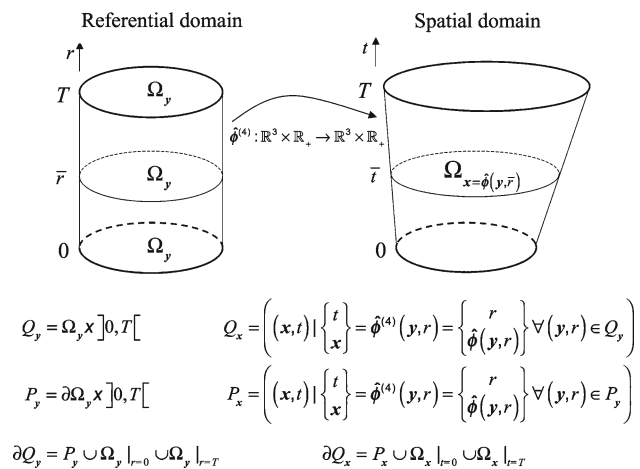


**Fig. 1** The space-time mapping of the referential domain onto the spatial domain. Note that, in all cases, the referential domain  $\Omega_y$  is fixed for all  $r \in ]0, T[$  in contrast with the spatial domain

fact that we take  $t = r$ , it is important to distinguish between the differential operators  $\partial/\partial r$  and  $\partial/\partial t$ , because in the former case we are assuming points  $y \in \Omega_y$  are being held fixed, whereas in the latter case we are assuming points  $x \in \Omega_x|_t$  are being held fixed.

**Remark 2.2** The spatial description is often referred to as the Eulerian description.

The deformation gradient associated with  $\hat{\phi}^{(4)}$  becomes

$$\hat{F}^{(4)} = D\hat{\phi}^{(4)} = \begin{bmatrix} \frac{\partial t}{\partial r} & \frac{\partial t}{\partial y} \\ \frac{\partial \hat{\phi}}{\partial r} & \frac{\partial \hat{\phi}}{\partial y} \end{bmatrix} = \begin{bmatrix} 1 & \mathbf{0}^T \\ \hat{v} & \hat{F} \end{bmatrix}, \quad (2)$$

where  $\mathbf{0} \in \mathbb{R}^3$  is the zero vector,  $\hat{F} \in \mathbb{R}^{3 \times 3}$  is the usual deformation gradient associated with  $\hat{\phi}$ , and  $\hat{v} \in \mathbb{R}^3$  is the referential velocity vector, defined as,

$$\hat{v} = \frac{\partial \hat{u}}{\partial r}, \quad (3)$$

where  $\hat{u}$  is the displacement of a point in the referential domain,

$$\hat{u}(y, r) = \hat{\phi}(y, r) - y, \quad (4)$$

and  $\frac{\partial}{\partial r}$  is the derivative with respect to the referential time variable taken with  $y$  held fixed.

The inverse of  $\hat{F}^{(4)}$  may be computed as

$$\hat{F}^{(4)-1} = \begin{bmatrix} 1 & \mathbf{0}^T \\ -\hat{F}^{-1}\hat{v} & \hat{F}^{-1} \end{bmatrix}, \quad (5)$$

and its transpose is

$$\hat{F}^{(4)-T} = \begin{bmatrix} 1 & -\hat{v}^T \hat{F}^{-T} \\ \mathbf{0} & \hat{F}^{-T} \end{bmatrix}. \quad (6)$$

The following relationship is also easily verified

$$\hat{J}^{(4)} \equiv \det \hat{\mathbf{F}}^{(4)} = \hat{J} \equiv \det \hat{\mathbf{F}}, \quad (7)$$

that is, the determinants of  $\hat{\mathbf{F}}^{(4)}$  and  $\hat{\mathbf{F}}$  are equal, a consequence of time synchronization.

Let  $\boldsymbol{\gamma}_x^{(4)} : Q_x \rightarrow \mathbb{R}^4$  denote a space-time flux vector field defined on the spatial configuration. In order to preserve the conservation structure in the reference configuration, we define  $\boldsymbol{\gamma}_y^{(4)}$ , a space-time flux vector field in the referential configuration, as

$$\boldsymbol{\gamma}_y^{(4)} = \hat{J}^{(4)} \hat{\mathbf{F}}^{(4)-1} \boldsymbol{\gamma}_x^{(4)}. \quad (8)$$

This is the *space-time Piola transformation*. With (8), we can prove the following space-time integral theorem:

$$\int_{Q_x} \nabla_x^{(4)} \cdot \boldsymbol{\gamma}_x^{(4)} dQ_x = \int_{Q_y} \nabla_y^{(4)} \cdot \boldsymbol{\gamma}_y^{(4)} dQ_y, \quad (9)$$

where

$$\nabla_x^{(4)} \equiv \left( \frac{\partial}{\partial t}, \frac{\partial}{\partial x} \right) \quad (10)$$

$$\nabla_y^{(4)} \equiv \left( \frac{\partial}{\partial t}, \frac{\partial}{\partial y} \right) \quad (11)$$

are the space-time gradient operators. The proof of (9) is based on the *Piola identity*, namely,

$$\nabla_y^{(4)} \cdot \left( \hat{J}^{(4)} \hat{\mathbf{F}}^{(4)-1} \right) = 0, \quad (12)$$

the transformation formula for volume elements,

$$dQ_x = \hat{J}^{(4)} dQ_y, \quad (13)$$

and straightforward calculations.

One must be careful in analysis on a space-time manifold because many commonly invoked results depend on the existence of a Riemannian metric, which in the present case does not exist. For example, there is no well-defined unit normal vector to the boundary of  $\partial Q_x$ , in contrast with  $\partial Q_y$ , for which there is a well-defined unit outward normal vector. However, many important results can be obtained without the existence of a Riemannian metric, or any metric for that matter. The subject of analysis on manifolds without metric structure (i.e., differential topology) is well-developed (see, Flanders [21], Spivak [57], Lang [44,45], Guillemin and Pollack [23], Bishop and Goldberg [8], Marsden and Hughes [47]). A proof of (9) using exterior calculus methodology is presented in Appendix A.

A way to understand (8) is to assume Cartesian coordinate charts on both  $Q_x$  and  $Q_y$ . We will denote these charts as  $\{x_a\}$  and  $\{y_A\}$ , respectively. We use lower case indices (i.e.,  $a, b, c, \dots$ ) to denote the current configuration and upper case indices (i.e.,  $A, B, C, \dots$ ) to denote the reference configuration. All the indices run over the range 0, 1, 2, 3 with 0

referring to the time coordinate, and 1, 2, 3 referring to the space coordinates. Summation over the range of the indices is implied for repeated indices. With these one can compute as follows:

$$\frac{\partial(\hat{J}^{(4)} \hat{\mathbf{F}}_{Aa}^{(4)-1})}{\partial y_A} = \frac{\partial \hat{J}^{(4)}}{\partial y_A} \hat{\mathbf{F}}_{Aa}^{(4)-1} + \hat{J}^{(4)} \frac{\partial \hat{\mathbf{F}}_{Aa}^{(4)-1}}{\partial y_A} \quad (14)$$

$$\begin{aligned} \frac{\partial \hat{J}^{(4)}}{\partial y_A} &= \frac{\partial \hat{J}^{(4)}}{\partial \hat{\mathbf{F}}_{bB}^{(4)}} \frac{\partial \hat{\mathbf{F}}_{bB}^{(4)}}{\partial y_A} \\ &= \text{cof} \hat{\mathbf{F}}_{bB}^{(4)} \frac{\partial^2 \hat{\phi}_b^{(4)}}{\partial y_A \partial y_B} \\ &= \hat{J}^{(4)} \hat{\mathbf{F}}_{bB}^{(4)-T} \frac{\partial^2 \hat{\phi}_b^{(4)}}{\partial y_A \partial y_B} \end{aligned} \quad (15)$$

$$\begin{aligned} \frac{\partial \hat{\mathbf{F}}_{Ca}^{(4)-1}}{\partial y_A} &= -\hat{\mathbf{F}}_{Cb}^{(4)-1} \frac{\partial \hat{\mathbf{F}}_{bB}^{(4)}}{\partial y_A} \hat{\mathbf{F}}_{Ba}^{(4)-1} \\ &= -\hat{\mathbf{F}}_{Cb}^{(4)-1} \frac{\partial^2 \hat{\phi}_b^{(4)}}{\partial y_A \partial y_B} \hat{\mathbf{F}}_{Ba}^{(4)-1} \end{aligned} \quad (16)$$

$$\frac{\partial \hat{\mathbf{F}}_{Aa}^{(4)-1}}{\partial y_A} = -\hat{\mathbf{F}}_{Ab}^{(4)-1} \frac{\partial^2 \hat{\phi}_b^{(4)}}{\partial y_A \partial y_B} \hat{\mathbf{F}}_{Ba}^{(4)-1} \quad (17)$$

$$\begin{aligned} \frac{\partial(\hat{J}^{(4)} \hat{\mathbf{F}}_{Aa}^{(4)-1})}{\partial y_A} &= \hat{J}^{(4)} \frac{\partial^2 \hat{\phi}_b^{(4)}}{\partial y_A \partial y_B} \hat{\mathbf{F}}_{Bb}^{(4)-1} \hat{\mathbf{F}}_{Aa}^{(4)-1} \\ &\quad - \hat{J}^{(4)} \frac{\partial^2 \hat{\phi}_b^{(4)}}{\partial y_A \partial y_B} \hat{\mathbf{F}}_{Ab}^{(4)-1} \hat{\mathbf{F}}_{Ba}^{(4)-1} \\ &= \hat{J}^{(4)} \frac{\partial^2 \hat{\phi}_b^{(4)}}{\partial y_A \partial y_B} \left( \hat{\mathbf{F}}_{Bb}^{(4)-1} \hat{\mathbf{F}}_{Aa}^{(4)-1} \right. \\ &\quad \left. - \hat{\mathbf{F}}_{Ab}^{(4)-1} \hat{\mathbf{F}}_{Ba}^{(4)-1} \right) \\ &= 0. \end{aligned} \quad (18)$$

This is the component form of (12). The last line of (18) follows from the fact that  $\frac{\partial^2 \hat{\phi}_b^{(4)}}{\partial y_A \partial y_B}$  is symmetric in  $A$  and  $B$ , and the term in parenthesis is skew-symmetric in  $A$  and  $B$ .

The referential domain can take on several interpretations. In fluid-structure interaction, it is usually taken to be the initial configuration of the problem domain. When the fluid domain moves, it becomes the so-called arbitrary Lagrangian–Eulerian (ALE) description. The material description is often utilized for the solid domain. By virtue of the fact that the referential domain is arbitrary, it can be specialized for the material description. This representation is also important for deriving material forms of the conservation laws. A summary of notations and important results for the material description follows. We set  $\mathbf{y} = \mathbf{X} \in \Omega_X \subset \mathbb{R}^3$ , a “particle” in the material domain, and  $r = s \in ]0, T[$ , the material time. As before, the differential operator  $\partial/\partial s$ , needs to be distinguished from  $\partial/\partial r$  and  $\partial/\partial t$ . In the case of  $\partial/\partial s$ , known as the material time derivative, the material point (i.e., particle)  $\mathbf{X} \in \Omega_X$  is held fixed. The material description is often referred to as the Lagrangian description.

The material and referential clocks are also synchronized. Let  $Q_X = \Omega_X \times ]0, T[ \subset \mathbb{R}^4$  and  $\phi^{(4)} : Q_X \rightarrow Q_x$ , where

$$Q_x = \left( (x, t) \mid \begin{Bmatrix} t \\ x \end{Bmatrix} = \phi^{(4)}(X, s) \right. \\ \left. = \begin{Bmatrix} s \\ \phi(X, s) \end{Bmatrix} \mid \forall (X, s) \in Q_s \right) \quad (19)$$

$$F^{(4)} = D\phi^{(4)} = \begin{bmatrix} \frac{\partial t}{\partial s} & \frac{\partial \mathbf{x}}{\partial s} \\ \frac{\partial \phi}{\partial s} & \frac{\partial \phi}{\partial X} \end{bmatrix} = \begin{bmatrix} 1 & \mathbf{0}^T \\ \mathbf{v} & \mathbf{F} \end{bmatrix}, \quad (20)$$

$$\mathbf{F} = \frac{\partial \phi}{\partial X} \quad (\text{deformation gradient}), \quad (21)$$

$$\mathbf{u}(X, s) = \phi(X, s) - X \quad (\text{particle displacement}), \quad (22)$$

$$\mathbf{v} = \frac{\partial \phi}{\partial s} = \frac{\partial \mathbf{u}}{\partial s} \quad (\text{particle velocity}), \quad (23)$$

$$F^{(4)-1} = \begin{bmatrix} 1 & \mathbf{0}^T \\ -F^{-1}\mathbf{v} & F^{-1} \end{bmatrix}, \quad (24)$$

$$F^{(4)-T} = \begin{bmatrix} 1 & -\mathbf{v}^T F^{-T} \\ \mathbf{0} & F^{-T} \end{bmatrix}. \quad (25)$$

$$J^{(4)} \equiv \det F^{(4)} = J \equiv \det F, \quad (26)$$

$$\gamma_X^{(4)T} = J \gamma_x^{(4)T} F^{(4)-T}. \quad (27)$$

$$\int_{Q_x} \nabla_x^{(4)} \cdot \gamma_x^{(4)} dQ_x = \int_{Q_X} \nabla_X^{(4)} \cdot \gamma_X^{(4)} dQ_X, \quad (28)$$

$$\nabla_X^{(4)} \equiv \left( \frac{\partial}{\partial s} \right) \quad (29)$$

## 2.2 Master balance laws

In this section we derive generic master balance laws for vectors and scalars, and present their various forms in the spatial and referential domains.

The following master balance laws hold on the spatial domain  $\Omega_x$  (see, e.g., [47] for background):

*Scalar case*

$$\frac{d}{dt} \int_{\Omega_x} \alpha d\Omega_x = \int_{\partial\Omega_x} \gamma_x^T \mathbf{n}_x d\partial\Omega_x + \int_{\Omega_x} \beta d\Omega_x, \quad (30)$$

*Vector case*

$$\frac{d}{dt} \int_{\Omega_x} \boldsymbol{\alpha} d\Omega_x = \int_{\partial\Omega_x} \boldsymbol{\Gamma}_x \mathbf{n}_x d\partial\Omega_x + \int_{\Omega_x} \boldsymbol{\beta} d\Omega_x. \quad (31)$$

In the above equations  $\alpha$ , a scalar, and  $\boldsymbol{\alpha}$ , a vector, are the conserved quantities of interest,  $\beta$ , a scalar, and  $\boldsymbol{\beta}$ , a vector, are the volumetric source terms, and  $\gamma_x^T \mathbf{n}$ , a scalar, and  $\boldsymbol{\Gamma}_x \mathbf{n}$ , a vector, are the surface fluxes.  $\mathbf{n}$  is the unit outward normal to  $\partial\Omega_x$ , the boundary of  $\Omega_x$ ,  $\gamma_x$  is a vector, and  $\boldsymbol{\Gamma}_x$  is a second-rank tensor. Note that the unit outward normal vector to the 3-dimensional spatial slices is well defined. Recall

that the domain  $\Omega_x$  changes with time and this must be taken into account in the time differentiation of the left-hand sides. Standard procedures (see [47]) yield the following:

$$\int_{\Omega_x} \frac{\partial \alpha}{\partial t} d\Omega_x = \int_{\partial\Omega_x} (\gamma_x - \alpha \mathbf{v})^T \mathbf{n}_x d\partial\Omega_x + \int_{\Omega_x} \beta d\Omega_x \quad (32)$$

and

$$\int_{\Omega_x} \frac{\partial \boldsymbol{\alpha}}{\partial t} d\Omega_x = \int_{\partial\Omega_x} (\boldsymbol{\Gamma}_x - \boldsymbol{\alpha} \otimes \mathbf{v}) \mathbf{n}_x d\partial\Omega_x + \int_{\Omega_x} \boldsymbol{\beta} d\Omega_x, \quad (33)$$

where the partial time derivative  $\partial/\partial t$  is taken with the spatial coordinate  $\mathbf{x}$  held fixed. Note that the boundary terms are modified by the fluxes involving the material particle velocity  $\mathbf{v}$ . Employing the divergence theorem on the boundary terms in (32) and (33) gives

$$\int_{\Omega_x} \frac{\partial \alpha}{\partial t} + \nabla_x \cdot (\alpha \mathbf{v} - \gamma_x) - \beta d\Omega_x = 0 \quad (34)$$

and

$$\int_{\Omega_x} \frac{\partial \boldsymbol{\alpha}}{\partial t} + \nabla_x \cdot (\boldsymbol{\alpha} \otimes \mathbf{v} - \boldsymbol{\Gamma}_x) - \boldsymbol{\beta} d\Omega_x = 0. \quad (35)$$

Equations (34) and (35) represent the scalar and vector master balance laws on the spatial domain written in a divergence form. We are going to employ Eq. (10) in (34) and (35) to obtain the same balance laws on the referential space-time domain, also in the divergence form. For this purpose we integrate (34) and (35) in time

$$\int_{Q_x} \frac{\partial \alpha}{\partial t} + \nabla_x \cdot (\alpha \mathbf{v} - \gamma_x) - \beta dQ_x = 0 \quad (36)$$

$$\int_{Q_x} \frac{\partial \boldsymbol{\alpha}}{\partial t} + \nabla_x \cdot (\boldsymbol{\alpha} \otimes \mathbf{v} - \boldsymbol{\Gamma}_x) - \boldsymbol{\beta} dQ_x = 0, \quad (37)$$

and then change variables, using (10)–(13),

$$\int_{Q_y} \frac{\partial \hat{\alpha}}{\partial r} + \nabla_y \cdot \left( \hat{\alpha} \hat{\mathbf{F}}^{-1} (\mathbf{v} - \hat{\mathbf{v}}) - \hat{\mathbf{F}}^{-1} \gamma_x \right) - \hat{\alpha} \hat{\beta} dQ_y = 0 \quad (38)$$

$$\int_{Q_y} \frac{\partial \hat{\boldsymbol{\alpha}}}{\partial r} + \nabla_y \cdot \left( \hat{\boldsymbol{\alpha}} \otimes (\mathbf{v} - \hat{\mathbf{v}}) \right) \hat{\mathbf{F}}^{-T} \\ - \hat{\boldsymbol{\Gamma}}_x \hat{\mathbf{F}}^{-T} - \hat{\boldsymbol{\beta}} dQ_y = 0. \quad (39)$$

The advantage of these forms of the master balance law is that one is free to choose any referential domain that is convenient for a given problem.

Particularly useful forms of (38) and (39) are obtained by choosing the reference domain to be the material domain. In



this case, we set  $\mathbf{y} = \mathbf{X}$ ,  $\hat{\mathbf{v}} = \mathbf{v}$ ,  $\hat{\mathbf{F}} = \mathbf{F}$ , and  $\hat{J} = J$ , in (38) and (39), and obtain, respectively,

$$\int_{Q_X} \frac{\partial J\alpha}{\partial s} - \nabla_X \cdot (J\mathbf{F}^{-1}\boldsymbol{\gamma}_x) - J\beta \, dQ_X = 0 \quad (40)$$

and

$$\int_{Q_X} \frac{\partial J\alpha}{\partial s} - \nabla_X \cdot (J\boldsymbol{\Gamma}_x \mathbf{F}^{-T}) - J\beta \, dQ_X = 0. \quad (41)$$

As may be noted, this results in a simplification of the general case due to the fact that  $\mathbf{v} - \hat{\mathbf{v}} = \mathbf{0}$ . This is an advantage of the Lagrangian description.

**Remark 2.3** In order to obtain local forms of the balance laws, we assume the integrands of any of the previous integral balance laws are continuous and the domain may be taken arbitrarily small about any space-time point. In this case, using standard arguments (see [47]), it follows that the integrands must vanish pointwise. This is referred to as the *localization argument*.

We can also state the mixed form of the master balance laws, where “mixed” refers to the fact that time and space derivatives are associated with different descriptions. This form is often used as a starting point of ALE formulations of balance laws. We first recognize that both  $\int_{Q_y} = \int_T \int_{\Omega_y}$  and  $\Omega_y$  do not change in time. Furthermore, using time synchronization and a localization argument *with respect to time* in (38) and (39) leads to

$$\int_{\Omega_y} \frac{\partial \hat{J}\alpha}{\partial r} + \nabla_y \cdot (\hat{J}\alpha \hat{\mathbf{F}}^{-1}(\mathbf{v} - \hat{\mathbf{v}}) - \hat{J}\hat{\mathbf{F}}^{-1}\boldsymbol{\gamma}_x) - \hat{J}\beta \, d\Omega_y = 0 \quad (42)$$

and

$$\int_{\Omega_y} \frac{\partial \hat{J}\alpha}{\partial r} + \nabla_y \cdot (\hat{J}(\alpha \otimes (\mathbf{v} - \hat{\mathbf{v}})) \hat{\mathbf{F}}^{-T} - \hat{J}\boldsymbol{\Gamma}_x \hat{\mathbf{F}}^{-T}) - \hat{J}\beta \, d\Omega_y = 0, \quad (43)$$

which hold at every time instant. Changing variables  $\int_{\Omega_y} \rightarrow \int_{\Omega_x}$  and using Eq. (10) and (13) yields

$$\int_{\Omega_x} \hat{J}^{-1} \frac{\partial \hat{J}\alpha}{\partial r} + \nabla_x \cdot (\alpha(\mathbf{v} - \hat{\mathbf{v}}) - \boldsymbol{\gamma}_x) - \beta \, d\Omega_x = 0 \quad (44)$$

and

$$\int_{\Omega_x} \hat{J}^{-1} \frac{\partial \hat{J}\alpha}{\partial r} + \nabla_x \cdot (\alpha \otimes (\mathbf{v} - \hat{\mathbf{v}}) - \boldsymbol{\Gamma}_x) - \beta \, d\Omega_x = 0. \quad (45)$$

Note that in (44) and (45), partial time derivatives are left with respect to the referential time variable, while the spatial

derivatives are taken with respect to spatial coordinates, leading to a mixed representation. These equations may be simplified further. Assuming sufficient smoothness of the fields, we compute

$$\begin{aligned} \hat{J}^{-1} \frac{\partial \hat{J}\alpha}{\partial r} &= \hat{J}^{-1} \left( \alpha \frac{\partial \hat{J}}{\partial r} + \hat{J} \frac{\partial \alpha}{\partial r} \right) \\ &= \hat{J}^{-1} \left( \alpha \hat{J} \nabla_x \cdot \hat{\mathbf{v}} + \hat{J} \frac{\partial \alpha}{\partial r} \right) \\ &= \boxed{\alpha \nabla_x \cdot \hat{\mathbf{v}}} + \frac{\partial \alpha}{\partial r}, \end{aligned} \quad (46)$$

where, going from the first to the second line, we have used the *key identity*

$$\frac{\partial \hat{J}}{\partial r} = \hat{J} \nabla_x \cdot \hat{\mathbf{v}}, \quad (47)$$

which we will discuss further in Sect. 4.3. Also note that

$$\nabla_x \cdot \alpha(\mathbf{v} - \hat{\mathbf{v}}) = (\mathbf{v} - \hat{\mathbf{v}}) \cdot \nabla_x \alpha + \alpha \nabla_x \cdot \mathbf{v} - \boxed{\alpha \nabla_x \cdot \hat{\mathbf{v}}}. \quad (48)$$

Similarly, for a vector quantity, we get

$$\hat{J}^{-1} \frac{\partial \hat{J}\alpha}{\partial r} = \boxed{\alpha \nabla_x \cdot \hat{\mathbf{v}}} + \frac{\partial \alpha}{\partial r}, \quad (49)$$

and

$$\nabla_x \cdot (\alpha \otimes (\mathbf{v} - \hat{\mathbf{v}})) = (\mathbf{v} - \hat{\mathbf{v}}) \cdot \nabla_x \alpha + \alpha \nabla_x \cdot \mathbf{v} - \boxed{\alpha \nabla_x \cdot \hat{\mathbf{v}}}. \quad (50)$$

Substituting (46) and (48) in (44), and (49) and (50) in (45) leads to simplified forms of the integral balance statements in the vector and scalar cases,

$$\int_{\Omega_x} \frac{\partial \alpha}{\partial r} + (\mathbf{v} - \hat{\mathbf{v}}) \cdot \nabla_x \alpha + \alpha \nabla_x \cdot \mathbf{v} - \nabla_x \cdot \boldsymbol{\gamma}_x - \beta \, d\Omega_x = 0 \quad (51)$$

and

$$\int_{\Omega_x} \frac{\partial \alpha}{\partial r} + (\mathbf{v} - \hat{\mathbf{v}}) \cdot \nabla_x \alpha + \alpha \nabla_x \cdot \mathbf{v} - \nabla_x \cdot \boldsymbol{\Gamma}_x - \beta \, d\Omega_x = 0 \quad (52)$$

respectively. It is important to note the disappearance in (51) and (52) of  $\alpha \nabla_x \cdot \hat{\mathbf{v}}$  and  $\alpha \nabla_x \cdot \hat{\mathbf{v}}$  [i.e., the boxed terms in (46), (48)–(50)]. This cancellation is due to (47). In the fully-discrete case, (47) may not be satisfied identically, which has implications to the discrete conservation of momentum. We will return to this point in Sect. 4.3.

## 2.3 Discussion of discretization choices for balance laws on moving domains

In the previous section we have derived integral balance laws on the referential and spatial domains. At the continuous or

infinite-dimensional level, all the instantiations of these laws are completely equivalent. The situation changes when one tries to numerically approximate the equations emanating from the balance laws. In this section we discuss the suitability of the existing computational approaches for partial differential equations arising from different forms of the balance laws. We focus on ALE and space-time methods (see, e.g., [31, 34, 41, 64, 65, 69]).

In the space-time finite element method the approximation space consists of basis functions that explicitly depend on space and time, denoted  $N_A(\mathbf{x}, t)$ , where  $A$  spans the index set  $\mathbf{I}$  of functions on a space-time mesh defined on  $Q_x$ . Letting  $u = u(\mathbf{x}, t)$  denote a generic space-time field, its partial time and spatial derivatives are expressed as follows:

$$u(\mathbf{x}, t) = \sum_{A \in \mathbf{I}} U_A N_A(\mathbf{x}, t) \quad (53)$$

$$\frac{\partial u}{\partial t}(\mathbf{x}, t) = \sum_{A \in \mathbf{I}} U_A \frac{\partial N_A}{\partial t}(\mathbf{x}, t) \quad (54)$$

and

$$\frac{\partial u}{\partial \mathbf{x}}(\mathbf{x}, t) = \sum_{A \in \mathbf{I}} U_A \frac{\partial N_A}{\partial \mathbf{x}}(\mathbf{x}, t) \quad (55)$$

where the  $U_A$ 's are real coefficients. Note that the partial time derivative in (54) is, by definition, taken with  $\mathbf{x}$  fixed. With this observation, the forms of the balance equations given by (36) and (37) are well-suited for space-time treatment.

One may also employ the space-time technique for discretizing the balance equations on the referential domain, (38) and (39). Just as before, let  $\hat{N}_A(\mathbf{y}, r)$  be the basis functions associated with the space-time discretization of  $Q_y$ . Now the solution field and its partial time and space derivatives become

$$\hat{u}(\mathbf{y}, r) = \sum_{A \in \mathbf{I}} \hat{U}_A \hat{N}_A(\mathbf{y}, r) \quad (56)$$

$$\frac{\partial \hat{u}}{\partial r}(\mathbf{y}, r) = \sum_{A \in \mathbf{I}} \hat{U}_A \frac{\partial \hat{N}_A}{\partial r}(\mathbf{y}, r) \quad (57)$$

and

$$\frac{\partial \hat{u}}{\partial \mathbf{y}}(\mathbf{y}, r) = \sum_{A \in \mathbf{I}} \hat{U}_A \frac{\partial \hat{N}_A}{\partial \mathbf{y}}(\mathbf{y}, r). \quad (58)$$

As before, the  $\hat{U}_A$ 's are real coefficients, but the partial time derivative in (57) is now taken with the referential coordinate  $\mathbf{y}$  held fixed.

The mixed form of the balance laws, as expressed by Eq. (44) and (45), is not amenable to space-time discretization because partial time and space derivatives employed in the formulation of the conservation equations are taken with respect to different descriptions, namely, the referential and spatial description, respectively. In this case, the

following approach is taken. On the referential domain  $\Omega_y$  one defines basis functions  $\hat{N}_A(\mathbf{y})$ ,  $A \in \mathbf{I}$ , and assumes the following expansion for the solution variable as a function of the referential domain variables

$$\hat{u}(\mathbf{y}, r) = \sum_{A \in \mathbf{I}} \hat{U}_A(r) \hat{N}_A(\mathbf{y}), \quad (59)$$

which, in turn, results in the following expression for the referential time derivative

$$\frac{\partial \hat{u}(\mathbf{y}, r)}{\partial r} = \sum_{A \in \mathbf{I}} \frac{\partial \hat{U}_A(r)}{\partial r} \hat{N}_A(\mathbf{y}). \quad (60)$$

The basis in the spatial configuration  $\Omega_x$  is the *push forward* of  $\hat{N}_A(\mathbf{y})$  defined by

$$N_A(\mathbf{x}, t) \equiv \hat{N}_A(\hat{\phi}^{-1}(\mathbf{x}, t)) = \hat{N}_A \circ \hat{\phi}^{-1}(\mathbf{x}, t) \quad (61)$$

In the spatial configuration, a solution field is now defined as

$$\begin{aligned} u(\mathbf{x}, t) &= \hat{u}(\hat{\phi}^{-1}(\mathbf{x}, t), t) = \sum_{A \in \mathbf{I}} \hat{U}_A(t) \hat{N}_A(\hat{\phi}^{-1}(\mathbf{x}, t)) \\ &= \sum_{A \in \mathbf{I}} \hat{U}_A(t) N_A(\mathbf{x}, t), \end{aligned} \quad (62)$$

and its gradient with respect to the spatial coordinates is easily computed as

$$\frac{\partial u(\mathbf{x}, t)}{\partial \mathbf{x}} = \sum_{A \in \mathbf{I}} \hat{U}_A(t) \frac{\partial N_A(\mathbf{x}, t)}{\partial \mathbf{x}} \quad (63)$$

Finally, on the spatial domain, the referential time derivative of the solution field becomes

$$\begin{aligned} \frac{\partial \hat{u}}{\partial r}(\hat{\phi}^{-1}(\mathbf{x}, t), t) &= \sum_{A \in \mathbf{I}} \frac{\partial \hat{U}_A(t)}{\partial r} \hat{N}_A \circ \hat{\phi}^{-1}(\mathbf{x}, t) \\ &= \sum_{A \in \mathbf{I}} \frac{\partial \hat{U}_A(t)}{\partial t} N_A(\mathbf{x}, t) \end{aligned} \quad (64)$$

In (44) and (45) the spatial gradient and the referential time derivative are evaluated according to (63) and (64), respectively. This is the essence of the discrete ALE approach. These particularly simple expressions explain in part the popularity of ALE methods for moving domain problems. Comparing expressions (62) and (64) we note that a referential time derivative of the solution in the spatial configuration may be obtained by simply taking a time derivative of its coefficients, thus rendering the semi-discrete equations amenable to finite-difference-in-time treatment. As a result, we may think of ALE as an extension of the classical semi-discrete approach to moving domain problems.

The semi-discrete approach may also be applied to the equations emanating from the master balance law written with respect to the referential domain [see Eqs. (42) and (43)]. An expression of the form (59) may be employed in this case

due to the orthogonality of space and time in the referential description.

## 2.4 Specific forms of solid and fluid equations

Although we fully recognize the elegance and power of the space-time approaches, in this work we opt for a numerical implementation in the semi-discrete setting. This, in turn, dictates the forms of the balance laws at the continuous level that we take as a point of departure for designing discrete formulations. In what follows, we use the developments of the previous sections to derive strong forms of the solid and fluid partial differential equations employed in this work.

### 2.4.1 Formulation of the solid problem

We adopt the material description for the solid and utilize Eqs. (40) and (41). Setting  $\alpha = \rho$ , the mass density of the solid, and  $\gamma = \mathbf{0}$  and  $\beta = 0$  in (40), we arrive at

$$\int_{Q_X} \frac{\partial J\rho}{\partial s} dQ_X = 0. \quad (65)$$

By the localization argument,

$$\frac{\partial J\rho}{\partial s} = 0, \quad (66)$$

implying that  $J\rho$  is a function of material particles alone, that is,  $J\rho(\mathbf{X}, s) = J\rho(\mathbf{X})$ . Assuming the initial configuration is the material configuration, that is  $\phi(\mathbf{X}, 0) = \mathbf{X}$ , then  $\mathbf{F}(\mathbf{X}, 0) = \mathbf{I}$  and  $J(\mathbf{X}, 0) = 1$ . Denoting by  $\rho_0$  the mass density of the solid in the initial configuration, we obtain the following point-wise statement of the *conservation of mass*

$$J\rho = \rho_0. \quad (67)$$

*Balance of linear momentum* follows from setting  $\alpha = \rho\mathbf{v}$ , the linear momentum density,  $\mathbf{\Gamma}_X = \boldsymbol{\sigma}$ , the “true” or Cauchy stress tensor, and  $\boldsymbol{\beta} = \rho\mathbf{f}$ , the force density per unit volume, in (41):

$$\int_{Q_X} \frac{\partial J\rho\mathbf{v}}{\partial s} - \nabla_X \cdot (J\boldsymbol{\sigma}\mathbf{F}^{-T}) - J\rho\mathbf{f} dQ_X = \mathbf{0}. \quad (68)$$

Localizing (68) to a point in space-time and substituting (67) we obtain a point-wise statement of balance of linear momentum

$$\rho_0 \frac{\partial \mathbf{v}}{\partial s} - \nabla_X \cdot (J\boldsymbol{\sigma}\mathbf{F}^{-T}) = \rho_0\mathbf{f}. \quad (69)$$

Note that if  $\mathbf{f} = \mathbf{0}$ , momentum is conserved.

To complete the specification of the solid problem we first introduce the displacement  $\mathbf{u}$ , such that  $\mathbf{v} = \partial\mathbf{u}/\partial s$ , and define  $\mathbf{P}$  and  $\mathbf{S}$ , the first and second Piola–Kirchhoff stress

tensors, respectively, as

$$\mathbf{P} = J\boldsymbol{\sigma}\mathbf{F}^{-T} \quad (70)$$

and

$$\mathbf{S} = \mathbf{F}^{-1}\mathbf{P} = J\mathbf{F}^{-1}\boldsymbol{\sigma}\mathbf{F}^{-T} \quad (71)$$

With these definitions, the solid problem takes a familiar form, namely

$$\rho_0 \frac{\partial^2 \mathbf{u}}{\partial s^2} - \nabla_X \cdot (\mathbf{F}\mathbf{S}) = \rho_0\mathbf{f} \quad (72)$$

Note that in this Lagrangian setting, provided the initial distribution of mass density  $\rho_0$  is given, the mass density is determined by the displacement, that is,  $\rho = \rho_0/J = \rho_0/\det \mathbf{F} = \rho_0/\det(\mathbf{I} + \nabla_X \mathbf{u})$ .

The details of the constitutive model used in this work are as follows. We use the generalized neo–Hookean model with penalty given in Simo and Hughes [55].  $\mathbf{S}$  derives from the gradient of an elastic potential  $\psi$  as

$$\mathbf{S} = 2 \frac{\partial \psi}{\partial \mathbf{C}} \quad (73)$$

where  $\mathbf{C}$  is the Cauchy–Green deformation tensor, defined as

$$\mathbf{C} = \mathbf{F}^T \mathbf{F} \quad (74)$$

The elastic potential is given by a sum decomposition

$$\psi = \psi_{\text{iso}} + \psi_{\text{dil}} \quad (75)$$

where  $\psi_{\text{iso}}$  is the energy associated with the volume-preserving or isochoric part of the motion, while  $\psi_{\text{dil}}$  is the energy of the volume-changing or dilatational part of the deformation. This decomposition expresses the fact that many materials respond differently in bulk and in shear. We perform the following multiplicative decomposition of the deformation gradient  $\mathbf{F}$  (see [16] and references therein):

$$\mathbf{F} = J^{1/3} \bar{\mathbf{F}} \quad (76)$$

where  $\bar{\mathbf{F}} = J^{-1/3} \mathbf{F}$ . Note that  $\det \bar{\mathbf{F}} = 1$ , hence  $\bar{\mathbf{F}}$  is associated with the volume-preserving part of the motion, while  $J^{1/3}$  is the volume-changing part. Let

$$\bar{\mathbf{C}} = \bar{\mathbf{F}}^T \bar{\mathbf{F}} \quad (77)$$

in direct analogy with (74). Then,

$$\psi_{\text{iso}} = \frac{1}{2} \mu^s (\text{tr} \bar{\mathbf{C}} - 3) \quad (78)$$

and

$$\psi_{\text{dil}} = \frac{1}{2} \kappa^s \left( \frac{1}{2} (J^2 - 1) - \ln J \right). \quad (79)$$

Note that this model fulfills all the normalization conditions necessary for well-posedness (see Marsden and Hughes [47], Holzapfel [27]). In particular, the  $\ln J$  term in the definition



of  $\psi_{dil}$  precludes material instabilities for states of strong compression. For this definition of the elastic potential, the second Piola-Kirchhoff stress tensor becomes

$$\mathbf{S} = \mu^s J^{-2/3} \left( \mathbf{I} - \frac{1}{3} \text{tr} \mathbf{C} \mathbf{C}^{-1} \right) + \frac{1}{2} \kappa^s (J^2 - 1) \mathbf{C}^{-1}, \quad (80)$$

and the fourth-order tensor of elastic moduli is

$$\begin{aligned} \mathbf{C} = 4 \frac{\partial^2 \psi}{\partial \mathbf{C} \partial \mathbf{C}} = & \left( \frac{2}{9} \mu^s J^{-2/3} \text{tr} \mathbf{C} + \kappa^s J^2 \right) \mathbf{C}^{-1} \otimes \mathbf{C}^{-1} \\ & + \left( \frac{2}{3} \mu^s J^{-2/3} \text{tr} \mathbf{C} - \kappa^s (J^2 - 1) \right) \mathbf{C}^{-1} \odot \mathbf{C}^{-1} \\ & - \frac{2}{3} \mu^s J^{-2/3} (\mathbf{I} \otimes \mathbf{C}^{-1} + \mathbf{C}^{-1} \otimes \mathbf{I}). \end{aligned} \quad (81)$$

In (81) the  $\otimes$  symbol is used to denote the outer product of two second-rank tensors, that is,

$$(\mathbf{C}^{-1} \otimes \mathbf{C}^{-1})_{IJKL} \equiv (\mathbf{C}^{-1})_{IJ} (\mathbf{C}^{-1})_{KL}, \quad (82)$$

and

$$(\mathbf{C}^{-1} \odot \mathbf{C}^{-1})_{IJKL} \equiv \frac{(\mathbf{C}^{-1})_{IK} (\mathbf{C}^{-1})_{JL} + (\mathbf{C}^{-1})_{IL} (\mathbf{C}^{-1})_{JK}}{2} \quad (83)$$

Parameters  $\mu^s$  and  $\kappa^s$  may be determined by the Lamé constants of the linear elastic model, denoted  $\mu^l$  and  $\lambda^l$ , by considering the case when the current and the reference configurations coincide. Then, by inspection,

$$\mu^s = \mu^l \quad (84)$$

$$\kappa^s = \lambda^l + \frac{2}{3} \mu^l. \quad (85)$$

Thus,  $\mu^s$  and  $\kappa^s$  are the classical shear and bulk moduli, respectively.

## 2.4.2 Formulation of the fluid problem

While the solid problem is written using a Lagrangian description, an ALE approach is adopted for the fluid problem. Although ALE is widely used for fluid flow in moving domains, the authors wish to point out the recent works on the Particle Finite Element Method (PFEM, see, e.g., [35] and references therein), which makes use of a Lagrangian description of fluid mechanics, enabling straight-forward solution of very complicated flows and fluid-structure interaction problems. To arrive at the formulation of the fluid problem employed in this work, Eq. (51) and (52) are taken as a departure point. Note that we work with the so-called advective forms of the master balance laws rather than their conservative counterparts given by (44) and (45). We will show later in this paper that our final semi-discrete formulation satisfies global conservation of mass and linear momentum. Furthermore, the advantage of the advective form is that, when

discretized, it trivially satisfies the so-called Discrete Geometric Conservation Law (DGCL). The DGCL states that in the absence of body forces and surface tractions, the discrete scheme must preserve a constant velocity solution. For a discussion of the importance of conservation and satisfaction of the DGCL for moving domain problems see [17, 22, 46].

Substituting  $\alpha = \rho$ ,  $\boldsymbol{\gamma} = \mathbf{0}$  and  $\beta = 0$  in (50), we arrive at

$$\int_{\Omega_x} \frac{\partial \rho}{\partial r} + (\mathbf{v} - \hat{\mathbf{v}}) \cdot \nabla_x \rho + \rho \nabla_x \cdot \mathbf{v} \, d\Omega_x = 0. \quad (86)$$

Assuming that the fluid has constant mass density (i.e., the flow is incompressible) and localizing the above equation to a point in space and time, we obtain the following form of the mass conservation equation,

$$\nabla_x \cdot \mathbf{v} = 0, \quad (87)$$

which manifests the incompressibility constraint. To arrive at the conservation of linear momentum we use (52) and set  $\alpha = \rho \mathbf{v}$ ,  $\boldsymbol{\Gamma} = \boldsymbol{\sigma}$ , and  $\beta = \rho \mathbf{f}$

$$\begin{aligned} \int_{\Omega_x} \frac{\partial \rho \mathbf{v}}{\partial r} + (\mathbf{v} - \hat{\mathbf{v}}) \cdot \nabla_x \rho \mathbf{v} \\ + \rho \mathbf{v} \nabla_x \cdot \mathbf{v} - \nabla_x \cdot \boldsymbol{\sigma} - \rho \mathbf{f} \, d\Omega_x = 0. \end{aligned} \quad (88)$$

Using the assumption of constant mass density, (87) and localizing the result to a point in space and time, we obtain

$$\rho \frac{\partial \mathbf{v}}{\partial r} + \rho (\mathbf{v} - \hat{\mathbf{v}}) \cdot \nabla_x \mathbf{v} - \nabla_x \cdot \boldsymbol{\sigma} = \rho \mathbf{f}. \quad (89)$$

To complete the specification of the fluid problem, we assume that the flow is Newtonian with the following definition of the Cauchy stress tensor

$$\boldsymbol{\sigma} = -p \mathbf{I} + 2\mu \nabla_x^s \mathbf{v}, \quad (90)$$

where  $p$  is the pressure,  $\mu$  is the dynamic viscosity,  $\mathbf{I}$  is the second-rank identity tensor, and  $\nabla_x^s = 1/2(\nabla_x + \nabla_x^T)$  is the symmetric gradient.

**Remark 2.4** We note that if  $\mathbf{f} = \mathbf{0}$  and  $\boldsymbol{\sigma} \cdot \mathbf{n} = \mathbf{0}$  on  $\partial\Omega_x$ , then  $\mathbf{v} = \text{constant}$  identically satisfies (88).

## 3 Variational formulation of the coupled fluid-structure interaction problem at the continuous level

Let  $\Omega_0 \equiv \Omega_y \subset \mathbb{R}^d$ ,  $d = 2, 3$ , represent the combined fluid and solid domain in the initial configuration, which serves simultaneously as the reference configuration. Let  $\hat{\boldsymbol{\phi}} : \Omega_0 \rightarrow \Omega_t \equiv \Omega_x|_t \subset \mathbb{R}^d$  denote the motion of the fluid-solid domain, as before.

The domain  $\Omega_0$  admits the decomposition

$$\Omega_0 = \overline{\Omega_0^f} \cup \Omega_0^s, \quad (91)$$

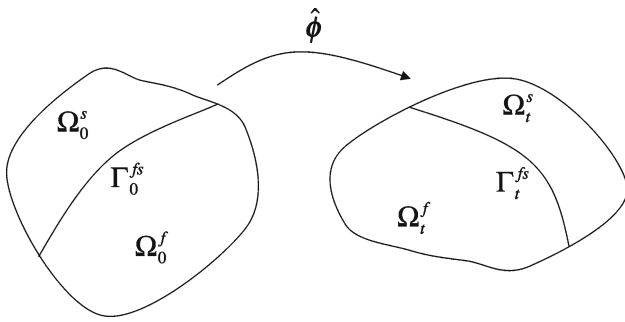


**Fig. 2** Abstract setting for the fluid-structure interaction problem. Depiction of the initial and the current configurations related through the ALE mapping. The initial configuration also serves as the reference configuration

where  $\Omega_0^f$  is the subset of  $\Omega_0$  occupied by the fluid, and  $\Omega_0^s$  is the subset of  $\Omega_0$  occupied by the solid. The decomposition is non-overlapping, that is

$$\Omega_0^f \cap \Omega_0^s = \emptyset. \quad (92)$$

Likewise,

$$\Omega_t = \overline{\Omega_t^f \cup \Omega_t^s}, \quad (93)$$

with

$$\Omega_t^f \cap \Omega_t^s = \emptyset. \quad (94)$$

Let  $\Gamma_0^{fs}$  denote the interface between the fluid and the solid regions in the initial configuration, and, analogously, let  $\Gamma_t^{fs}$  be its counterpart in the current configuration. The setup is illustrated in Fig. 2. It is important to emphasize that the motion of the fluid domain is not the particle motion of the fluid. It does, however, conform to the particle motion of the solid at the fluid-solid interface because the Lagrangian description is adopted for the solid.

### 3.1 Solid problem

This section gives a weak formulation of the solid in the Lagrangian description. Let  $\mathcal{V}^s = \mathcal{V}^s(\Omega_0^s)$  denote the trial solution space for displacements and let  $\mathcal{W}^s = \mathcal{W}^s(\Omega_0^s)$  denote the trial weighting space for the linear momentum equations. Let  $\mathbf{u}$  denote the displacement of the solid with respect to the initial configuration and let  $\mathbf{w}^s$  be the weighting function for the momentum equation. We also assume that the displacement satisfies the boundary condition,  $\mathbf{u} = \mathbf{g}^s$  on  $\Gamma_0^{s,D}$ , the Dirichlet part of the solid domain boundary. The variational formulation is stated as follows: Find  $\mathbf{u} \in \mathcal{V}^s$  such that  $\forall \mathbf{w}^s \in \mathcal{W}^s$ ,

$$B^s(\mathbf{w}^s, \mathbf{u}) = F^s(\mathbf{w}^s) \quad (95)$$

where

$$B^s(\mathbf{w}^s, \mathbf{u}) = \left( \mathbf{w}^s, \rho_0^s \frac{\partial^2 \mathbf{u}}{\partial s^2} \right)_{\Omega_0^s} + (\nabla_X \mathbf{w}^s, \mathbf{F}S)_{\Omega_0^s}, \quad (96)$$

and

$$F^s(\mathbf{w}^s) = (\mathbf{w}^s, \rho_0^s \mathbf{f}^s)_{\Omega_0^s} + (\mathbf{w}^s, \mathbf{h}^s)_{\Gamma_0^{s,N}}, \quad (97)$$

where  $\Gamma_0^{s,N}$  is the Neumann part of the solid boundary,  $\mathbf{h}^s$  is the boundary traction vector,  $\rho_0^s$  is the density of the solid in the initial configuration,  $\mathbf{f}^s$  is the body force per unit mass, and  $(\cdot, \cdot)_{\mathcal{D}}$  is the  $L^2$  inner product with respect to domain  $\mathcal{D}$ . The above relations are written over the initial configuration  $\Omega_0^s$ , which is also the material configuration. The subscript  $X$  on the partial derivative operators indicates that the derivatives are taken with respect to the material coordinates  $X$ .

### 3.2 Motion of the fluid subdomain

This section gives a weak formulation of the motion of the fluid subdomain. Partial differential equations of linear elastostatics subject to Dirichlet boundary conditions coming from the displacements of the solid region are employed to define the ALE mapping  $\hat{\phi}(\mathbf{y}, r)$  of the fluid domain. For precise conditions on the regularity of the ALE map, see Nobile [51]. In the discrete setting, the fluid subdomain motion problem is referred to as “mesh moving.” The fluid subdomain motion problem may be thought of as a succession of fictitious linear elastic boundary-value problems designed simply to produce a smooth evolution of the fluid mesh.

We write  $\hat{\phi}_r(\mathbf{y}) = \hat{\phi}(\mathbf{y}, r)$ . Consequently,  $\hat{\phi}_r : \Omega_0 \rightarrow \Omega_r$  and  $\hat{\phi}_r^{-1} : \Omega_r \rightarrow \Omega_0$ . Likewise, we define the displacement of the reference domain as

$$\hat{\mathbf{u}}(\mathbf{y}, r) = \hat{\phi}(\mathbf{y}, r) - \mathbf{y} \quad (98)$$

and write  $\hat{\mathbf{u}}_r(\mathbf{y}) = \hat{\mathbf{u}}(\mathbf{y}, r)$ . Note that  $\hat{\mathbf{u}}_r$  is defined on  $\Omega_0$  and represents the displacement of the reference configuration at time  $r$ .

Let  $\Omega_{\tilde{t}}$  be the configuration of  $\Omega_0$  at  $\tilde{t} < t$ . We think of this as a configuration “nearby”  $\Omega_t$  that in numerical computations will typically represent the final configuration of the previous time step. We wish to push forward the functions defined on  $\Omega_0$  to  $\Omega_{\tilde{t}}$ . We write  $\hat{\phi}_{\tilde{t}} : \Omega_0 \rightarrow \Omega_{\tilde{t}}$  and  $\hat{\phi}_{\tilde{t}}^{-1} : \Omega_{\tilde{t}} \rightarrow \Omega_0$ . Then  $\hat{\mathbf{u}}_t \circ \hat{\phi}_{\tilde{t}}^{-1}$  and  $\hat{\mathbf{u}}_{\tilde{t}} \circ \hat{\phi}_{\tilde{t}}^{-1}$  are the displacements of the reference domain at time  $t$  and  $\tilde{t}$ , respectively, but both are defined with respect to the configuration of the reference domain at time  $\tilde{t}$ , namely  $\Omega_{\tilde{t}}$ . We write  $\tilde{\mathbf{x}} = \hat{\phi}_{\tilde{t}}(\mathbf{y}) \in \Omega_{\tilde{t}}$ . To determine  $\hat{\phi}_{\tilde{t}}$  we will construct a linear elastic boundary problem for  $\hat{\mathbf{u}}_t \circ \hat{\phi}_{\tilde{t}}^{-1}$  and utilize

$$\hat{\phi}_{\tilde{t}}(\mathbf{y}) = \hat{\phi}_{\tilde{t}}(\mathbf{y}) + \left( \hat{\mathbf{u}}_t \circ \hat{\phi}_{\tilde{t}}^{-1} \right) \left( \hat{\phi}_{\tilde{t}}(\mathbf{y}) \right) \quad (99)$$

We would like to remind the reader that  $\hat{\phi}_{\tilde{t}}$  and  $\hat{u}_{\tilde{t}}$  are considered known when we solve for  $\hat{u}_t \circ \hat{\phi}_{\tilde{t}}^{-1}$ .

Let  $\mathcal{V}^m = \mathcal{V}^m(\Omega_{\tilde{t}}^f)$  denote the trial solution space of displacements and let  $\mathcal{W}^m = \mathcal{W}^m(\Omega_{\tilde{t}}^f)$  denote the weighting space for the elastic equilibrium equations. As usual, kinematic boundary conditions are built into the definitions of the spaces, namely,

$$\mathcal{V}^m = \left\{ \mathbf{u}^m \mid \mathbf{u}^m \in \left( H^1(\Omega_{\tilde{t}}^f) \right)^d, \mathbf{u}^m = \mathbf{u}_t \circ \hat{\phi}_{\tilde{t}}^{-1} \text{ on } \Gamma_{\tilde{t}}^{fs} \right\} \quad (100)$$

$$\mathcal{W}^m = \left\{ \mathbf{w}^m \mid \mathbf{w}^m \in \left( H^1(\Omega_{\tilde{t}}^f) \right)^d, \mathbf{w}^m = \mathbf{0} \text{ on } \Gamma_{\tilde{t}}^{fs} \right\} \quad (101)$$

where  $\mathbf{u}_t$  is the particle displacement at time  $t$ . Note that in our formulation  $\mathbf{u}_t$  will be an unknown and will be solved for simultaneously along with  $\hat{u}_t$  in a coupled fashion. The variational formulation of the problem is stated as follows: Find  $\hat{u}_t \circ \hat{\phi}_{\tilde{t}}^{-1} \in \mathcal{V}^m$  such that  $\forall \mathbf{w}^m \in \mathcal{W}^m$ ,

$$B^m(\mathbf{w}^m, \hat{u}_t \circ \hat{\phi}_{\tilde{t}}^{-1}) = F^m(\mathbf{w}^m), \quad (102)$$

where

$$B^m(\mathbf{w}^m, \mathbf{u}^m) = (\nabla_{\tilde{x}}^s \mathbf{w}^m, 2\mu^m \nabla_{\tilde{x}}^s \mathbf{u}^m)_{\Omega_{\tilde{t}}^f} + (\nabla_{\tilde{x}} \cdot \mathbf{w}^m, \lambda^m \nabla_{\tilde{x}} \cdot \mathbf{u}^m)_{\Omega_{\tilde{t}}^f}, \quad (103)$$

$$F^m(\mathbf{w}^m) = B^m(\mathbf{w}^m, \hat{u}_{\tilde{t}} \circ \hat{\phi}_{\tilde{t}}^{-1}), \quad (104)$$

and  $\nabla_{\tilde{x}}$  is the gradient operator on  $\Omega_{\tilde{t}}^f$ ,  $\nabla_{\tilde{x}}^s$  is its symmetrization, and  $\mu^m$  and  $\lambda^m$  are the Lamé parameters of the fictitious linear elastic model characterizing the motion of the fluid domain. In the discrete setting  $\mu^m$  and  $\lambda^m$  should be selected (as it was demonstrated in [37]) such that the fluid mesh quality is preserved for as long as possible. In particular, mesh quality can be preserved by dividing the elastic coefficients by the Jacobian determinant of the element mapping, effectively increasing the stiffness of the smaller elements [37,48,70], which are typically placed at fluid-solid interfaces. For advanced mesh moving techniques see [38,39,58,59]. Parts of the boundary of the fluid region may also have motion prescribed independent of the motion of the solid region. This is handled in a standard way as a Dirichlet boundary condition. The remainder of the fluid region boundary is typically subjected to a “zero stress” Neumann boundary condition.

As a result of the above construction, the ALE mapping for the entire domain may be defined in a piece-wise fashion. Recall that this means for the solid domain that we take  $\mathbf{y} = \mathbf{X}$ ,  $r = s$ ,  $\hat{\phi} = \phi$ , and  $\hat{u} = \mathbf{u}$ . We write

$$\hat{\phi}(\mathbf{y}, r) = \begin{cases} \mathbf{X} + \mathbf{u}(\mathbf{X}, s) & \forall \mathbf{X} \in \Omega_0^s, s \in (0, T) \\ \mathbf{y} + \hat{\mathbf{u}}(\mathbf{y}, r) & \forall \mathbf{y} \in \Omega_0^f, r \in (0, T) \end{cases} \quad (105)$$

Note that due to (100), the ALE map  $\hat{\phi}$  in (105) is continuous at the fluid-solid interface. Recall also that the velocity of the fluid domain is obtained by taking a partial time derivative of  $\hat{\mathbf{u}}$  with  $\mathbf{y}$  held fixed, that is,  $\hat{\mathbf{v}} = \partial \hat{\mathbf{u}} / \partial r$ .

### 3.3 Fluid problem

In this section we give a weak formulation of the incompressible Navier–Stokes fluid on a moving domain in the ALE description. The motion of the fluid domain was constructed in the previous section. Let  $\mathcal{V}^f = \mathcal{V}^f(\Omega_{\tilde{t}}^f)$  denote the trial solution space of velocities and pressures and let  $\mathcal{W}^f = \mathcal{W}^f(\Omega_{\tilde{t}}^f)$  denote the trial weighting space for the momentum and continuity equations. Let  $\{\mathbf{v}, p\}$  denote the particle velocity-pressure pair and  $\{\mathbf{w}^f, q^f\}$  the weighting functions for the momentum and continuity equations. We also assume that the fluid particle velocity field satisfies the boundary condition,  $\mathbf{v} = \mathbf{g}^f$  on  $\Gamma_{\tilde{t}}^{f,D}$ , the Dirichlet part of the fluid boundary. The variational formulation is stated as follows: Find  $\{\mathbf{v}, p\} \in \mathcal{V}^f$  such that  $\forall \{\mathbf{w}^f, q^f\} \in \mathcal{W}^f$ ,

$$B^f(\{\mathbf{w}^f, q^f\}, \{\mathbf{v}, p\}; \hat{\mathbf{v}}) = F^f(\{\mathbf{w}^f, q^f\}) \quad (106)$$

where

$$\begin{aligned} B^f(\{\mathbf{w}^f, q^f\}, \{\mathbf{v}, p\}; \hat{\mathbf{v}}) &= \left( \mathbf{w}^f, \rho^f \frac{\partial \mathbf{v}}{\partial r} \right)_{\Omega_{\tilde{t}}^f} + \left( \mathbf{w}^f, \rho^f (\mathbf{v} - \hat{\mathbf{v}}) \cdot \nabla_{\tilde{x}} \mathbf{v} \right)_{\Omega_{\tilde{t}}^f} \\ &\quad + (q^f, \nabla_{\tilde{x}} \cdot \mathbf{v})_{\Omega_{\tilde{t}}^f} - (\nabla_{\tilde{x}} \cdot \mathbf{w}^f, p)_{\Omega_{\tilde{t}}^f} \\ &\quad + \left( \nabla_{\tilde{x}}^s \mathbf{w}^f, 2\mu^f \nabla_{\tilde{x}}^s \mathbf{v} \right)_{\Omega_{\tilde{t}}^f}, \end{aligned} \quad (107)$$

and

$$F^f(\{\mathbf{w}^f, q^f\}) = (\mathbf{w}^f, \rho^f \mathbf{f}^f)_{\Omega_{\tilde{t}}^f} + (\mathbf{w}^f, \mathbf{h}^f)_{\Gamma_{\tilde{t}}^{f,N}}, \quad (108)$$

where  $\Gamma_{\tilde{t}}^{f,N}$  is the Neumann part of the fluid domain boundary,  $\mathbf{h}^f$  is the boundary traction vector,  $\mathbf{f}^f$  is the body force per unit mass, and  $\rho^f$  and  $\mu^f$  are the density and the dynamic viscosity of the fluid, respectively. The above equations are written with respect to the current configuration  $\Omega_{\tilde{t}}$ ,  $\nabla_{\tilde{x}}$  is the gradient operator on  $\Omega_{\tilde{t}}$ , and  $\nabla_{\tilde{x}}^s$  is its symmetrization.

### 3.4 Coupled problem

In this section we present the coupled fluid-structure interaction problem, which is based on the individual subproblems introduced previously. The variational formulation for the coupled problem is stated as: Find  $\{\mathbf{v}, p\} \in \mathcal{V}^f$ ,  $\mathbf{u} \in \mathcal{V}^s$ , and  $\hat{\mathbf{u}} \in \mathcal{V}^m$  such that  $\forall \{\mathbf{w}^f, q^f\} \in \mathcal{W}^f$ ,  $\forall \mathbf{w}^s \in \mathcal{W}^s$ , and  $\forall \mathbf{w}^m \in \mathcal{W}^m$ ,

$$\begin{aligned} B^f(\{\mathbf{w}^f, q^f\}, \{\mathbf{v}, p\}; \hat{\mathbf{v}}) - F^f(\{\mathbf{w}^f, q^f\}) + B^s(\mathbf{w}^s, \mathbf{u}) \\ - F^s(\mathbf{w}^s) + B^m(\mathbf{w}^m, \hat{\mathbf{u}}) - F^m(\mathbf{w}^m) = 0. \end{aligned} \quad (109)$$

with the following auxiliary relations holding in the sense of traces:

$$\mathbf{v} \Big|_{\Gamma_t^{fs}} = \frac{\partial \mathbf{u}}{\partial t} \circ \hat{\boldsymbol{\phi}}^{-1} \Big|_{\Gamma_t^{fs}}, \quad (110)$$

$$\mathbf{w}^f \Big|_{\Gamma_t^{fs}} = \mathbf{w}^s \circ \hat{\boldsymbol{\phi}}^{-1} \Big|_{\Gamma_t^{fs}}. \quad (111)$$

Relationship (110), the kinematic constraint, equates the fluid particle velocity with that of the solid at the fluid-solid boundary. Equation (111) leads to the compatibility of the Cauchy stress vector at the fluid-solid interface. To demonstrate this fact, we first set  $\mathbf{w}^m = \mathbf{0}$  and focus on the fluid and solid parts of the coupled problem (109). Integrating by parts in (109) and assuming sufficient regularity of the solution fields gives

$$\begin{aligned} 0 = & \left( \mathbf{w}^f, \mathcal{L}^f(\mathbf{v}, p; \hat{\mathbf{v}}) - \rho^f \mathbf{f}^f \right)_{\Omega_t^f} + \left( q^f, \nabla_x \cdot \mathbf{v} \right)_{\Omega_t^f} \\ & + \left( \mathbf{w}^f, \boldsymbol{\sigma}^f \mathbf{n}_t^f - \mathbf{h}^f \right)_{\Gamma_t^{f,N}} + \left( \mathbf{w}^f, \boldsymbol{\sigma}^f \mathbf{n}_t^f \right)_{\Gamma_t^{fs}} \\ & + \left( \mathbf{w}^s, \mathcal{L}^s(\mathbf{u}) - \rho_0^s \mathbf{f}^s \right)_{\Omega_0^s} + \left( \mathbf{w}^s, \mathbf{P} \mathbf{n}_0^s - \mathbf{h}^s \right)_{\Gamma_0^{s,N}} \\ & + \left( \mathbf{w}^s, \mathbf{P} \mathbf{n}_0^s \right)_{\Gamma_0^{fs}}, \end{aligned} \quad (112)$$

where  $\mathbf{n}_t^f$  and  $\mathbf{n}_0^s$  are the unit outward normal vectors to the fluid and solid domains, in the current and reference configurations, respectively. In (112) the following definitions are used:

$$\mathcal{L}^f(\mathbf{v}, p; \hat{\mathbf{v}}) = \rho^f \frac{\partial \mathbf{v}}{\partial r} + \rho^f (\mathbf{v} - \hat{\mathbf{v}}) \cdot \nabla_x \mathbf{v} - \nabla_x \cdot \boldsymbol{\sigma}^f, \quad (113)$$

$$\boldsymbol{\sigma}^f = -\nabla_x p \mathbf{I} + 2\mu^f \nabla_x^s \mathbf{v}, \quad (114)$$

$$\mathcal{L}^s(\mathbf{u}) = \rho_0^s \frac{\partial^2 \mathbf{u}}{\partial s^2} - \nabla_x \cdot \mathbf{P}. \quad (115)$$

$$\mathbf{P} = \mathbf{F} \mathbf{S}, \quad (116)$$

Standard variational arguments imply that the fluid and the solid momentum equations and the fluid incompressibility constraint hold in the interior of the appropriate subdomains. The Neumann boundary conditions are also satisfied on the appropriate parts of the fluid and solid domain boundaries. Selecting test functions that vanish everywhere in the domain, except at the fluid-solid interface in (112), gives

$$\left( \mathbf{w}^f, \boldsymbol{\sigma}^f \mathbf{n}_t^f \right)_{\Gamma_t^{fs}} + \left( \mathbf{w}^s, \mathbf{P} \mathbf{n}_0^s \right)_{\Gamma_0^{fs}} = 0. \quad (117)$$

Transforming the second term in (117) to the current configuration, yields

$$\left( \mathbf{w}^f, \boldsymbol{\sigma}^f \mathbf{n}_t^f \right)_{\Gamma_t^{fs}} + \left( \mathbf{w}^s \circ \hat{\boldsymbol{\phi}}^{-1}, \boldsymbol{\sigma}^s \mathbf{n}_t^s \right)_{\Gamma_t^{fs}} = 0. \quad (118)$$

Using (111) we arrive at the weak continuity of surface tractions at the fluid-solid interface

$$\left( \mathbf{w}^f, \boldsymbol{\sigma}^f \mathbf{n}_t^f + \boldsymbol{\sigma}^s \mathbf{n}_t^s \right)_{\Gamma_t^{fs}} = 0, \quad (119)$$

which, together with (110), produces proper fluid-solid interface conditions.

#### 4 Formulation of the fluid-structure interaction problem at the discrete level

In this section we give a formulation of the fluid-structure interaction Eq. (109) in the discrete setting. We begin by defining the spatial discretization of the problem. It is exactly the same for finite elements and NURBS-based isogeometric analysis. Having defined the semi-discrete forms, we present the time stepping algorithm, which is the generalized- $\alpha$  method of Chung and Hulbert [12].

##### 4.1 Approximation spaces and enforcement of kinematic compatibility conditions

We begin by considering the discretization of the reference domain  $\Omega_0$ . Here, and in what follows, we will use the same notation for the discrete objects as for their continuous counterparts to simplify the presentation. Let  $\hat{N}_A$  denote a set of basis functions defined on  $\Omega_0$ , as in Sect. 2.3, and let  $I$  denote the index set of all basis functions defined on  $\Omega_0$ . These functions do not depend on time, they are “fixed” in space on the reference domain. Consider a *discrete* ALE mapping  $\hat{\boldsymbol{\phi}}(\mathbf{y}, r)$  which can be expressed as

$$\hat{\boldsymbol{\phi}}(\mathbf{y}, r) = \sum_{A \in I} \hat{\boldsymbol{\phi}}_A(r) \hat{N}_A(\mathbf{y}) = \sum_{A \in I} (\hat{\mathbf{U}}_A(r) + \mathbf{y}_A) \hat{N}_A(\mathbf{y}) \quad (120)$$

The mapping pertains to the entire fluid-structure domain. The motion of the fluid subdomain is obtained from (120) by restricting the index set to the fluid control variables (or nodal variables in the case of finite elements). We write  $I = I_f \cup I_s$ , where  $I_f$  and  $I_s$  are the index sets of the fluid and solid control variables, respectively. Note that  $I_f \cap I_s \neq \emptyset$  due to the kinematic continuity conditions imposed at the fluid-solid interface.

The displacement field of the solid is written as

$$\mathbf{u}(\mathbf{X}, s) = \sum_{A \in I_s} \mathbf{U}_A(s) \hat{N}_A(\mathbf{X}), \quad (121)$$

We assume that all basis functions in the reference configuration are at least  $C^0$ -continuous, which automatically makes them  $H^1$ -conforming. In this work, we also require that the discretization at the fluid-solid interface is conforming, that is,  $\hat{N}_A$ 's are  $C^0$ -continuous across  $\Gamma_0^{fs}$ .

In contrast to the solid problem, the fluid problem (106) is posed over the current configuration with unknown fields expressed as functions of the spatial coordinates  $\mathbf{x}$ . In order to approximate the unknown fields in the current domain, we employ  $\{N_A(\mathbf{x}, t) = \hat{N}_A \circ \hat{\boldsymbol{\phi}}_t^{-1}(\mathbf{x})\}_{A \in I_f}$ , as defined in Sect. 2.3, Eq. (61), to approximate the fluid velocity and

pressure as

$$\mathbf{v}(\mathbf{x}, t) = \sum_{A \in I_f} \mathbf{V}_A(t) N_A(\mathbf{x}, t), \quad (122)$$

$$p(\mathbf{x}, t) = \sum_{A \in I_f} P_A(t) N_A(\mathbf{x}, t) \quad (123)$$

The fluid domain motion problem (106) is posed over a configuration at time  $\tilde{t}$ . As a result, in order to approximate the fluid mesh displacement, we make use of the basis defined on that configuration, namely,  $\{\tilde{N}_A(\tilde{\mathbf{x}}, \tilde{t}) = \hat{N}_A \circ \hat{\phi}_{\tilde{t}}^{-1}(\tilde{\mathbf{x}})\}_{A \in I_f}$ . The fluid mesh displacement, as a function of the  $\tilde{\mathbf{x}}$  configuration variables, becomes

$$\tilde{\mathbf{u}}(\tilde{\mathbf{x}}, \tilde{t}) = \sum_{A \in I_f} \hat{\mathbf{U}}_A(\tilde{t}) \tilde{N}_A(\tilde{\mathbf{x}}, \tilde{t}), \quad (124)$$

and, as a function of the current configuration variables,

$$\hat{\mathbf{u}}(\mathbf{x}, t) = \sum_{A \in I_f} \hat{\mathbf{U}}_A(t) N_A(\mathbf{x}, t). \quad (125)$$

The fluid mesh velocity in the current configuration becomes [see (64)]:

$$\hat{\mathbf{v}}(\mathbf{x}, t) = \sum_{A \in I_f} \frac{\partial \hat{\mathbf{U}}_A}{\partial t}(t) N_A(\mathbf{x}, t). \quad (126)$$

The kinematic compatibility conditions (100) and (110), as well as conditions on the weighting spaces, (101) and (111), are essential for the continuous fluid-structure interaction problem (109) to ensure proper coupling. In the discrete setting there are a variety of ways of incorporating them into the formulation. For example, condition (110) may be imposed weakly (see, e.g., [6, 7]) by constructing additional terms on the fluid-solid interface using ideas emanating from discontinuous Galerkin methods. As a result, incompatible fluid and solid discretizations may be employed. This approach is not adopted here. Instead, in our discrete formulation, we choose to satisfy the above mentioned conditions strongly as described in the following.

Continuity of the discrete ALE mapping at the fluid-solid interface is ensured as follows. Let  $I_{fs} = I_f \cap I_s$  denote the index set of basis functions (and the associated geometry and solution degrees of freedom) associated with the fluid-solid interface. Then, setting  $\hat{\mathbf{U}}_A = \mathbf{U}_A \forall A \in I_{fs}$  gives

$$\begin{aligned} \mathbf{u}|_{\Gamma_0^{fs}} &= \sum_{A \in I_{fs}} \mathbf{U}_A \hat{N}_A|_{\Gamma_0^{fs}} = \sum_{A \in I_{fs}} \hat{\mathbf{U}}_A (\tilde{N}_A \circ \hat{\phi}_{\tilde{t}})|_{\Gamma_0^{fs}} \\ &= \hat{\mathbf{u}} \circ \hat{\phi}_{\tilde{t}}|_{\Gamma_0^{fs}}, \end{aligned} \quad (127)$$

which is precisely the compatibility condition given in (100). Continuity of the ALE mapping, together with continuity of the basis in the reference configuration, assures that the basis

functions in the current configuration are at least  $C^0$ -continuous, and thus,  $H^1$ -conforming. The kinematic compatibility condition (110), which ensures that the fluid particles adhere to the fluid-solid boundary, is satisfied by setting  $\mathbf{V}_A = \partial \mathbf{U}_A / \partial t \forall A \in I_{fs}$  and carrying out the same computation as in (127). The fluid-solid interface condition in (101) is satisfied by setting to zero the weighting functions for the mesh motion problem supported on the fluid-solid interface, while a unique set of basis functions at the fluid-solid interface guarantees (111).

*Remark 4.1* In the theoretical developments and the computations reported in this paper, the same basis functions are used for the pressure as for the fluid particle velocity and the displacement of the fluid region. Unequal-order velocity-pressure discretization may also be employed in order to satisfy the Babuška–Brezzi condition at the discrete level (see [9, 56]). This will not be an issue in our formulation because our variational multiscale formulation attains stability, circumventing the Babuška–Brezzi condition.

#### 4.2 Semi-discrete problem

Let  $\mathcal{V}_h^f, \mathcal{V}_h^s, \mathcal{V}_h^m$  and  $\mathcal{W}_h^f, \mathcal{W}_h^s, \mathcal{W}_h^m$  be the finite dimensional subspaces corresponding to their infinite dimensional counterparts. We approximate the coupled fluid-structure interaction problem (109) as follows: Find  $\{\mathbf{v}, p\} \in \mathcal{V}_h^f, \mathbf{u} \in \mathcal{V}_h^s$ , and  $\hat{\mathbf{u}} \in \mathcal{V}_h^m$  such that  $\forall \{\mathbf{w}^f, q^f\} \in \mathcal{W}_h^f, \forall \mathbf{w}^s \in \mathcal{W}_h^s$ , and  $\forall \mathbf{w}^m \in \mathcal{W}_h^m$ ,

$$\begin{aligned} B_{MS}^f(\{\mathbf{w}^f, q^f\}, \{\mathbf{v}, p\}; \hat{\mathbf{v}}) - F_{MS}^f(\{\mathbf{w}^f, q^f\}) + B^s(\mathbf{w}^s, \mathbf{u}) \\ - F^s(\mathbf{w}^s) + B^m(\mathbf{w}^m, \hat{\mathbf{u}}) - F^m(\mathbf{w}^m) = 0, \end{aligned} \quad (128)$$

where

$$\begin{aligned} B_{MS}^f(\{\mathbf{w}^f, q^f\}, \{\mathbf{v}, p\}; \hat{\mathbf{v}}) &= B^f(\{\mathbf{w}^f, q^f\}, \{\mathbf{v}, p\}; \hat{\mathbf{v}}) \\ &+ \left( (\mathbf{v} - \hat{\mathbf{v}}) \cdot \nabla_x \mathbf{w}^f, \mathbf{v}' \right)_{\tilde{\Omega}_t^f} + \left( \nabla_x q^f, \frac{1}{\rho^f} \mathbf{v}' \right)_{\tilde{\Omega}_t^f} \\ &+ (\nabla_x \cdot \mathbf{w}^f \rho^f \tau_C, \nabla_x \cdot \mathbf{v})_{\tilde{\Omega}_t^f} - (\mathbf{w}^f, \mathbf{v}' \cdot \nabla_x \mathbf{v})_{\tilde{\Omega}_t^f} \\ &- \left( \nabla_x \mathbf{w}^f, \frac{1}{\rho^f} \mathbf{v}' \otimes \mathbf{v}' \right)_{\tilde{\Omega}_t^f} + (\mathbf{v}' \cdot \nabla_x \mathbf{w}^f \bar{\tau}, \mathbf{v}' \cdot \nabla_x \mathbf{v})_{\tilde{\Omega}_t^f} \end{aligned} \quad (129)$$

and

$$F_{MS}^f(\{\mathbf{w}^f, q^f\}) = F^f(\{\mathbf{w}^f, q^f\}). \quad (130)$$



The following definitions are employed in (129):

$$\mathbf{v}' = \tau_M(\mathcal{L}^f(\mathbf{v}, p; \hat{\mathbf{v}}) - \rho^f \mathbf{f}^f) \quad (131)$$

$$\tau_M = \left( \frac{C_I}{\Delta t^2} + (\mathbf{v} - \hat{\mathbf{v}}) \cdot \mathbf{G}(\mathbf{v} - \hat{\mathbf{v}}) + C_I \left( \frac{\mu^f}{\rho^f} \right)^2 \mathbf{G} : \mathbf{G} \right)^{-1/2} \quad (132)$$

$$\tau_C = (\tau_M \mathbf{g} \cdot \mathbf{g})^{-1} \quad (133)$$

$$\bar{\tau} = (\mathbf{v}' \cdot \mathbf{G} \mathbf{v}')^{-1/2} \quad (134)$$

$$G_{ij} = \sum_{k=1}^d \frac{\partial \xi_k}{\partial x_i} \frac{\partial \xi_k}{\partial x_j} \quad (135)$$

$$\mathbf{G} : \mathbf{G} = \sum_{i,j=1}^d G_{ij} G_{ij} \quad (136)$$

$$(\mathbf{v} - \hat{\mathbf{v}}) \cdot \mathbf{G}(\mathbf{v} - \hat{\mathbf{v}}) = \sum_{i,j=1}^d (v_i - \hat{v}_i) G_{ij} (v_j - \hat{v}_j) \quad (137)$$

$$g_i = \sum_{j=1}^d \frac{\partial \xi_j}{\partial x_i}, \quad (138)$$

$$\mathbf{g} \cdot \mathbf{g} = g_i g_i. \quad (139)$$

In the above,  $\frac{\partial \xi}{\partial \mathbf{x}}$  is the inverse Jacobian of the mapping between the isoparametric, or parent, and physical domains,  $\Delta t$  is the time step size, and  $C_I$  is a positive constant, independent of the mesh size, derived from an element-wise inverse estimate (see, e.g., Johnson [40]). In (128) the symbol  $\tilde{\Omega}_t^f$  is used to denote the fact that integrals are taken over element interiors.

Galerkin's method is employed for the solid and mesh motion problems. The fluid formulation (129) emanates from the variational multiscale residual-based turbulence modeling paradigm [2, 4, 7, 11, 29]. The residual-based formulation of fluid flow may be viewed as an extension of well-known stabilized methods, such as SUPG [10]. However, the last term of (129) is not motivated by multiscale arguments, but merely provides additional residual-based stabilization (see Taylor et al. [61]).

### 4.3 Discussion of conservation

In this section we focus on the semi-discrete formulation (128) restricted to the fluid. We show that the formulation satisfies the discrete geometric conservation law and is globally mass-conservative. We also show that our formulation globally conserves momentum under semi-discretization.

The discrete geometric conservation law is satisfied if the formulation preserves a constant fluid velocity in space and time when there are no body forces and the stress tensor is self-equilibrating. Indeed, if a constant particle velocity field is assumed, it is easily seen to satisfy (128) identically.

We note that selecting the advective form was an important constituent in obtaining this result. Furthermore, assuming that a time integrator is chosen such that it “respects” a constant solution, that is, if the velocity field is constant in time, the discrete approximation to the time derivative is zero, then the formulation satisfies the geometric conservation law at a fully discrete level. Any consistent time integrator, including the one employed in this work and described in the following section, should satisfy this condition.

To demonstrate global mass conservation, we set  $\mathbf{w}^f = \mathbf{0}$ ,  $\mathbf{w}^s = \mathbf{0}$ ,  $\mathbf{w}^m = \mathbf{0}$ , and  $q^f = 1$  in (128). This choice leaves us with

$$(1, \nabla_x \cdot \mathbf{v})_{\Omega_t^f} = (1, \mathbf{v} \cdot \mathbf{n}^f)_{\Gamma_t^f} = 0, \quad (140)$$

which is precisely the statement of global mass conservation on the fluid domain. Note that in the solid region the mass-conservation is satisfied a priori due to the choice of the Lagrangian description.

Let  $\mathbf{e}_i$ ,  $i = 1, 2, 3$ , be the  $i$ th Cartesian basis vector. To show global momentum conservation, we set  $\mathbf{w}^f = \mathbf{e}_i$ ,  $\mathbf{w}^s = \mathbf{e}_i$ ,  $\mathbf{w}^m = \mathbf{0}$  in (128) and assume that there are no body or surface forces present. In this case (128) reduces to

$$\left( \mathbf{e}_i, \rho_0^s \frac{\partial^2 \mathbf{u}}{\partial s^2} \right)_{\Omega_0^s} + \left( \mathbf{e}_i, \rho^f \frac{\partial \mathbf{v}}{\partial r} \right)_{\Omega_t^f} + \left( \mathbf{e}_i, \rho^f (\mathbf{v} - \hat{\mathbf{v}}) \cdot \nabla_x \mathbf{v} \right)_{\Omega_t^f} + (\mathbf{e}_i, \mathbf{v}' \cdot \nabla_x \mathbf{v})_{\Omega_t^f} = 0 \quad (141)$$

$$(q^f, \nabla_x \cdot \mathbf{v})_{\Omega_t^f} + \left( \nabla_x q^f, \frac{1}{\rho^f} \mathbf{v}' \right)_{\Omega_t^f} = 0 \quad (142)$$

Integration-by-parts in the third term of (141) gives

$$\left( \mathbf{e}_i, \rho_0^s \frac{\partial^2 \mathbf{u}}{\partial s^2} \right)_{\Omega_0^s} + \left( \mathbf{e}_i, \rho^f \frac{\partial \mathbf{v}}{\partial r} \right)_{\Omega_t^f} + \left( \mathbf{e}_i, \rho^f \{(\mathbf{v} - \hat{\mathbf{v}}) \cdot \mathbf{n}^f\} \mathbf{v} \right)_{\Gamma_t^f} - \left( \mathbf{e}_i, \rho^f \{ \nabla_x \cdot (\mathbf{v} - \hat{\mathbf{v}}) \} \mathbf{v} \right)_{\Omega_t^f} + (\mathbf{e}_i, \mathbf{v}' \cdot \nabla_x \mathbf{v})_{\Omega_t^f} = 0 \quad (143)$$

Using (142) with a specific choice of the test function  $q^f = \rho^f v_i$  gives

$$(\mathbf{e}_i, \rho^f \{ \nabla_x \cdot \mathbf{v} \} \mathbf{v})_{\Omega_t^f} + (\mathbf{e}_i, \mathbf{v}' \cdot \nabla_x \mathbf{v})_{\Omega_t^f} = 0 \quad (144)$$

which, in turn, simplifies (143) to

$$\left( \mathbf{e}_i, \rho_0^s \frac{\partial^2 \mathbf{u}}{\partial s^2} \right)_{\Omega_0^s} + \left( \mathbf{e}_i, \rho^f \frac{\partial \mathbf{v}}{\partial r} \right)_{\Omega_t^f} + \left( \mathbf{e}_i, \rho^f \{(\mathbf{v} - \hat{\mathbf{v}}) \cdot \mathbf{n}^f\} \mathbf{v} \right)_{\Gamma_t^f} + \left( \mathbf{e}_i, \rho^f \{ \nabla_x \cdot \hat{\mathbf{v}} \} \mathbf{v} \right)_{\Omega_t^f} = 0 \quad (145)$$

Note that  $q^f = \rho^f v_i$  is a valid choice because velocity and pressure are approximated by the same discrete spaces. This would not be the case if  $\mathcal{V}_h^p = \mathcal{W}_h^p \not\supset \mathcal{V}_h^v$  component-wise. We proceed by changing variables in the second and fourth terms of Eq. (145) to the referential description as

$$\begin{aligned} & \left( \mathbf{e}_i, \rho_0^s \frac{\partial^2 \mathbf{u}}{\partial s^2} \right)_{\Omega_0^s} + \left( \mathbf{e}_i, \rho^f \frac{\partial \mathbf{v}}{\partial r} \hat{\mathbf{j}} \right)_{\Omega_0^f} \\ & + \left( \mathbf{e}_i, \rho^f \{(\mathbf{v} - \hat{\mathbf{v}}) \cdot \mathbf{n}^f\} \mathbf{v} \right)_{\Gamma_i^f} \\ & + \left( \mathbf{e}_i, \rho^f \{ \hat{\mathbf{j}} \nabla_x \cdot \hat{\mathbf{v}} \} \mathbf{v} \right)_{\Omega_0^f} = 0 \end{aligned} \quad (146)$$

Recognizing that  $\hat{\mathbf{j}} \nabla_x \cdot \hat{\mathbf{v}} = \partial \hat{\mathbf{j}} / \partial r$  [see also Eq. (47)] and combining the second and fourth terms in (146) gives

$$\begin{aligned} & \left( \mathbf{e}_i, \rho_0^s \frac{\partial^2 \mathbf{u}}{\partial s^2} \right)_{\Omega_0^s} + \left( \mathbf{e}_i, \rho^f \frac{\partial \mathbf{v} \hat{\mathbf{j}}}{\partial r} \right)_{\Omega_0^f} \\ & + \left( \mathbf{e}_i, \rho^f \{(\mathbf{v} - \hat{\mathbf{v}}) \cdot \mathbf{n}^f\} \mathbf{v} \right)_{\Gamma_i^f} = 0 \end{aligned} \quad (147)$$

Defining  $\dot{\mathbf{u}} = \partial \mathbf{u} / \partial s$  to be the velocity of the solid, taking the partial time derivative outside of the inner product and changing variables back to the spatial domain in the first two terms of (147) gives

$$\begin{aligned} & \frac{d}{dt} \left( \mathbf{e}_i, \rho_0^s J^{-1} \dot{\mathbf{u}} \right)_{\Omega_t^s} + \frac{d}{dt} \left( \mathbf{e}_i, \rho^f \mathbf{v} \right)_{\Omega_t^f} \\ & + \left( \mathbf{e}_i, \rho^f \{(\mathbf{v} - \hat{\mathbf{v}}) \cdot \mathbf{n}^f\} \mathbf{v} \right)_{\Gamma_i^f} = 0 \end{aligned} \quad (148)$$

By conservation of mass in the Lagrangian description,  $\rho_0^s J^{-1} = \rho_t^s$  [see also Eq. (67)]. Also note that  $\mathbf{v} = \hat{\mathbf{v}}$  on  $\Gamma_t^{fs}$ . With these observations we arrive at

$$\begin{aligned} & \frac{d}{dt} \left( \mathbf{e}_i, \rho_t^s \dot{\mathbf{u}} \right)_{\Omega_t^s} + \left( \mathbf{e}_i, \rho^f \mathbf{v} \right)_{\Omega_t^f} \\ & + \left( \mathbf{e}_i, \rho^f \{(\mathbf{v} - \hat{\mathbf{v}}) \cdot \mathbf{n}^f\} \mathbf{v} \right)_{\Gamma_i^f - \Gamma_t^{fs}} = 0 \end{aligned} \quad (149)$$

which precisely states that the rate of change of the global momentum of the coupled system is balanced by the momentum flux through the boundary of the fluid domain. The momentum flux through the solid boundary is zero due to the choice of the Lagrangian description.

**Remark 4.2** The term  $(\mathbf{w}^f, \mathbf{v}' \cdot \nabla_x \mathbf{v})_{\Omega_t^f}$  was first presented in [61]. For a stationary fluid domain, the conservation-restoring property of this term was shown in [33], where it was pointed out that conservation can be obtained for stabilized methods, but not for Galerkin methods satisfying the Babuška–Brezzi condition [9, 56].

**Remark 4.3** The identity  $\partial \hat{\mathbf{j}} / \partial r = \hat{\mathbf{j}} \nabla_x \cdot \hat{\mathbf{v}}$  plays a critical role in proving momentum conservation. This identity holds true when a functional representation in space and time is simultaneously employed, for example, when space-time

finite elements are employed. On the other hand, lack of satisfaction of the identity induced by a time-integration method will, in general, prevent us from obtaining (147) from (146) and in this case momentum may not be conserved in the fully-discrete case.

#### 4.4 Time integration of the fluid-structure interaction system

In this section, we present the time integration algorithm for semi-discrete Eq. (128). The method is the generalized- $\alpha$  algorithm proposed by Chung and Hulbert [12] for the equations of structural dynamics, and extended to the equations of fluid mechanics by Jansen et al. [36]. In the context of fluid-structure interaction, the generalized- $\alpha$  method was used in [15, 43]. In this section we give details of the method as it applies to the semi-discrete formulation (128).

Let  $\mathbf{U}$ ,  $\dot{\mathbf{U}}$ ,  $\ddot{\mathbf{U}}$ , and  $\mathbf{P}$  denote the vectors of nodal or control variable degrees of freedom of displacements, velocities, velocity time derivatives, and pressure, respectively, of the fluid-structure system. Let  $\mathbf{V}$ ,  $\dot{\mathbf{V}}$ , and  $\ddot{\mathbf{V}}$  denote the vectors of nodal or control variable degrees of freedom of mesh displacements, velocities, and accelerations, respectively. Note that there is no “fluid displacement” in our formulation;  $\dot{\mathbf{U}}$  and  $\ddot{\mathbf{U}}$  are simply labels that we chose for fluid time derivative degrees of freedom. Also note that fluid and solid degrees of freedom are combined in one solution vector. We define three residual vectors corresponding to the momentum, continuity, and mesh motion equations by substituting individual basis functions in place of  $\mathbf{w}^f$ ,  $\mathbf{w}^s$ ,  $q^f$ , and  $\mathbf{w}^m$  in (128) as follows:

$$\mathbf{R}^{\text{mom}} = [\mathbf{R}_{A,i}^{\text{mom}}] \quad (150)$$

$$\begin{aligned} \mathbf{R}_{A,i}^{\text{mom}} &= B_{MS}^f(\{N_A \mathbf{e}_i, 0\}, \{\mathbf{v}, p\}; \hat{\mathbf{v}}) - F_{MS}^f(\{N_A \mathbf{e}_i, 0\}) \\ &+ B^s(\hat{N}_A \mathbf{e}_i, \mathbf{u}) - F^s(\hat{N}_A \mathbf{e}_i) \end{aligned} \quad (151)$$

$$\mathbf{R}^{\text{cont}} = [\mathbf{R}_A^{\text{cont}}] \quad (152)$$

$$\mathbf{R}_A^{\text{cont}} = B_{MS}^f(\{\mathbf{0}, N_A\}, \{\mathbf{v}, p\}; \hat{\mathbf{v}}) - F_{MS}^f(\{\mathbf{0}, N_A\}) \quad (153)$$

$$\mathbf{R}^{\text{mesh}} = [\mathbf{R}_{A,i}^{\text{mesh}}] \quad (154)$$

$$\mathbf{R}_{A,i}^{\text{mesh}} = B^m(\tilde{N}_A \mathbf{e}_i, \hat{\mathbf{u}}) \quad (155)$$

Note that in the above  $\mathbf{R}^{\text{mom}}$  is the combined fluid and solid residual of the linear momentum equations.

The generalized- $\alpha$  time integration algorithm is stated as follows: given  $(\mathbf{U}_n, \dot{\mathbf{U}}_n, \ddot{\mathbf{U}}_n, \mathbf{V}_n, \dot{\mathbf{V}}_n, \ddot{\mathbf{V}}_n)$ , find  $(\mathbf{U}_{n+1}, \dot{\mathbf{U}}_{n+1}, \ddot{\mathbf{U}}_{n+1}, \mathbf{P}_{n+1}, \mathbf{V}_{n+1}, \dot{\mathbf{V}}_{n+1}, \ddot{\mathbf{V}}_{n+1}, \mathbf{U}_{n+\alpha_f}, \dot{\mathbf{U}}_{n+\alpha_f}, \ddot{\mathbf{U}}_{n+\alpha_m}, \mathbf{V}_{n+\alpha_f}, \dot{\mathbf{V}}_{n+\alpha_f}, \ddot{\mathbf{V}}_{n+\alpha_m})$ , such that

$$\begin{aligned} & \mathbf{R}^{\text{mom}}(\mathbf{U}_{n+\alpha_f}, \dot{\mathbf{U}}_{n+\alpha_f}, \ddot{\mathbf{U}}_{n+\alpha_m}, \mathbf{P}_{n+1}, \\ & \times \mathbf{V}_{n+\alpha_f}, \dot{\mathbf{V}}_{n+\alpha_f}, \ddot{\mathbf{V}}_{n+\alpha_m}) = \mathbf{0}, \end{aligned} \quad (156)$$

$$\begin{aligned} & \mathbf{R}^{\text{cont}}(\mathbf{U}_{n+\alpha_f}, \dot{\mathbf{U}}_{n+\alpha_f}, \ddot{\mathbf{U}}_{n+\alpha_m}, \mathbf{P}_{n+1}, \\ & \times \mathbf{V}_{n+\alpha_f}, \dot{\mathbf{V}}_{n+\alpha_f}, \ddot{\mathbf{V}}_{n+\alpha_m}) = \mathbf{0}, \end{aligned} \quad (157)$$

$$\mathbf{R}^{\text{mesh}}(\mathbf{U}_{n+\alpha_f}, \dot{\mathbf{U}}_{n+\alpha_f}, \ddot{\mathbf{U}}_{n+\alpha_m}, \times \mathbf{P}_{n+1}, \mathbf{V}_{n+\alpha_f}, \dot{\mathbf{V}}_{n+\alpha_f}, \ddot{\mathbf{V}}_{n+\alpha_m}) = \mathbf{0}, \quad (158)$$

$$\mathbf{U}_{n+\alpha_f} = \mathbf{U}_n + \alpha_f(\mathbf{U}_{n+1} - \mathbf{U}_n), \quad (159)$$

$$\dot{\mathbf{U}}_{n+\alpha_f} = \dot{\mathbf{U}}_n + \alpha_f(\dot{\mathbf{U}}_{n+1} - \dot{\mathbf{U}}_n), \quad (160)$$

$$\ddot{\mathbf{U}}_{n+\alpha_m} = \ddot{\mathbf{U}}_n + \alpha_m(\ddot{\mathbf{U}}_{n+1} - \ddot{\mathbf{U}}_n), \quad (161)$$

$$\mathbf{V}_{n+\alpha_f} = \mathbf{V}_n + \alpha_f(\mathbf{V}_{n+1} - \mathbf{V}_n), \quad (162)$$

$$\dot{\mathbf{V}}_{n+\alpha_f} = \dot{\mathbf{V}}_n + \alpha_f(\dot{\mathbf{V}}_{n+1} - \dot{\mathbf{V}}_n), \quad (163)$$

$$\ddot{\mathbf{V}}_{n+\alpha_m} = \ddot{\mathbf{V}}_n + \alpha_m(\ddot{\mathbf{V}}_{n+1} - \ddot{\mathbf{V}}_n), \quad (164)$$

$$\dot{\mathbf{U}}_{n+1} = \dot{\mathbf{U}}_n + \Delta t((1-\gamma)\ddot{\mathbf{U}}_n + \gamma\ddot{\mathbf{U}}_{n+1}), \quad (165)$$

$$\mathbf{U}_{n+1} = \mathbf{U}_n + \Delta t\dot{\mathbf{U}}_n + \frac{\Delta t^2}{2}((1-2\beta)\ddot{\mathbf{U}}_n + 2\beta\ddot{\mathbf{U}}_{n+1}), \quad (166)$$

$$\dot{\mathbf{V}}_{n+1} = \dot{\mathbf{V}}_n + \Delta t((1-\gamma)\ddot{\mathbf{V}}_n + \gamma\ddot{\mathbf{V}}_{n+1}), \quad (167)$$

$$\mathbf{V}_{n+1} = \mathbf{V}_n + \Delta t\dot{\mathbf{V}}_n + \frac{\Delta t^2}{2}((1-2\beta)\ddot{\mathbf{V}}_n + 2\beta\ddot{\mathbf{V}}_{n+1}), \quad (168)$$

where  $\Delta t = t_{n+1} - t_n$  is the time step,  $\alpha_f$ ,  $\alpha_m$ ,  $\gamma$ , and  $\beta$  are real-valued parameters that define the method and are selected to ensure second-order accuracy and unconditional stability. For a second-order linear ordinary differential equation system with constant coefficients, which is related to the solid and the mesh parts of the fluid-structure interaction problem, Chung and Hulbert [12] showed that second-order accuracy is attained if

$$\gamma = \frac{1}{2} - \alpha_f + \alpha_m, \quad (169)$$

and

$$\beta = \frac{1}{4}(1 - \alpha_f + \alpha_m)^2, \quad (170)$$

while unconditional stability requires

$$\alpha_m \geq \alpha_f \geq \frac{1}{2}. \quad (171)$$

Results (169) and (171) were also shown by Jansen et al. [36] to hold true for a first order linear ordinary differential equation system with constant coefficients, which is related to the fluid part of the fluid-structure interaction problem. Condition (170) is only applicable to the second-order case. In order to have strict control over high frequency damping,  $\alpha_m$  and  $\alpha_f$  are parameterized by  $\rho_\infty$ , the spectral radius of the amplification matrix at infinitely large time step. Optimal high frequency damping occurs when all the eigenvalues of the amplification matrix take on the same value, namely,  $-\rho_\infty$ . In this case, for the second-order system, Chung and Hulbert [12] derive

$$\alpha_m^c = \frac{2 - \rho_\infty^c}{1 + \rho_\infty^c}, \quad (172)$$

$$\alpha_f^c = \frac{1}{1 + \rho_\infty^c},$$

while for the first order system Jansen et al. [36] give

$$\alpha_m^j = \frac{1}{2} \left( \frac{3 - \rho_\infty^j}{1 + \rho_\infty^j} \right), \quad (173)$$

$$\alpha_f^j = \frac{1}{1 + \rho_\infty^j},$$

where superscripts distinguish the quantities coming from two different methods. The above equations show that for the same values of  $\rho_\infty$  (that is,  $\rho_\infty^c = \rho_\infty^j$ ) there is a mismatch between  $\alpha_m^c$  and  $\alpha_f^c$ . This inconsistency may be eliminated by setting  $\rho_\infty^c = \rho_\infty^j = 1$ , the case of zero high frequency damping corresponding to the midpoint rule, but this is not sufficiently robust for practical calculations. In this work, we adopt expressions (173), making the fluid part of the problem optimally damped, and determine the eigenvalues of the amplification matrix for a second-order linear ordinary differential equation system at infinitely large time step, given by an expression obtained in [12]:

$$\lim_{\Delta t \rightarrow \infty} \lambda = \left\{ \frac{-1 + (\alpha_m^j - \alpha_f^j)}{1 + (\alpha_m^j - \alpha_f^j)}, \frac{-1 + (\alpha_m^j - \alpha_f^j)}{1 + (\alpha_m^j - \alpha_f^j)}, 1 - \frac{1}{\alpha_f^j} \right\}. \quad (174)$$

Substituting (173) into (174), we obtain

$$\lim_{\Delta t \rightarrow \infty} \lambda = \left\{ \frac{-1 - 3\rho_\infty^j}{3 + \rho_\infty^j}, \frac{-1 - 3\rho_\infty^j}{3 + \rho_\infty^j}, -\rho_\infty^j \right\}. \quad (175)$$

The first two eigenvalues are different from  $-\rho_\infty^j$ , but it is a simple matter to show that they are monotone decreasing functions of  $\rho_\infty^j$  and

$$\frac{1}{3} \leq \left| \frac{-1 - 3\rho_\infty^j}{3 + \rho_\infty^j} \right| \leq 1 \quad \forall |\rho_\infty^j| \leq 1. \quad (176)$$

This, in turn, implies that the spectral radius of the amplification matrix never exceeds unity in magnitude and no instabilities are incurred for a second-order system. Note that this choice of parameters maintains second-order accuracy and unconditional stability because conditions (169)–(171) still hold true.

To solve the nonlinear system of Eqs. (156)–(168), we employ Newton's method, which can be viewed as a two-stage predictor–multicorrector algorithm.

### Predictor stage. Set

$$\dot{U}_{n+1,(0)} = \dot{U}_n, \quad (177)$$

$$\ddot{U}_{n+1,(0)} = \frac{(\gamma - 1)}{\gamma} \ddot{U}_n, \quad (178)$$

$$U_{n+1,(0)} = U_n + \Delta t \dot{U}_n + \frac{\Delta t^2}{2} ((1 - 2\beta) \ddot{U}_n + 2\beta \ddot{U}_{n+1,(0)}), \quad (179)$$

$$P_{n+1,(0)} = P_n, \quad (180)$$

$$\dot{V}_{n+1,(0)} = \dot{V}_n \quad (181)$$

$$\ddot{V}_{n+1,(0)} = \frac{(\gamma - 1)}{\gamma} \ddot{V}_n \quad (182)$$

$$V_{n+1,(0)} = V_n + \Delta t \dot{V}_n + \frac{\Delta t^2}{2} ((1 - 2\beta) \ddot{V}_n + 2\beta \ddot{V}_{n+1,(0)}). \quad (183)$$

The subscript 0 on the left-hand side quantities is the iteration index. Note that the predictor is consistent with the generalized- $\alpha$  Eq. (165)–(168).

**Multi-corrector stage.** Repeat the following steps for  $l = 1, 2, \dots, l_{\max}$ .

- (1) Evaluate iterates at the intermediate time levels as

$$U_{n+\alpha_f,(l)} = U_n + \alpha_f (U_{n+1,(l-1)} - U_n) \quad (184)$$

$$\dot{U}_{n+\alpha_f,(l)} = \dot{U}_n + \alpha_f (\dot{U}_{n+1,(l-1)} - \dot{U}_n) \quad (185)$$

$$\ddot{U}_{n+\alpha_m,(l)} = \ddot{U}_n + \alpha_m (\ddot{U}_{n+1,(l-1)} - \ddot{U}_n) \quad (186)$$

$$V_{n+\alpha_f,(l)} = V_n + \alpha_f (V_{n+1,(l-1)} - V_n) \quad (187)$$

$$\dot{V}_{n+\alpha_f,(l)} = \dot{V}_n + \alpha_f (\dot{V}_{n+1,(l-1)} - \dot{V}_n) \quad (188)$$

$$\ddot{V}_{n+\alpha_m,(l)} = \ddot{V}_n + \alpha_m (\ddot{V}_{n+1,(l-1)} - \ddot{V}_n) \quad (189)$$

$$P_{n+1,(l)} = P_{n+1,(l-1)} \quad (190)$$

- (2) Use the intermediate solutions to assemble the residuals of the continuity and momentum equations and the corresponding matrices in the linear system

$$\begin{aligned} \frac{\partial \mathbf{R}^{\text{mom}}}{\partial \ddot{U}_{n+1}} \Delta \ddot{U}_{n+1,(l)} + \frac{\partial \mathbf{R}^{\text{mom}}}{\partial \mathbf{P}_{n+1}} \Delta \mathbf{P}_{n+1,(l)} \\ + \frac{\partial \mathbf{R}^{\text{mom}}}{\partial \ddot{V}_{n+1}} \Delta \ddot{V}_{n+1,(l)} = -\mathbf{R}_{(l)}^{\text{mom}} \end{aligned} \quad (191)$$

$$\begin{aligned} \frac{\partial \mathbf{R}^{\text{con}}}{\partial \ddot{U}_{n+1}} \Delta \ddot{U}_{n+1,(l)} + \frac{\partial \mathbf{R}^{\text{con}}}{\partial \mathbf{P}_{n+1}} \Delta \mathbf{P}_{n+1,(l)} \\ + \frac{\partial \mathbf{R}^{\text{con}}}{\partial \ddot{V}_{n+1}} \Delta \ddot{V}_{n+1,(l)} = -\mathbf{R}_{(l)}^{\text{con}} \end{aligned} \quad (192)$$

$$\begin{aligned} \frac{\partial \mathbf{R}^{\text{mesh}}}{\partial \ddot{U}_{n+1}} \Delta \ddot{U}_{n+1,(l)} + \frac{\partial \mathbf{R}^{\text{mesh}}}{\partial \mathbf{P}_{n+1}} \Delta \mathbf{P}_{n+1,(l)} \\ + \frac{\partial \mathbf{R}^{\text{mesh}}}{\partial \ddot{V}_{n+1}} \Delta \ddot{V}_{n+1,(l)} = -\mathbf{R}_{(l)}^{\text{mesh}} \end{aligned} \quad (193)$$

Solve this linear system using a preconditioned GMRES algorithm (see Saad and Schultz [54]) to a specified tolerance.

- (3) Having solved the linear system, update the iterates as

$$\ddot{U}_{n+1,(l)} = \ddot{U}_{n+1,(l-1)} + \Delta \ddot{U}_{n+1,(l)} \quad (194)$$

$$\dot{U}_{n+1,(l)} = \dot{U}_{n+1,(l-1)} + \gamma \Delta t \Delta \ddot{U}_{n+1,(l)} \quad (195)$$

$$U_{n+1,(l)} = U_{n+1,(l-1)} + \beta (\Delta t)^2 \Delta \ddot{U}_{n+1,(l)} \quad (196)$$

$$\mathbf{P}_{n+1,(l)} = \mathbf{P}_{n+1,(l-1)} + \Delta \mathbf{P}_{n+1,(l)} \quad (197)$$

$$\ddot{V}_{n+1,(l)} = \ddot{V}_{n+1,(l-1)} + \Delta \ddot{V}_{n+1,(l)} \quad (198)$$

$$\dot{V}_{n+1,(l)} = \dot{V}_{n+1,(l-1)} + \gamma \Delta t \Delta \ddot{V}_{n+1,(l)} \quad (199)$$

$$V_{n+1,(l)} = V_{n+1,(l-1)} + \beta (\Delta t)^2 \Delta \ddot{V}_{n+1,(l)} \quad (200)$$

**Remark 4.4** In the context of solution strategies employed to solve the coupled fluid-structural equations, Tezduyar and co-workers (see, e.g., [71]) introduced the following terminology: the block-iterative solution strategy refers to the case when the solution for the three fields (i.e., the solid, fluid and mesh) is obtained in a fully segregated manner; the quasi-direct solution strategy refers to the case when the fluid and solid equations are solved in a coupled fashion, while the mesh motion is solved for separately; finally, the direct strategy refers to the case when the three fields are solved for in a coupled fashion and all the influences of the fields on each other are reflected in the tangent matrix. Adopting the terminology of Tezduyar, the method outlined in this section may be classified as a direct solution strategy.

### 5 Linearization of the fluid-structure interaction equations: a methodology for computing shape derivatives

Derivatives of the momentum, continuity, and mesh motion residuals with respect to solution variables define the so-called *tangent matrices*. In particular, derivatives of the momentum and continuity residuals with respect to the mesh motion variables are referred to as *shape derivatives*. The computation of shape derivative matrices, required for a consistent linearization of the fluid-structure system, has not been extensively studied in the fluid-structure interaction literature, although recently a few references have appeared on the subject (see, e.g., [15, 19]). In this section, we present a detailed methodology for deriving shape derivatives and provide their explicit expressions. Although presented in the ALE context, this methodology is applicable to other fluid-structure formulations.

We begin by introducing notation. Let  $\mathbf{x} = \mathbf{x}(\xi)$  denote the isoparametric mapping at a particular time instant. Let  $\frac{\partial \mathbf{x}}{\partial \xi}$  be the Jacobian of this mapping, let  $\frac{\partial \xi}{\partial \mathbf{x}} = \frac{\partial \mathbf{x}}{\partial \xi}^{-1}$  denote its

inverse, and let  $J_\xi = \det \frac{\partial \mathbf{x}}{\partial \xi}$  be its determinant. A Cartesian basis will be used throughout and operations on vectors and tensors will be expressed through operations on their components in the Cartesian basis. Let  $x_i$  and  $\xi_i$  denote the  $i$ th component of  $\mathbf{x}$  and  $\xi$ , respectively, and  $[\frac{\partial \mathbf{x}}{\partial \xi}]_{ij} = \frac{\partial x_i}{\partial \xi_j}$ , and  $[\frac{\partial \xi}{\partial \mathbf{x}}]_{ij} = \frac{\partial \xi_i}{\partial x_j}$  be the components of the Jacobian and its inverse, respectively. The following identities are standard in nonlinear continuum mechanics (see, e.g., Holzapfel [27]), and will be used in the sequel:

$$\mathcal{D} \left( \frac{\partial \xi_i}{\partial x_j} \right) = - \frac{\partial \xi_i}{\partial x_l} \mathcal{D} \left( \frac{\partial x_l}{\partial \xi_k} \right) \frac{\partial \xi_k}{\partial x_j}, \quad (201)$$

and

$$\mathcal{D} J_\xi = J_\xi \frac{\partial \xi_j}{\partial x_i} \mathcal{D} \left( \frac{\partial x_i}{\partial \xi_j} \right), \quad (202)$$

where  $\mathcal{D}$  denotes a general derivative operator. Summation convention on repeated indices is used throughout. Making use of Eq. (201) and (202) and the chain rule, we obtain

$$\begin{aligned} \mathcal{D} \left( J_\xi \frac{\partial \xi_i}{\partial x_j} \right) &= J_\xi \left( \frac{\partial \xi_l}{\partial x_k} \mathcal{D} \left( \frac{\partial x_k}{\partial \xi_l} \right) \frac{\partial \xi_i}{\partial x_j} \right. \\ &\quad \left. - \frac{\partial \xi_i}{\partial x_l} \mathcal{D} \left( \frac{\partial x_l}{\partial \xi_k} \right) \frac{\partial \xi_k}{\partial x_j} \right), \end{aligned} \quad (203)$$

and, furthermore,

$$\begin{aligned} \mathcal{D} \left( J_\xi \frac{\partial \xi_i}{\partial x_j} \frac{\partial \xi_m}{\partial x_n} \right) &= J_\xi \left\{ \frac{\partial \xi_l}{\partial x_k} \mathcal{D} \left( \frac{\partial x_k}{\partial \xi_l} \right) \frac{\partial \xi_i}{\partial x_j} - \frac{\partial \xi_i}{\partial x_l} \mathcal{D} \left( \frac{\partial x_l}{\partial \xi_k} \right) \frac{\partial \xi_k}{\partial x_j} \right\} \frac{\partial \xi_m}{\partial x_n} \\ &\quad - J_\xi \frac{\partial \xi_i}{\partial x_j} \frac{\partial \xi_m}{\partial x_l} \mathcal{D} \left( \frac{\partial x_l}{\partial \xi_k} \right) \frac{\partial \xi_k}{\partial x_n}. \end{aligned} \quad (204)$$

Our task is to derive expressions for shape derivatives in a term-by-term fashion. We will treat several terms in detail so as to make the underlying procedures clear. Results for the rest of the terms will be stated without derivation. We first consider a derivative of the discrete residual of the momentum equation with respect to mesh acceleration degrees of freedom,

$$\frac{\partial \mathbf{R}^{\text{mom}}}{\partial \ddot{\mathbf{V}}}, \quad (205)$$

which we re-express in component form for convenience as

$$\frac{\partial R_{A,i}^{\text{mom}}}{\partial \ddot{V}_{B,j}}. \quad (206)$$

In (205), time step and iteration superscripts are omitted in the interest of a concise exposition. This derivative is active in the fluid region only, so we consider just the Navier–Stokes contributions to the discrete residual.

### Acceleration term

We begin with the acceleration contribution to the shape derivative matrix, that is

$$\frac{\partial \sum_{e=1}^{N_{el}} \int_{\Omega_e} N_A \rho^f \frac{\partial v_i}{\partial t} d\Omega_e}{\partial \ddot{V}_{B,j}}. \quad (207)$$

In (207)  $N_{el}$  is the number of elements in the fluid mesh and  $\Omega_e$  is the domain of the spatial element.

Taking the partial derivative operator inside the sum over the elements, for a given element  $e$  we obtain

$$\frac{\partial \int_{\Omega_e} N_A \rho^f \frac{\partial v_i}{\partial t} d\Omega_e}{\partial \ddot{V}_{B,j}}. \quad (208)$$

In (208) we cannot take the partial derivative operator inside the integral, as the region of integration directly depends on the mesh motion, that is,  $\Omega_e = \Omega_e(\dot{\mathbf{V}})$ . In order to circumvent this difficulty, we change variables,  $\mathbf{x} \rightarrow \xi$ . With this, (208) becomes

$$\int_{\hat{\Omega}_e} N_A \rho^f \frac{\partial v_i}{\partial t} \frac{\partial J_\xi}{\partial \ddot{V}_{B,j}} d\hat{\Omega}_e, \quad (209)$$

where  $\hat{\Omega}_e$  is the parent domain of the element.

Note that the basis functions, and particle density and acceleration in the parent domain are independent of the mesh motion variables, hence the partial derivative only affects the Jacobian determinant. Using expression (202) in (209) gives

$$\int_{\hat{\Omega}_e} N_A \rho^f \frac{\partial v_i}{\partial t} \frac{\partial \left( \frac{\partial x_k}{\partial \xi_l} \right)}{\partial \ddot{V}_{B,j}} \frac{\partial \xi_l}{\partial x_k} J_\xi d\hat{\Omega}_e \quad (210)$$

The term  $\frac{\partial \left( \frac{\partial x_k}{\partial \xi_l} \right)}{\partial \ddot{V}_{B,j}} \frac{\partial \xi_l}{\partial x_k}$  is analyzed as follows. Recall the definition of  $x_k$ ,

$$x_k = \hat{u}_k + y_k, \quad (211)$$

where  $y_k$  are the reference configuration coordinates of and  $\hat{u}_k$  are the mesh displacements. Then,

$$\frac{\partial x_k}{\partial \xi_l} = \frac{\partial \hat{u}_k}{\partial \xi_l} + \frac{\partial y_k}{\partial \xi_l}, \quad (212)$$

and

$$\frac{\partial \left( \frac{\partial x_k}{\partial \xi_l} \right)}{\partial \ddot{V}_{B,j}} = \frac{\partial \left( \frac{\partial \hat{u}_k}{\partial \xi_l} \right)}{\partial \ddot{V}_{B,j}}, \quad (213)$$

as the second term on the right-hand side of (212) is independent of the mesh motion. The mesh displacement  $\hat{u}_k$  is defined as a linear combination of mesh displacement coefficients and basis functions, that is

$$\hat{u}_k = \sum_{A=1}^{N_{\text{dof}}} V_{A,k} N_A, \quad (214)$$



where  $N_{\text{dof}}$  is the number of element degrees of freedom. The above implies

$$\frac{\partial \left( \frac{\partial x_k}{\partial \xi_l} \right)}{\partial \dot{V}_{B,j}} \frac{\partial \xi_l}{\partial x_k} = \alpha_f \beta \Delta t^2 \frac{\partial N_B}{\partial \xi_l} \frac{\partial \xi_l}{\partial x_j}. \quad (215)$$

In (215) we made use of Newmark update formulas (164) and (168). Inserting (215) into (210), changing variables back to the physical domain, and summing over the elements of the fluid mesh, we finally get

$$\sum_{e=1}^{N_{el}} \alpha_f \beta \Delta t^2 \int_{\Omega_e} N_A \rho^f \frac{\partial v_i}{\partial t} \frac{\partial N_B}{\partial x_j} d\Omega_e. \quad (216)$$

Matrix (216) is the contribution to the shape derivative matrix (205) from the acceleration term present in the discrete momentum equations of the incompressible Navier–Stokes system. It is form-identical to and has the same sparsity structure of the matrices that contribute to the tangents in the analysis of fluids and solids, and its implementation in finite element and isogeometric codes is standard.

#### Advection term

In the acceleration term the coupling between the momentum residual and mesh motion variables occurs through  $J_\xi$ . Other terms of the discrete incompressible Navier–Stokes system exhibit more complex coupling. For example, consider the advective contribution to the momentum residual

$$\begin{aligned} & \sum_{e=1}^{N_{el}} \int_{\Omega_e} N_A \rho^f (v_k - \hat{v}_k) \frac{\partial v_i}{\partial x_k} d\Omega_e \\ &= \sum_{e=1}^{N_{el}} \int_{\Omega_e} N_A \rho^f v_k \frac{\partial v_i}{\partial x_k} d\Omega_e - \sum_{e=1}^{N_{el}} \int_{\Omega_e} N_A \rho^f \hat{v}_k \frac{\partial v_i}{\partial x_k} d\Omega_e. \end{aligned} \quad (217)$$

Restricting the sum to a single element, changing variables to the parent domain, and taking the derivative with respect to the mesh acceleration degrees of freedom gives

$$\begin{aligned} & \int_{\hat{\Omega}_e} N_A \rho^f (v_k - \hat{v}_k) \frac{\partial v_i}{\partial \xi_l} \frac{\partial \left( \frac{\partial \xi_l}{\partial x_k} J_\xi \right)}{\partial \dot{V}_{B,j}} d\hat{\Omega}_e \\ & - \int_{\hat{\Omega}_e} N_A \rho^f \frac{\partial v_i}{\partial \xi_l} \frac{\partial \xi_l}{\partial x_k} \frac{\partial \hat{v}_k}{\partial \dot{V}_{B,j}} J_\xi d\hat{\Omega}_e \end{aligned} \quad (218)$$

Using relation (203) in the first term of (218) gives

$$\begin{aligned} & \int_{\hat{\Omega}_e} N_A \rho^f (v_k - \hat{v}_k) \frac{\partial v_i}{\partial \xi_l} \left( \frac{\partial \xi_m}{\partial x_n} \frac{\partial \left( \frac{\partial x_n}{\partial \xi_m} \right)}{\partial \dot{V}_{B,j}} \frac{\partial \xi_l}{\partial x_k} \right. \\ & \left. - \frac{\partial \xi_l}{\partial x_n} \frac{\partial \left( \frac{\partial x_n}{\partial \xi_m} \right)}{\partial \dot{V}_{B,j}} \frac{\partial \xi_m}{\partial x_k} \right) J_\xi d\hat{\Omega}_e \end{aligned} \quad (219)$$

Changing variables back to the physical domain, taking the sum over the elements in the fluid mesh, and accounting for the second term of (218), we get

$$\begin{aligned} & \sum_{e=1}^{N_{el}} \alpha_f \beta \Delta t^2 \int_{\Omega_e} N_A \rho^f (v_k - \hat{v}_k) \frac{\partial v_i}{\partial x_k} \frac{\partial N_B}{\partial x_j} d\Omega_e \\ & - \sum_{e=1}^{N_{el}} \alpha_f \beta \Delta t^2 \int_{\Omega_e} N_A \rho^f (v_k - \hat{v}_k) \frac{\partial v_i}{\partial x_j} \frac{\partial N_B}{\partial x_k} d\Omega_e \\ & - \sum_{e=1}^{N_{el}} \alpha_f \gamma \Delta t \int_{\Omega_e} N_A \rho^f \frac{\partial v_i}{\partial x_j} N_B d\Omega_e. \end{aligned} \quad (220)$$

#### Pressure stabilization term

As a final example we present the derivation of the shape derivative contribution from the discrete continuity equation, that is

$$\frac{\partial R_A^{\text{cont}}}{\partial \dot{V}_{B,j}}. \quad (221)$$

Consider the pressure contribution from the stabilizing terms, that is

$$\sum_{e=1}^{N_{el}} \int_{\Omega_e} \frac{\partial N_A}{\partial x_i} \frac{\tau_M}{\rho^f} \frac{\partial p}{\partial x_i} d\Omega_e. \quad (222)$$

As in previous developments, restricting to a single element and changing variables in (222) gives

$$\int_{\hat{\Omega}_e} \frac{\partial N_A}{\partial \xi_k} \frac{\partial \xi_k}{\partial x_i} \frac{\tau_M}{\rho^f} \frac{\partial p}{\partial \xi_l} \frac{\partial \xi_l}{\partial x_i} J_\xi d\hat{\Omega}_e. \quad (223)$$

Taking the derivative with respect to the acceleration degrees of freedom and isolating terms that are independent of the mesh motion in (223) we get

$$\begin{aligned} & \int_{\hat{\Omega}_e} \frac{\partial N_A}{\partial \xi_k} \frac{1}{\rho^f} \frac{\partial p}{\partial \xi_l} \frac{\partial \left( \tau_M \frac{\partial \xi_k}{\partial x_i} \frac{\partial \xi_l}{\partial x_i} J_\xi \right)}{\partial \dot{V}_{B,j}} d\hat{\Omega}_e \\ &= \int_{\hat{\Omega}_e} \frac{\partial N_A}{\partial \xi_k} \frac{\tau_M}{\rho^f} \frac{\partial p}{\partial \xi_l} \frac{\partial \left( \frac{\partial \xi_k}{\partial x_i} \frac{\partial \xi_l}{\partial x_i} J_\xi \right)}{\partial \dot{V}_{B,j}} d\hat{\Omega}_e \\ &+ \int_{\hat{\Omega}_e} \frac{\partial N_A}{\partial \xi_k} \frac{1}{\rho^f} \frac{\partial p}{\partial \xi_l} \frac{\partial \xi_k}{\partial x_i} \frac{\partial \xi_l}{\partial x_i} J_\xi \frac{\partial \tau_M}{\partial \dot{V}_{B,j}} d\hat{\Omega}_e. \end{aligned} \quad (224)$$

The last term on the right-hand side of the above expression involves the derivative of  $\tau_M$  with respect to the mesh acceleration degrees of freedom. It is, in principle, present in the tangent matrix and is computable, but in this work it is omitted. In order to handle the first term on the right-hand side of

(224) we employ relation (204) to obtain

$$\begin{aligned} & \int_{\hat{\Omega}_e} \frac{\partial N_A}{\partial \xi_k} \frac{\tau_M}{\rho^f} \frac{\partial p}{\partial \xi_l} \left( \frac{\partial \xi_m}{\partial x_n} \frac{\partial}{\partial \xi_m} \left( \frac{\partial x_n}{\partial \xi_m} \right) \frac{\partial \xi_k}{\partial x_i} \frac{\partial \xi_l}{\partial x_i} \right. \\ & - \frac{\partial \xi_l}{\partial x_n} \frac{\partial}{\partial \xi_m} \left( \frac{\partial x_n}{\partial \xi_m} \right) \frac{\partial \xi_m}{\partial x_i} \frac{\partial \xi_k}{\partial x_i} \\ & \left. - \frac{\partial \xi_k}{\partial x_n} \frac{\partial}{\partial \xi_m} \left( \frac{\partial x_n}{\partial \xi_m} \right) \frac{\partial \xi_m}{\partial x_i} \frac{\partial \xi_l}{\partial x_i} \right) J_{\xi} d\hat{\Omega}_e. \end{aligned} \quad (225)$$

Changing variables back to the physical domain and summing over the fluid domain elements gives the following contribution to the shape derivative

$$\begin{aligned} & \sum_{e=1}^{N_{el}} \alpha_f \beta \Delta t^2 \int_{\Omega_e} \frac{\partial N_A}{\partial x_i} \frac{\tau_M}{\rho^f} \frac{\partial p}{\partial x_i} \frac{\partial N_B}{\partial x_j} d\Omega_e \\ & - \sum_{e=1}^{N_{el}} \alpha_f \beta \Delta t^2 \int_{\Omega_e} \frac{\partial N_A}{\partial x_i} \frac{\tau_M}{\rho^f} \frac{\partial p}{\partial x_j} \frac{\partial N_B}{\partial x_i} d\Omega_e \\ & - \sum_{e=1}^{N_{el}} \alpha_f \beta \Delta t^2 \int_{\Omega_e} \frac{\partial N_A}{\partial x_j} \frac{\tau_M}{\rho^f} \frac{\partial p}{\partial x_i} \frac{\partial N_B}{\partial x_i} d\Omega_e. \end{aligned} \quad (226)$$

As before, these matrices and their implementation in a finite element/isogeometric FSI solver are standard. In what follows, we give, without derivation, expressions for shape derivative contributions from some of the remaining terms in the formulation.

*Pressure gradient term*

$$\begin{aligned} & - \frac{\partial \sum_{e=1}^{N_{el}} \int_{\Omega_e} \frac{\partial N_A}{\partial x_i} p d\Omega_e}{\partial \ddot{V}_{B,j}} \\ & = - \sum_{e=1}^{N_{el}} \alpha_f \beta \Delta t^2 \int_{\Omega_e} \frac{\partial N_A}{\partial x_i} p \frac{\partial N_B}{\partial x_j} - \frac{\partial N_A}{\partial x_j} p \frac{\partial N_B}{\partial x_i} d\Omega_e. \end{aligned} \quad (227)$$

*Viscous stress term*

$$\begin{aligned} & \frac{\partial \sum_{e=1}^{N_{el}} \int_{\Omega_e} \frac{\partial N_A}{\partial x_k} \mu^f \left( \frac{\partial v_i}{\partial x_k} + \frac{\partial v_k}{\partial x_i} \right) d\Omega_e}{\partial \ddot{V}_{B,j}} \\ & = \sum_{e=1}^{N_{el}} \alpha_f \beta \Delta t^2 \int_{\Omega_e} \frac{\partial N_A}{\partial x_k} \mu^f \left( \frac{\partial v_i}{\partial x_k} + \frac{\partial v_k}{\partial x_i} \right) \frac{\partial N_B}{\partial x_j} \\ & - \frac{\partial N_A}{\partial x_j} \mu^f \left( \frac{\partial v_i}{\partial x_k} + \frac{\partial v_k}{\partial x_i} \right) \frac{\partial N_B}{\partial x_k} \\ & - \frac{\partial N_A}{\partial x_k} \mu^f \frac{\partial v_i}{\partial x_j} \frac{\partial N_B}{\partial x_k} - \frac{\partial N_A}{\partial x_k} \mu^f \frac{\partial v_k}{\partial x_j} \frac{\partial N_B}{\partial x_i} d\Omega_e. \end{aligned} \quad (228)$$

*Body force term*

$$\begin{aligned} & \frac{\partial \sum_{e=1}^{N_{el}} \int_{\Omega_e} N_A \rho^f f_i^f d\Omega_e}{\partial \ddot{V}_{B,j}} \\ & = \sum_{e=1}^{N_{el}} \int_{\Omega_e} N_A \rho^f \frac{\partial f_i^f}{\partial \ddot{V}_{B,j}} + \alpha_f \beta \Delta t^2 N_A \rho^f f_i^f \frac{\partial N_B}{\partial x_j} d\Omega_e. \end{aligned} \quad (229)$$

*Continuity constraint term*

$$\begin{aligned} & \frac{\partial \sum_{e=1}^{N_{el}} \int_{\Omega_e} N_A \frac{\partial v_i}{\partial x_i} d\Omega_e}{\partial \ddot{V}_{B,j}} \\ & = \sum_{e=1}^{N_{el}} \alpha_f \beta \Delta t^2 \int_{\Omega_e} N_A \left( \frac{\partial v_i}{\partial x_i} \frac{\partial N_B}{\partial x_j} - \frac{\partial v_i}{\partial x_j} \frac{\partial N_B}{\partial x_i} \right) d\Omega_e. \end{aligned} \quad (230)$$

*Continuity least-squares term*

$$\begin{aligned} & \frac{\partial \sum_{e=1}^{N_{el}} \int_{\Omega_e} \frac{\partial N_A}{\partial x_i} \tau_C \frac{\partial v_k}{\partial x_k} d\Omega_e}{\partial \ddot{V}_{B,j}} \\ & = \sum_{e=1}^{N_{el}} \alpha_f \beta \Delta t^2 \int_{\Omega_e} \frac{\partial N_A}{\partial x_i} \tau_C \frac{\partial v_k}{\partial x_k} \frac{\partial N_B}{\partial x_j} \\ & - \frac{\partial N_A}{\partial x_j} \tau_C \frac{\partial v_k}{\partial x_k} \frac{\partial N_B}{\partial x_i} - \frac{\partial N_A}{\partial x_i} \tau_C \frac{\partial v_k}{\partial x_j} \frac{\partial N_B}{\partial x_k} d\Omega_e. \end{aligned} \quad (231)$$

*Streamline diffusion stabilization term*

$$\begin{aligned} & \frac{\partial \sum_{e=1}^{N_{el}} \int_{\Omega_e} (v_k - \hat{v}_k) \frac{\partial N_A}{\partial x_k} \tau_M (v_l - \hat{v}_l) \frac{\partial v_i}{\partial x_l} d\Omega_e}{\partial \ddot{V}_{B,j}} \\ & = - \sum_{e=1}^{N_{el}} \alpha_f \gamma \Delta t \int_{\Omega_e} \frac{\partial N_A}{\partial x_j} \tau_M (v_k - \hat{v}_k) \frac{\partial v_i}{\partial x_k} N_B \\ & + \frac{\partial N_A}{\partial x_k} \tau_M (v_k - \hat{v}_k) \frac{\partial v_i}{\partial x_j} N_B d\Omega_e \\ & + \sum_{e=1}^{N_{el}} \alpha_f \beta \Delta t^2 \int_{\Omega_e} (v_l - \hat{v}_l) \frac{\partial N_A}{\partial x_l} \tau_M (v_k - \hat{v}_k) \frac{\partial v_i}{\partial x_k} \frac{\partial N_B}{\partial x_j} \\ & - \frac{\partial N_A}{\partial x_j} \tau_M (v_l - \hat{v}_l) \frac{\partial v_i}{\partial x_l} (v_k - \hat{v}_k) \frac{\partial N_B}{\partial x_k} \\ & - (v_l - \hat{v}_l) \frac{\partial N_A}{\partial x_l} \tau_M \frac{\partial v_i}{\partial x_j} (v_k - \hat{v}_k) \frac{\partial N_B}{\partial x_k} d\Omega_e \end{aligned} \quad (232)$$

Contributions to the shape derivative matrix given in this section are implemented in our software. With these contributions to the tangent matrix we observed satisfactory nonlinear convergence of the FSI system within the time step. Including additional terms in the tangent matrix may possibly lead to a better performance of the nonlinear solver for other problem classes of interest.

## 6 NURBS-based isogeometric analysis

In NURBS-based isogeometric analysis, a physical domain in  $\mathbb{R}^d$ ,  $d = 2, 3$ , is defined as a union of subdomains, also referred to as patches. A patch, denoted by  $\Omega$ , is an image under a NURBS mapping of a parametric domain  $(0, 1)^d$ , that is

$$\Omega = \{\mathbf{x} \in \mathbb{R}^d \mid \mathbf{x} = \mathbf{F}(\xi), \forall \xi \in (0, 1)^d\}. \quad (233)$$

The geometrical mapping  $\mathbf{F}(\xi)$  is defined as a linear combination of rational basis functions and real coefficients as

$$\mathbf{F}(\xi) = \sum_{i \in I} R_i(\xi) \mathbf{C}_i. \quad (234)$$

In (234),  $\mathbf{C}_i \in \mathbb{R}^d$  are the control points,  $I$  is the index set of control points, and their multi-linear interpolation is referred to as the control mesh. The basis functions  $R_i(\xi)$  have the following structure:

$$R_i(\xi) = \frac{B_i(\xi)}{w(\xi)}, \quad (235)$$

where the  $B_i(\xi)$ 's are tensor-product B-spline basis functions defined on  $(0, 1)^d$ ,

$$w(\xi) = \sum_{i \in I} w_i B_i(\xi) \quad (236)$$

is the so-called weighting function, and the  $w_i$ 's are the strictly positive weights. Due to the point-wise non-negativity of the B-spline functions and the strict positivity of the weights,  $w(\xi)$  is strictly positive.

In isogeometric analysis the geometry generation step entails constructing the initial control mesh, which, in conjunction with the underlying basis functions, defines the “exact geometry” parametrically. For purposes of analysis, the isoparametric concept is invoked (see [28]). The basis for the solution space in the physical domain, denoted by  $\phi_i(\mathbf{x})$ , is defined through a “push-forward” of the rational basis functions in (235) to the physical domain, namely

$$N_i(\mathbf{x}) = R_i(\mathbf{F}^{-1}(\mathbf{x})) = R_i \circ \mathbf{F}^{-1}(\mathbf{x}). \quad (237)$$

This construction guarantees that all rigid body modes and constant strain states are represented exactly in the discrete space, which, in turn, is critical for structural analysis. Coefficients of the basis functions in (237), defining the solution fields in question (e.g., displacement, velocity, etc.), are called control variables.

There are NURBS analogues of finite element  $h$ - and  $p$ -refinement, and there is also a variant of  $p$ -refinement, which is termed  $k$ -refinement, in which the continuity of functions is systematically increased. This seems to have no analogue in traditional finite element analysis but is a feature shared by some meshless methods. As a consequence of the parametric definition of the “exact” geometry at the coarsest level of

discretization, mesh refinement can be performed automatically without changing the geometry and its parameterization, and without further communication with an external description of the geometry (e.g., CAD). From the standpoint of analysis, these are significant benefits. For the details of the analysis framework based on NURBS, the corresponding mathematical theory, and mesh refinement and degree elevation algorithms, the reader is referred to [5, 30].

## 7 Numerical examples: selected benchmark computations

In this section we present two numerical examples, computed using the NURBS-based discretization. In these cases we use relatively thin structures for which we employ solid elements with four  $C^1$ -continuous quadratic basis functions in the through-thickness direction. For modeling shell-like structures with solid NURBS elements, see [30].

### 7.1 Flow over an elastic beam attached to a fixed square block

Our first example is a two-dimensional flow over a thin elastic beam attached to a rigid and fixed square block. This benchmark was proposed by Wall [73] in order to test accuracy and robustness of newly emerging fluid-structure interaction procedures. The problem setup is illustrated in Fig. 3. The flow is driven by a uniform velocity of magnitude 51.3 cm/s prescribed at the inflow. Lateral boundaries are assigned zero normal velocity and zero tangential traction. A zero traction boundary condition is applied at the outflow. The fluid density and viscosity are set to  $1.18 \times 10^{-3}$  g/cm<sup>3</sup> and  $1.82 \times 10^{-4}$  g/(cm s), respectively, resulting in a flow at Reynolds number  $Re = 100$  based on the edge length of the square block. The density of the elastic beam is 0.1 g/cm<sup>3</sup>, and the Young's modulus and Poisson's ratio are  $2.5 \times 10^6$  g/(cm s<sup>2</sup>) and 0.35, respectively. Problem

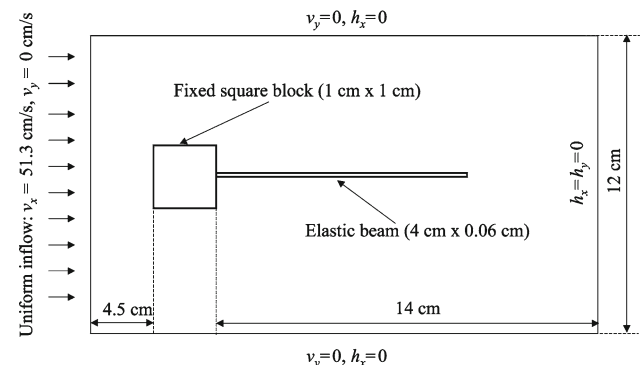


**Fig. 3** Flow over an elastic beam attached to a fixed square block. Problem setup

**Fig. 4** Flow over an elastic beam attached to a fixed square block. Fluid domain mesh employed in the computations

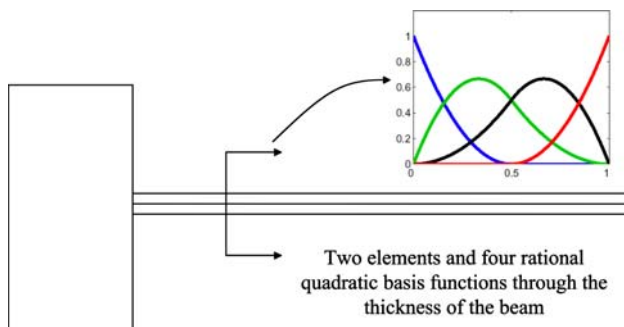
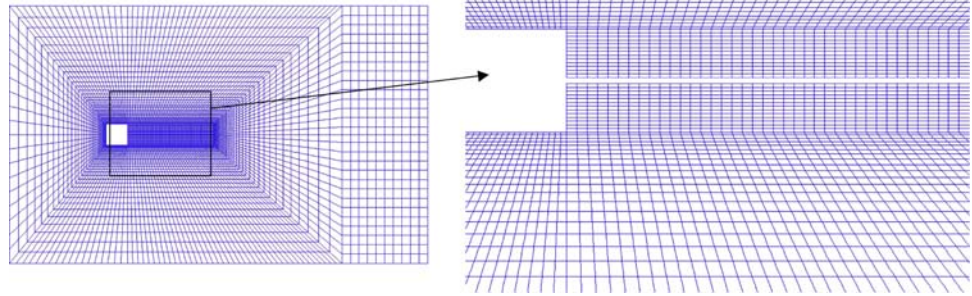


**Fig. 5** Flow over an elastic beam attached to a fixed square block. Through-thickness discretization of the beam

dimensions, material, and boundary data are taken from the original reference.

The mesh for this example is comprised of 6936 quadratic NURBS elements and is shown in Fig. 4. The through-thickness discretization of the beam is shown in Fig. 5. The mesh is allowed to move everywhere in the flow domain except at the inflow and around the square block, where it is held fixed, and also at the lateral boundaries and the outflow boundary where the mesh is constrained not to move in the normal direction.

Figure 6 shows velocity vectors and pressure contours of the solution at various times. The flow features are characteristic of  $Re = 100$  flow. Vortices that are being shed from the square block are impinging on the bar eventually forcing it into an oscillating motion. The bar experiences large deformations necessitating careful mesh movement. The fictitious elastic Lamé parameters for the mesh motion problem are defined as

$$\mu^m = \frac{E^m}{2(1 + \nu^m)} \quad (238)$$

$$\lambda^m = \frac{\nu^m E^m}{(1 + \nu^m)(1 - 2\nu^m)}, \quad (239)$$

where  $E^m$  and  $\nu^m$  are the mesh Young's modulus and Poisson's ratio, respectively. For this computation we take  $\nu^m =$

0.3 and define the mesh Young's modulus to be

$$E^m = E_0^m J_\xi^{-1}, \quad (240)$$

where, as in the previous section,  $J_\xi$  is the Jacobian determinant of the isoparametric element mapping and  $E_0^m$  is set to unity. Expression (240) represents the so-called Jacobian stiffening procedure (see, e.g., [48, 70]), which preserves good mesh quality throughout the entire simulation (see the smaller frames in Fig. 6).

The onset of vortex shedding in a numerical calculation depends on many factors, such as convergence tolerances, round-off, etc., some of which are very difficult or even impossible to control. As a result, meaningful comparisons with other computations are only possible when the flow reaches a stable periodic state. Comparison with the results of Wall [73] for a periodic flow regime is shown in Fig. 7. As may be inferred from the figure, the amplitude of the tip displacement is between 1 and 1.5 cm, and the period is approximately 0.33 s. These results are in agreement with those of Wall [73], despite the differences in discretizations and solid modeling. Wall used bilinear finite elements for the fluid discretization, biquadratic finite elements with one element through the thickness for the solid discretization, and incompatible meshes at the fluid-solid interface. In our computations, a compatible quadratic NURBS mesh is employed with a similar number of degrees of freedom as that of Wall. The St. Venant–Kirchhoff model for the elastic beam was used in [73], in contrast to a neo-Hookean with penalty formulation employed here.

## 7.2 Inflation of a balloon

This three-dimensional benchmark example, proposed by Tezduyar and Sathe [66], belongs to a class of problems known as flows in enclosed domains. In this case, the boundary of the fluid subdomain is composed of two parts: an inflow and a fluid-solid interface. For incompressible fluids this imposes the following condition: the inflow flow rate must equal the rate of change of the fluid domain volume



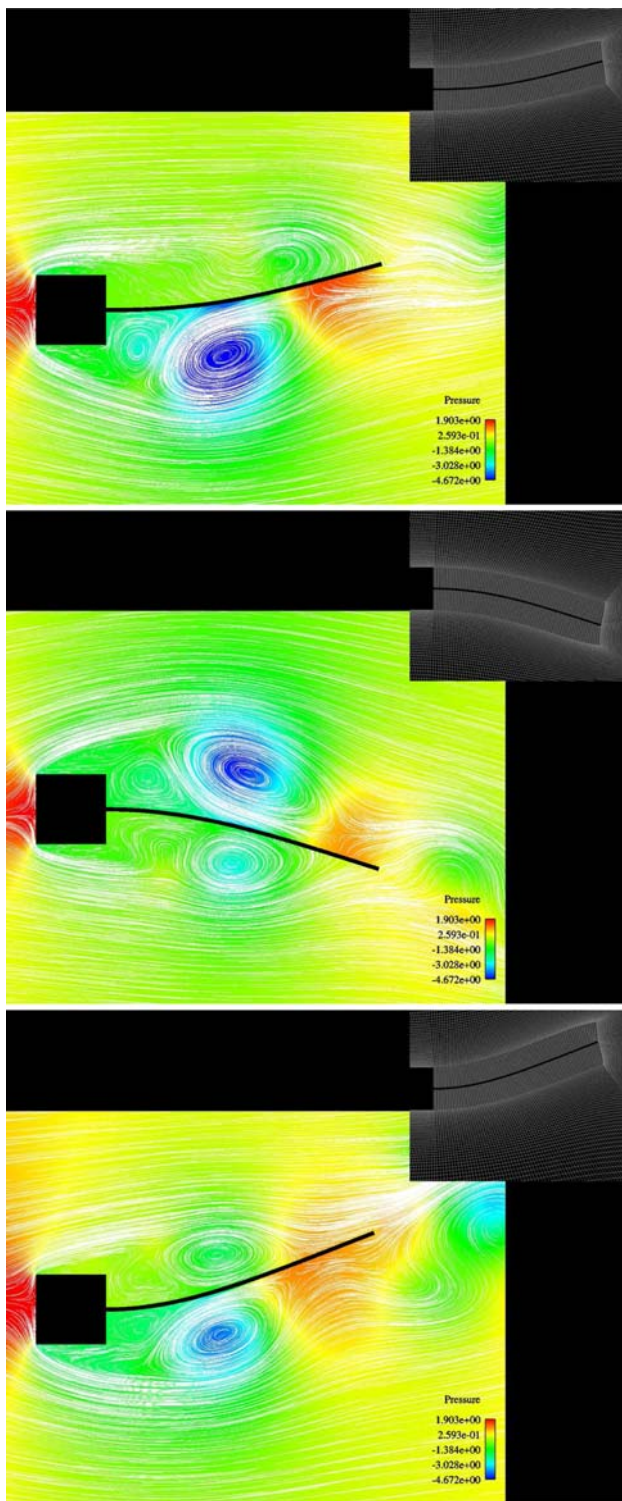


**Fig. 6** Flow over an elastic beam attached to a fixed square block. Larger frames: fluid velocity vectors superposed on top of the pressure plotted on a moving domain. Smaller frames: deformed fluid mesh

(see, e.g., [42]). In loosely coupled approaches, where the solution of the fluid and the solid subproblems are obtained in a staggered fashion, this condition is lost during subiteration

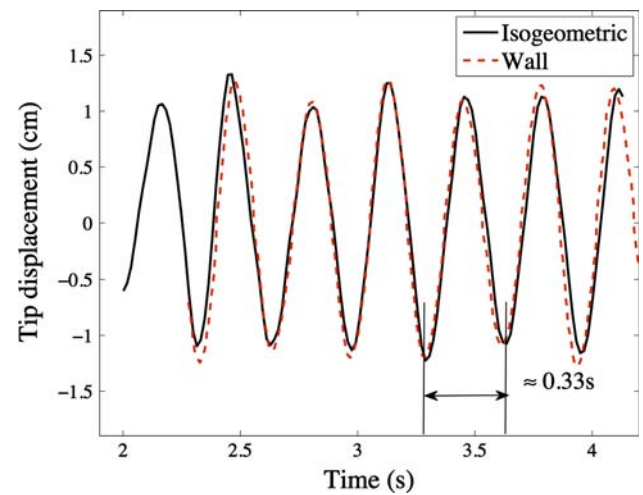


**Fig. 7** Flow over an elastic beam attached to a fixed square block. Displacement of the tip of the mid-plane of the bar as a function of time. Results of Wall [73] are plotted for comparison using a dashed line

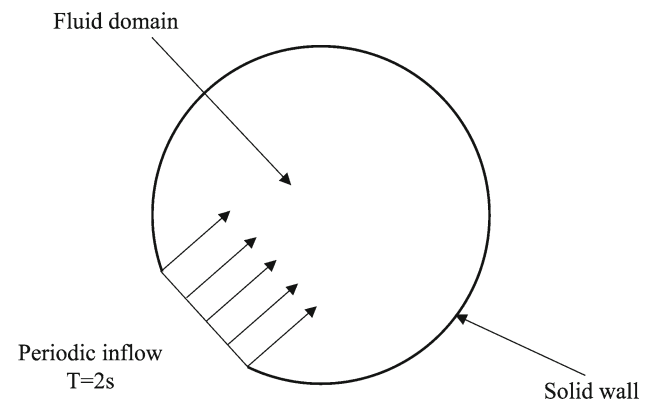


**Fig. 8** Inflation of a balloon. Problem setup

often leading to divergence of the calculations. In the context of loosely-coupled methods, special procedures were devised that led to convergent behavior for this class of problems (see [42]). In this section we show that the strongly-coupled procedures advocated in this work have no difficulty dealing with this situation.

The problem setup is illustrated in Fig. 8. An initially spherical balloon is inflated, as shown in the figure. The inflow velocity is governed by a cosine function with a period of 2 s and amplitude ranging from 0 to 2 m/s. The problem geometry, boundary conditions and material parameters are taken from [66]. In the initial configuration the diameter of the balloon is 2 m, the diameter of the circular hole is 0.6245 m, and the thickness of the balloon is 0.002 m. The density, Young's modulus, and Poisson's ratio for the balloon are  $100 \text{ kg/m}^3$ ,  $1,000 \text{ N/m}^2$ , and 0.4, respectively. The density and viscosity of the fluid correspond to that of air at room temperature and are taken to be  $1 \text{ kg/m}^3$  and  $1.5 \times 10^{-5} \text{ kg/(m s)}$ . The mesh



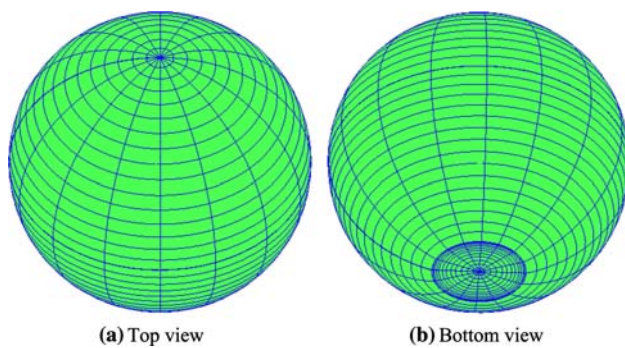


**Fig. 9** Inflation of a balloon. NURBS mesh of the balloon in both top and bottom views

of the initial configuration, comprised of 10,336 quadratic NURBS elements, is shown in Fig. 9. Note that, because NURBS are used to define the analysis-suitable geometry, the spherical balloon is represented exactly.

For the purposes of mesh motion, we take advantage of the parametric definition of the geometry. We take  $E^m$  [i.e., the elastic modulus of the mesh motion problem; see Eq. (238)–(239)] to be an exponentially increasing function of the parameter defining the radial direction, thus effectively “stiffening” the fluid elements near the fluid-solid boundary.

The computation is advanced for 14 inflow cycles, during which the volume of the balloon grows by a factor of approximately five with respect to its initial value. Figures 10–12 show snapshots of fluid velocity vectors superposed on the pressure contours at a planar cut through the diameter of the sphere. The flow starts out as being radially symmetric, although it is apparent that the symmetry of the solution breaks down towards the end of the computation. This is not surprising as the Reynolds number of the flow, based on the initial diameter of the balloon and the maximum inflow speed, is  $4 \times 10^5$ , which is quite high. For the purposes of plotting the results, the geometry and solution variables are interpolated with linear hexahedral finite elements at knots and midpoints of knot intervals. The meshes displayed in Figs. 10, 11 and 12 correspond to the linear hexahedral representation.

Figure 13a shows the inflow flowrate versus the rate of change of the fluid domain volume, which are expected to be the same. On the scale of the plot they are indistinguishable. A closer examination of the error between the inflow flowrate and the rate of change of the fluid domain volume reveals that the relative error in the quantities is on the order of  $10^{-4} - 10^{-3}$ , which is attributable to the fact that the nonlinear equations are solved to a tolerance (see Fig. 13b). Note that the results are, on average, slightly less accurate during the last few periods of the simulation, which is attributable to the loss of radial symmetry in the solution. Also note that the error has the same sign, that is, the rate of change of the fluid domain volume is always greater than

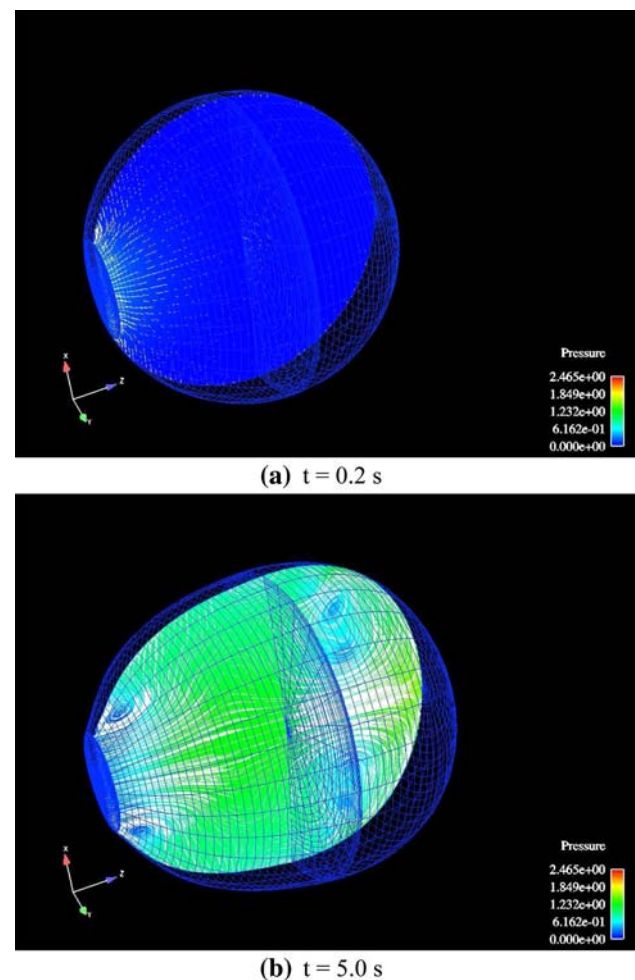


**Fig. 10** Inflation of a balloon. Mesh deformation and fluid velocity vectors superposed on the pressure plotted on a planar cut through the diameter of the balloon

the inflow flow rate. This suggests that in the discrete setting there is a tendency of the balloon to expand slightly faster (i.e., overcompensate) than dictated by the inflow flowrate.

## 8 Computation of vascular flows

In this section we describe the construction of arterial geometries. We then make an assessment of the solid model [presented in (75)–(80)] in describing the behavior of arterial wall tissue. Finally, we present results of the fluid-structure interaction calculation of a patient-specific abdominal aortic aneurysm.

### 8.1 Construction of the arterial geometry

Blood vessels are tubular objects and so we employ a sweeping method to construct meshes for isogeometric analysis.

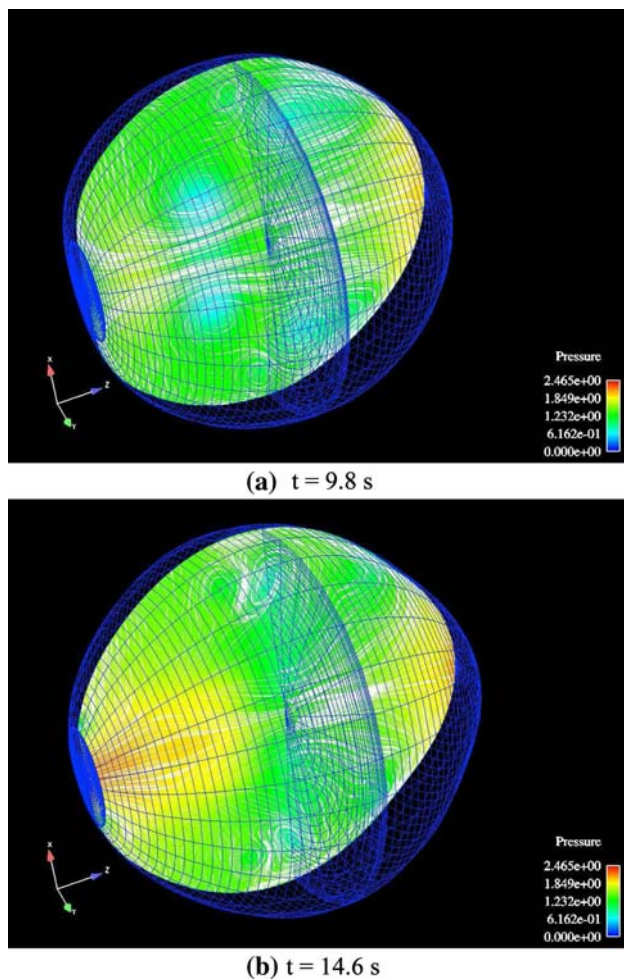


**Fig. 11** Inflation of a balloon. Mesh deformation and fluid velocity vectors superposed on the pressure plotted on a planar cut through the diameter of the balloon

A solid NURBS description of a single arterial branch is obtained by extrusion of a circular curve along the vessel path and filling the volume radially inward. Arterial systems engender various branchings and intersections, which are handled with a template-based approach described in detail in [74]. Application of these procedures generate multi-patch, trivariate descriptions of patient-specific arterial geometries that are also analysis suitable.

A central feature of our approach is a construction of an arterial cross-section template that is based on the NURBS definition of the circular surface. Here we focus on the construction of the cross-section template as it relates to fluid-structure interaction analysis of arterial blood flow. We identify the area occupied by the blood, or the fluid region, and the arterial wall, or the solid region. Fluid and solid regions are separated by the luminal surface, or the fluid-solid boundary. Figure 14 shows an example of a NURBS mesh of a circular cross-section with both fluid and solid regions present. NURBS elements are defined as areas enclosed between

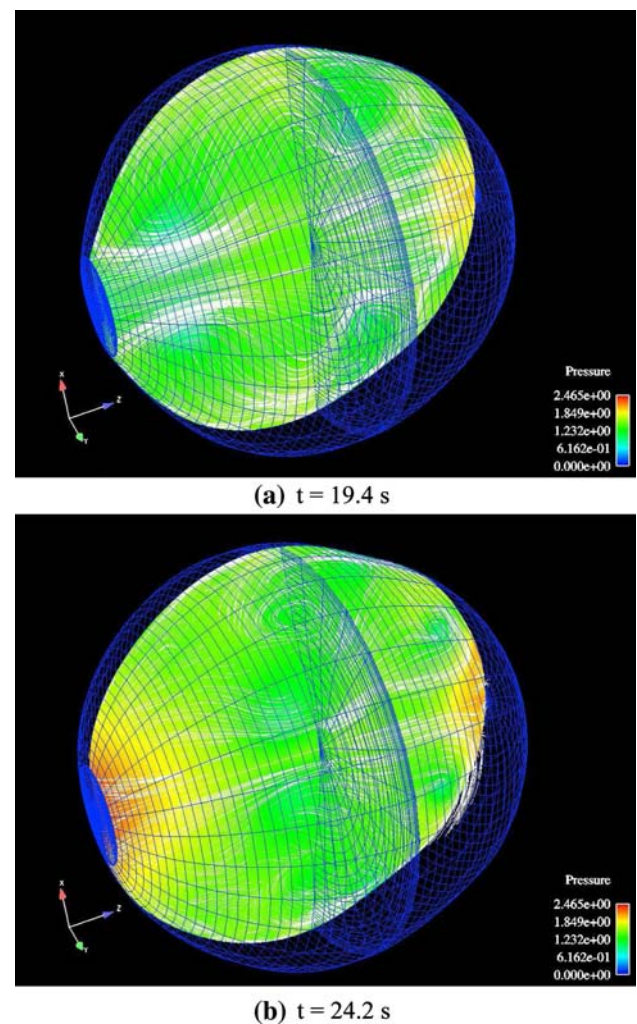


**Fig. 12** Inflation of a balloon. Mesh deformation and fluid velocity vectors superposed on the pressure plotted on a planar cut through the diameter of the balloon

isoparametric lines. Note that the isoparametric lines correspond to radial and circumferential directions. For purposes of analysis we separate the fluid and the solid region by a  $C^0$  line as the solution is not expected to have regularity beyond  $C^0$  at the interface.

Human arteries are not exactly circular, hence projection of the template onto the true surface is necessary. Only control points that govern the cross-section geometry are involved in the projection process, while the underlying parametric description of the cross-section stays unchanged. The end result of this construction is shown in Fig. 14, which illustrates the mapping of the template cross-section onto the patient-specific geometry. Here the isoparametric lines are somewhat distorted so as to conform to the true geometry, while the topology of the fluid and solid subdomains is preserved along with their interface. It is worth noting that cross-sections of healthy arteries are nearly circular, so in this

**Fig. 13** Inflation of a balloon. (a) Plot of the volumetric inflow rate (solid line) versus the rate of change of the fluid domain volume (circles). (b) Plot of the relative error in the flow rates that is attributable to convergence tolerances employed in the calculations

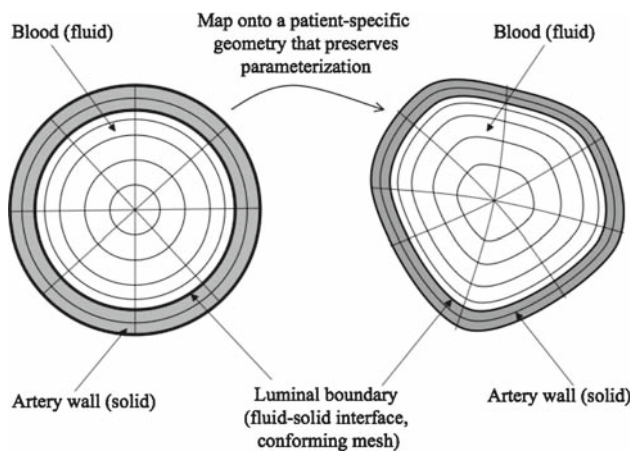
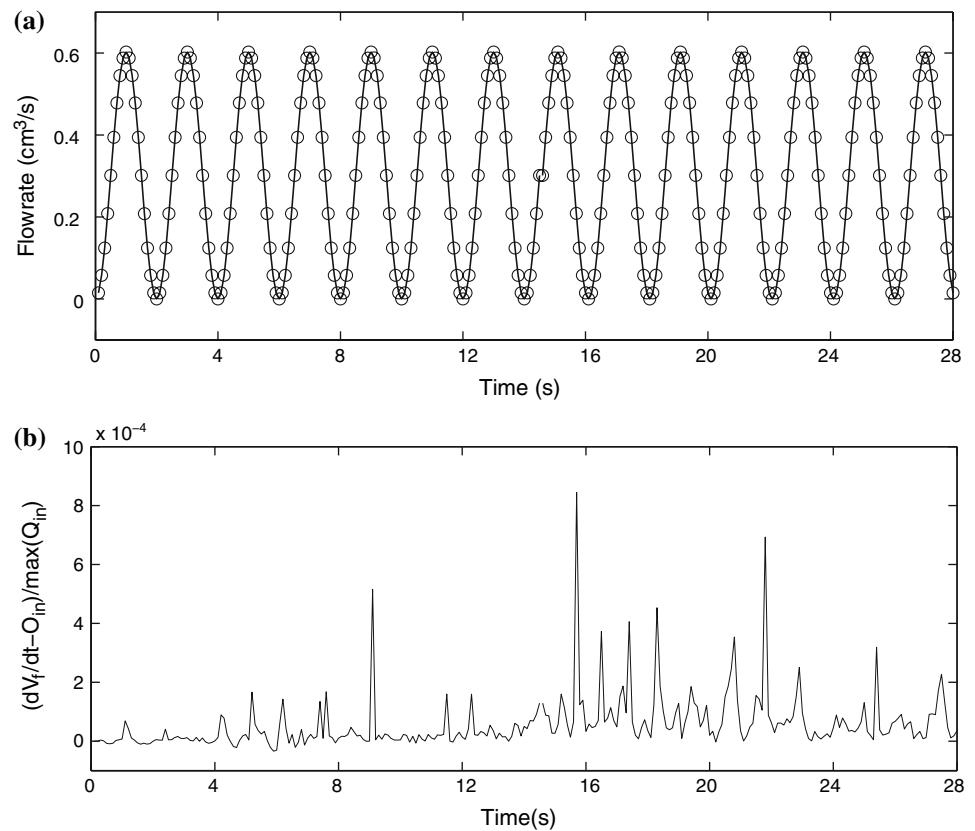


**Fig. 14** Arterial cross-section template based on a NURBS mesh of a circle that is subsequently mapped onto a subject-specific geometry. Fluid and solid regions are identified and separated by an interface. For analysis purposes, basis functions are made  $C^0$ -continuous at the fluid-solid boundary. Note that the topology of the fluid and the solid subdomains remains unchanged

case little distortion of the template is required to accurately capture the true geometry.

Compared to the standard finite element method, the described method has significant benefits for analysis of blood flow in arteries, both in terms of accuracy and implementational convenience. It is well known in fluid mechanics that steady, laminar, incompressible flow in a straight circular

pipe that is driven by a constant pressure gradient develops a parabolic profile in the radial direction and has no dependence on the circumferential or axial directions. NURBS discretizations proposed in this paper, in contrast to standard finite element discretizations, are capable of exactly representing this solution profile.

Parametric definition of the geometry is not only attractive from the mesh refinement point of view, is also beneficial in arterial blood flow applications for the following reasons:

- (1) In the fluid region structured boundary layer meshes near arterial walls may be constructed. This is crucial for overall accuracy of the fluid-structural simulation as well as for obtaining accurate wall quantities, such as shear stress, which plays an important role in predicting the onset and development of vascular disease.
- (2) In the solid region it allows for a natural representation of material anisotropy of the arterial wall because the parametric coordinates are aligned with the axial, circumferential and wall-normal directions. See [26] for arterial wall material modeling which accounts for anisotropic behavior.
- (3) Fluid-structure interaction applications involve motion of the fluid domain. As described previously, this is typically done by solving an auxiliary fictitious elastic boundary value problem for mesh movement (see, e.g., [37,3]). Parametric mesh definition in the fluid region



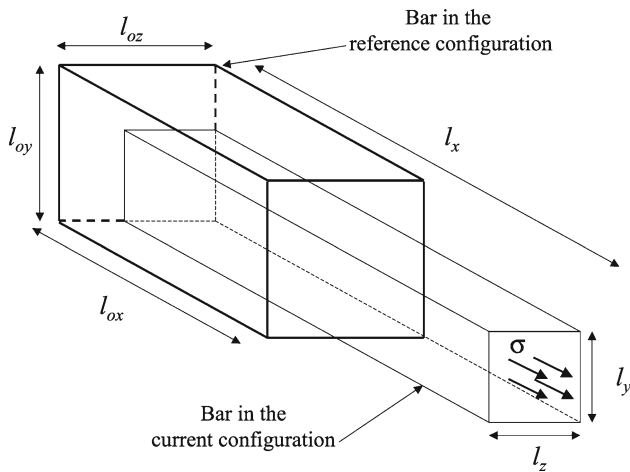


**Fig. 15** Setup for a uniaxial stress state

allows for a straightforward specification of these elastic mesh parameters. For example, for problems of this type we “stiffen” the mesh in the radial direction so as to preserve boundary layer elements during mesh motion.

## 8.2 Investigation of the solid model for a range of physiological stresses

We begin by examining the behavior of the material model presented in (75)–(80) on a simple state of uniaxial stress. We first consider a bar with an applied stress in the  $x$ -direction, denoted by  $\sigma$ , and zero stress in the the orthogonal directions, as illustrated in Fig. 15. We will then relate this situation to that of a pre-stressed artery in the physiologically relevant range. For this type of loading, the deformation tensors  $\mathbf{F}$  and  $\mathbf{C}$  are constant and diagonal, that is

$$\mathbf{F} = \begin{bmatrix} F_{11} & 0 & 0 \\ 0 & F_{22} & 0 \\ 0 & 0 & F_{33} \end{bmatrix} = \begin{bmatrix} l_x/l_{0x} & 0 & 0 \\ 0 & l_y/l_{0y} & 0 \\ 0 & 0 & l_z/l_{0z} \end{bmatrix} \quad (241)$$

and

$$\begin{aligned} \mathbf{C} = \mathbf{F}^T \mathbf{F} &= \begin{bmatrix} C_{11} & 0 & 0 \\ 0 & C_{22} & 0 \\ 0 & 0 & C_{33} \end{bmatrix} \\ &= \begin{bmatrix} (l_x/l_{0x})^2 & 0 & 0 \\ 0 & (l_y/l_{0y})^2 & 0 \\ 0 & 0 & (l_z/l_{0z})^2 \end{bmatrix} \end{aligned} \quad (242)$$

where  $l_x, l_y, l_z$  are the current lengths of the bar and  $l_{0x}, l_{0y}, l_{0z}$  are the original lengths of the bar in the  $x, y$  and  $z$ -directions, respectively. We assume that  $l_{0y} = l_{0z}$  and  $l_y = l_z$  due to symmetry, and use this assumption in the upcoming developments.

From considerations of equilibrium, the Cauchy stress tensor becomes

$$\boldsymbol{\sigma} = \begin{bmatrix} \sigma & 0 & 0 \\ 0 & 0 & 0 \\ 0 & 0 & 0 \end{bmatrix} \quad (243)$$

and, by the transformation of stress formula (71),

$$\begin{aligned} \mathbf{S} = J \mathbf{F}^{-1} \boldsymbol{\sigma} \mathbf{F}^{-T} &= \begin{bmatrix} J \sigma F_{11}^{-2} & 0 & 0 \\ 0 & 0 & 0 \\ 0 & 0 & 0 \end{bmatrix} \\ &= \begin{bmatrix} J \sigma C_{11}^{-1} & 0 & 0 \\ 0 & 0 & 0 \\ 0 & 0 & 0 \end{bmatrix}, \end{aligned} \quad (244)$$

with  $J = F_{11} F_{22} F_{33} = F_{11} F_{22}^2 = (C_{11} C_{22}^2)^{1/2}$ , where we used the assumption of symmetry in the second equality. Substituting (244) into (80) and rearranging terms, we arrive at the following  $2 \times 2$  system of nonlinear equations

$$\begin{aligned} \sigma &= \mu^s C_{11}^{1/6} C_{22}^{-5/3} (1 - 1/3(C_{11} + 2C_{22})C_{11}^{-1}) \\ &\quad + 1/2\kappa^s (C_{11} C_{22}^2 - 1) C_{11}^{-1/2} C_{22}^{-1} \end{aligned} \quad (245)$$

$$\begin{aligned} 0 &= \mu^s C_{11}^{-1/3} C_{22}^{-2/3} (1 - 1/3(C_{11} + 2C_{22})C_{22}^{-1}) \\ &\quad + 1/2\kappa^s (C_{11} C_{22}^2 - 1) C_{22}^{-1}. \end{aligned} \quad (246)$$

The shear and bulk moduli  $\mu^s$  and  $\kappa^s$  are computed from Eq. (84) as

$$\mu^s = \mu^l \quad (247)$$

$$\kappa^s = \lambda^l + \frac{2}{3}\mu^l, \quad (248)$$

where

$$\mu^l = \frac{E}{2(1 + \nu)} \quad (249)$$

$$\lambda^l = \frac{\nu E}{(1 + \nu)(1 - 2\nu)} \quad (250)$$

are the Lamé coefficients:  $E$  is Young’s modulus, and  $\nu$  is Poisson’s ratio. We set  $E = 4.144 \times 10^6 \text{ dyn/cm}^2 = 3.11 \times 10^3 \text{ mmHg}$  and  $\nu = 0.45$ .

The relevant values of  $\sigma$  corresponding to the physiologically-realistic range of intramural pressure are obtained using the following analysis. We approximate the arterial cross-section as a hollow cylinder. Let  $R_i$  and  $R_o$  denote its inner and outer radii. We also assume that a pressure of magnitude  $p_0$  is applied at the inner wall of the cylinder, as shown in Fig. 16. We assume an approximately constant state of stress through the thickness, as shown in Fig. 16. From force equilibrium considerations it follows that

$$2R_i p_0 = 2\sigma t \quad (251)$$

where  $t = R_o - R_i$  is the thickness of the arterial wall. Solving for  $\sigma$ , we get

$$\sigma = p_0 R_i / t. \quad (252)$$

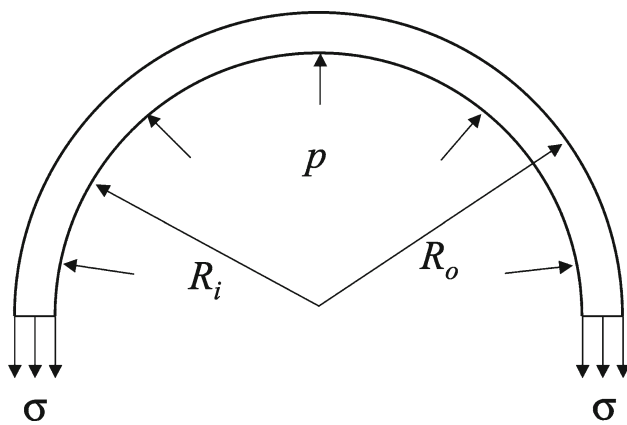


**Fig. 16** Equilibrium on a cylinder with imposed internal pressure

Assuming a thickness-to-radius ratio of 15% and  $p_0$  varying from 80 mmHg to 120 mmHg, we get the physiologically-realistic stress ranging from approximately 530 mmHg to 800 mmHg.

As a part of this analysis we also extract effective tangent moduli at different levels of deformation as follows. The tangent modulus is defined as

$$C = \frac{\partial \sigma}{\partial \epsilon}, \quad (253)$$

with  $\epsilon$  defined as

$$\epsilon = \frac{l_x - l_{0x}}{l_x} = 1 - F_{11}^{-1} = 1 - C_{11}^{-1/2}. \quad (254)$$

We solve (245) and (246) numerically for  $C_{11}$  and  $C_{22}$  for  $\sigma$  ranging from 0 mmHg to 2500 mmHg, and compute the strain according to (254). The plot of stress  $\sigma$  versus strain  $\epsilon$  is shown in Fig. 17. Physiological ranges of stresses and strains due to intramural pressure are indicated in the figure by dashed lines. Note that the stress-strain curve exhibits convex behavior throughout the range of loadings considered, showing stiffening with deformation. Also note that for the physiological range of stresses the deviation from a linearized stress-strain relationship is not significant. We also compute a numerical derivative of  $\sigma$  with respect to  $\epsilon$  in order to evaluate the effective tangent modulus. Note that the equivalent tangent stiffness is higher at the level of deformation caused by the physiological stress as compared to the tangent stiffness in the undeformed configuration. Also note that, as expected, the value of the tangent stiffness in the undeformed configuration is exactly the value of Young's modulus used to define the solid model parameters. Figure 18 shows the plot of elastic energy  $\psi$  versus strain  $\epsilon$ . We believe that this analysis justifies using the model in fluid-structure interaction analysis of arteries. We also feel that it supports the hypotheses behind the coupled momentum method of Figueroa et al. [20]. Obviously, significant improvements are possible.

However, the present model is both qualitatively and quantitatively reasonable for the following application.

### 8.3 Flow in a patient-specific abdominal aortic aneurysm

Patient-specific geometry is obtained from 64-slice CT angiography courtesy of T. Kvamsdal and J.H. Kaspersen of SINTEF, Norway. The geometrical model, which contains most major branches of a typical abdominal aorta, is shown in Fig. 19a. Note that one of the renal arteries is missing in the model indicating that the patient has only one kidney. The fluid properties are:  $\rho^f = 1.06 \text{ g/cm}^3$ ,  $\mu^f = 0.04 \text{ g/cm s}$ . The solid has the density  $\rho^s = 1 \text{ g/cm}^3$ , Young's modulus,  $E = 4.144 \times 10^6 \text{ dyn/cm}^2$ , and Poisson's ratio,  $\nu = 0.45$ . The model coefficients  $\mu^s$  and  $\kappa^s$  are obtained using relationships from the previous section. The computational mesh, consisting of 44892 quadratic NURBS elements, is shown in Fig. 19c. Two quadratic NURBS elements and four  $C^1$ -

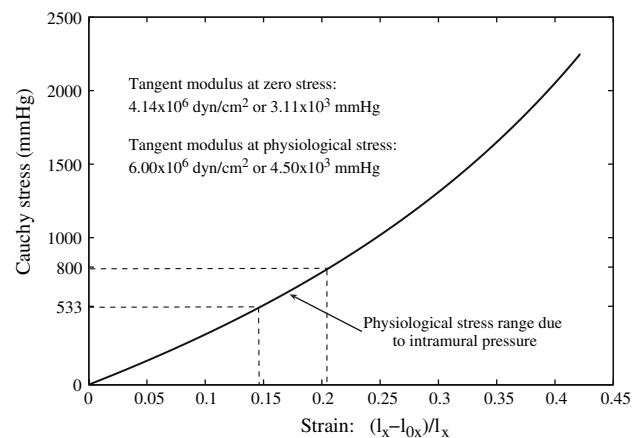


**Fig. 17** Cauchy stress plotted against strain for the material model used in the abdominal aorta simulation. Physiological range of stresses and strains due to intramural pressure are indicated by dashed lines

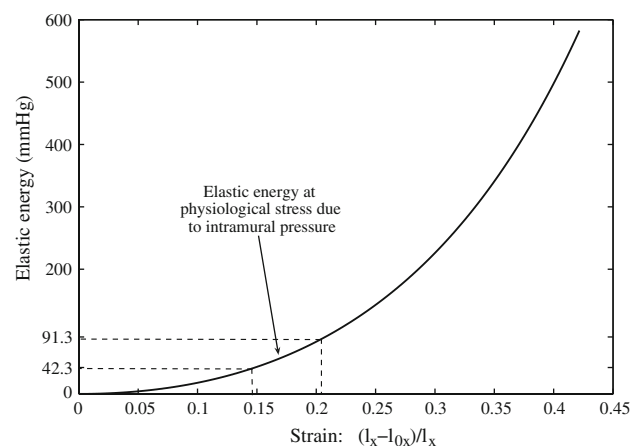
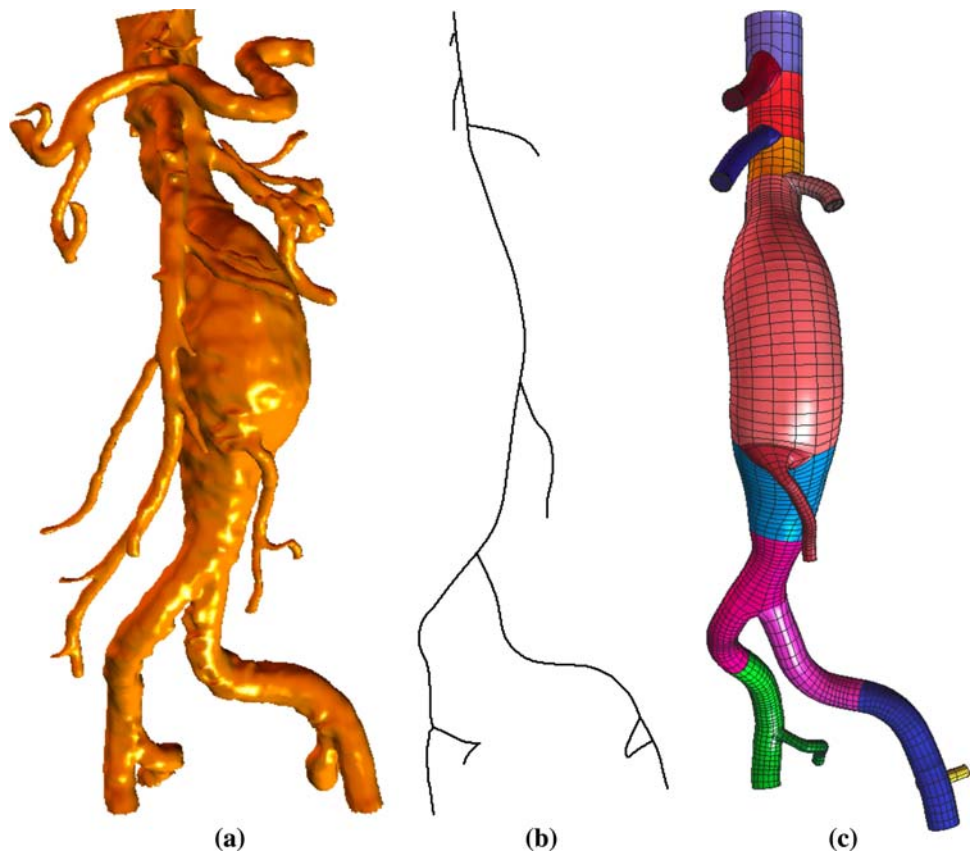


**Fig. 18** Elastic energy plotted against strain for the material model used in the abdominal aorta simulation. Physiological range of energies and strains due to intramural pressure are indicated by dashed lines



**Fig. 19** Flow in a patient-specific abdominal aorta with aneurysm. **a** Patient-specific imaging data; **b** Skeleton of the NURBS mesh; **c** Smoothed and truncated NURBS model and mesh. In **c**, every NURBS patch is assigned a different color. For more details of geometrical modeling for isogeometric analysis of blood flow the reader is referred to [74]



continuous basis functions are used for through-thickness resolution of the arterial wall. For the purposes of mesh motion, parametric stiffening in the radial direction is employed as for the inflation of a balloon problem.

### 8.3.1 Imposition of initial and boundary conditions

A periodic flow waveform, with period  $T = 1.05$  s, is applied at the inlet of the aorta, while resistance boundary conditions are applied at all outlets. The solid is fixed at the inlet and at all outlets. Material and flow rate data, as well as resistance values are taken from Figueroa et al. [20]. Wall thickness for this model is taken to be 15% of the nominal radius of each cross-section of the fluid domain model.

In order to ensure medically-realistic response, resistance boundary conditions must be applied in such a way that physiological pressure levels are present in the system at all times. This is accomplished by making use of the following variant of the resistance boundary condition (see also Figueroa et al. [20], Vignon-Clementel et al. [72], and Heywood et al. [25]). At every outlet face  $\Gamma_a$  we set

$$\mathbf{n}^T \boldsymbol{\sigma} \mathbf{n} = C_a \int_{\Gamma_a} \mathbf{v} \cdot \mathbf{n} d\Gamma_a + p_0, \quad (255)$$

$$\boldsymbol{\tau}_1^T \boldsymbol{\sigma} \mathbf{n} = 0, \quad (256)$$

$$\boldsymbol{\tau}_2^T \boldsymbol{\sigma} \mathbf{n} = 0 \quad (257)$$

where  $\mathbf{n}$  is the outward unit normal, and  $\boldsymbol{\tau}_1$  and  $\boldsymbol{\tau}_2$  are mutually orthogonal unit tangent vectors on the outlet face. The above boundary conditions state that normal stress on the outlet face is a linear function of the flowrate through the face, while both tangential stresses are zero. The  $C_a$ 's are the so-called resistance constants. They are positive, and are, in principle, different from outlet to outlet, reflecting the resistance of different blood vessels.  $p_0$  in (255) is responsible for imposing physiologically realistic pressure level in the vessels, even at zero flow through the outlet faces. For the computations reported in this section  $p_0$  is set to 85 mmHg, as in [20]. We impose boundary conditions (255) weakly by adding the following terms to the variational formulation (109)

$$+ \sum_a \left\{ \left( \int_{\Gamma_a} \mathbf{w}^f \cdot \mathbf{n} d\Gamma_a \right) \left( C_a \int_{\Gamma_a} \mathbf{v} \cdot \mathbf{n} d\Gamma_a + p_0 \right) \right\}$$

where the sum is taken over all the outlet faces with prescribed resistance conditions.

We initialize our computations as follows. We start with an un-pressurized configuration, set and maintain the inflow

velocity consistent with the inflow flowrate at  $t = 0$ , and gradually increase the pressure level in the system by raising  $p_0$  in (255) from zero to the physiologically realistic value of 85 mmHg. This is done for one or two cycles. Once the physiological pressure level is attained, we begin computing with the time-varying inflow boundary condition until periodic-in-time response is attained. This usually takes four or five cycles.

**Remark 8.1** Recent efforts to increase the efficiency of arterial FSI computations by performing a series of so-called “pre-FSI” computations were reported in [67].

**Remark 8.2** In reference [68] the authors propose a strategy to compute the so-called “estimated zero-pressure arterial geometry.” This is done in an effort to reconcile the fact that the patient-specific arterial geometry, often times taken as the reference geometry, corresponds to the pressurized configuration, while in the majority of the proposed material models the reference configuration is assumed to be stress-free.

### 8.3.2 Numerical results

After a nearly periodic-in-time solution was attained, simulation data was collected for postprocessing. Figures 20 and 21 show snapshots of the velocity field plotted on the moving domain at various times during the heart cycle. The flow field is quite complex and fully three-dimensional, especially in diastole. Velocity magnitude is largest near the inflow and is significantly lower in the aneurysm region. This occurs in part due to the fact that a significant percentage of the flow goes to the upper branches of the abdominal aorta. There is also an increase in the cross-sectional area of the vessel associated with the aneurysm, resulting in a decreased flow velocity in this region.

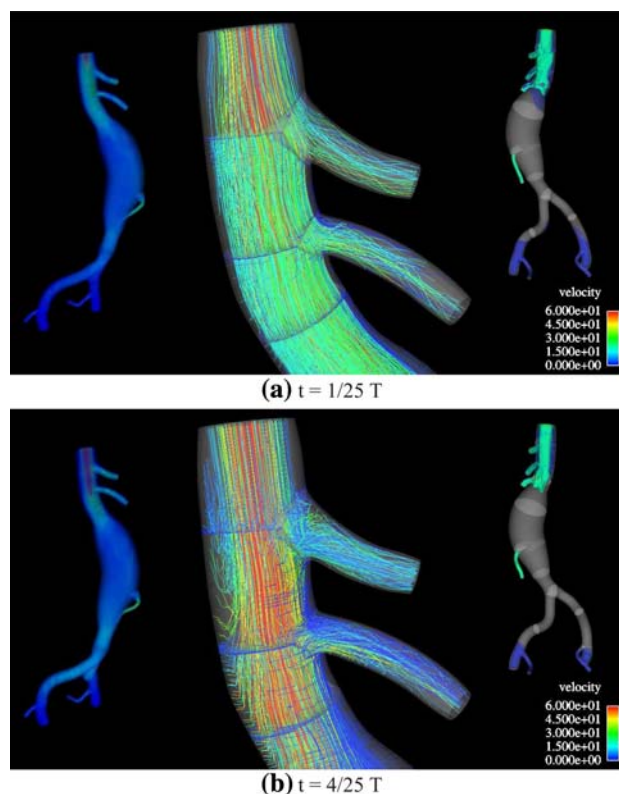
Figure 22 shows the magnitude of the wall shear stress (i.e., the tangential component of the fluid or solid traction vector) averaged over a cycle. Note that the wall shear stress is significantly lower in the aneurysm region than in the upper portion of the aorta and at branches. Also note the smoothness of the stress contours due to the NURBS representation of the geometry and solution fields.

Figure 23 shows the oscillatory shear index (OSI) at the luminal surface. OSI is defined as (see, e.g., [62,63]),

$$\text{OSI} = \frac{1}{2} \left( 1 - \frac{\tau_{\text{mean}}}{\tau_{\text{abs}}} \right), \quad (258)$$

where, denoting by  $\tau_s$  the wall shear stress vector,

$$\tau_{\text{mean}} = \left| \frac{1}{T} \int_0^T \tau_s dt \right|, \quad (259)$$



**Fig. 20** Flow in a patient-specific abdominal aorta with aneurysm. Large frame: fluid velocity vectors colored by their magnitude in the vicinity of the celiac and superior mesenteric arteries. Left small frame: volume rendering of the velocity magnitude. Right small frame: fluid velocity isosurfaces

and

$$\tau_{\text{abs}} = \frac{1}{T} \int_0^T |\tau_s| dt. \quad (260)$$

Note that, in contrast to the wall shear stress, OSI is largest in the aneurysm region, especially along the posterior wall, suggesting that wall shear stress is highly oscillatory there due to the recirculating flow. Low time-averaged wall shear stress, in combination with high shear stress temporal oscillations, as measured by the OSI, are indicators of the regions of high probability of occurrence of atherosclerotic disease. Figure 24 shows the distribution of flow among the branches. The outflow lags the inflow due to the distensibility of the arterial wall. The overall flow distribution and the time lag are in qualitative agreement with results in [3,20].

## 9 Conclusions

We have presented a monolithic isogeometric fluid-structure interaction formulation. The fluid subdomain was assumed to be governed by the incompressible Navier–Stokes equations and the solid subdomain was assumed to be

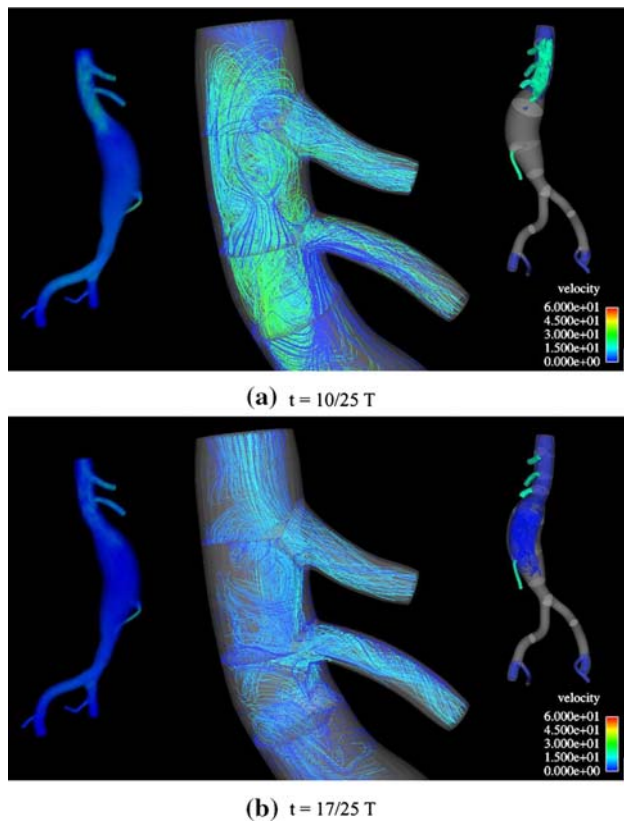


**Fig. 21** Flow in a patient-specific abdominal aorta with aneurysm. Large frame: fluid velocity vectors colored by their magnitude in the vicinity of the celiac and superior mesenteric arteries. Left small frame: volume rendering of the velocity magnitude. Right small frame: fluid velocity isosurfaces

governed by a fully-nonlinear hyperelastic constitutive equation. The arbitrary Lagrangian–Eulerian description was utilized for the fluid subdomain and the Lagrangian description was employed in the solid subdomain. We derived various basic forms of the equations for the solid and fluid from fundamental continuum mechanics relations written with respect to domains in arbitrary motion. We investigated the conservation properties of the formulation and concluded that mass conservation and the geometric conservation law are satisfied in the fully-discrete case, whereas momentum conservation is only satisfied up to truncation errors in a certain key relation introduced by the time integration method. Details of the implementation are described including the calculation of shape derivatives appearing in the tangent operator. NURBS-based isogeometric analysis models were employed in the numerical calculation of three test cases: flow over an elastic beam, the inflation of a balloon, and blood flow in a patient-specific model of an abdominal aortic aneurysm. The formulation behaved robustly in all cases.

**Acknowledgments** Support of the Office of Naval Research Contract N00014-03-0263, Dr. Luise Couchman, contract monitor, is gratefully

acknowledged. Y. Bazilevs and Y. Zhang were also partially supported by the J.T. Oden ICES Postdoctoral Fellowship at the Institute for Computational Engineering and Sciences. This support is gratefully acknowledged. We would also like to thank Karla Vega of the Texas Advanced Computing Center (TACC) [60] for her help with visualization and Dr. Samrat Goswami of ICES for his help with building the aneurysm geometry.

## Appendix A: A note on exterior calculus

The fact that clocks are synchronized in the space-time mapping does engender simplifications over the general asynchronous case. This may be inferred from the structure of  $\hat{F}^{(4)}$  and its inverse. See (2) and (5). Time synchronization means, roughly speaking, that space-like hypersurfaces, that is constant in  $t$  and  $r$  slices of  $Q_x$  and  $Q_y$  are orthogonal to the  $t$  and  $r$  coordinate axes, respectively. In the general case, one must rely on exterior calculus and differential forms, as noted in [1].

A coordinate-free exterior calculus version of the proof of (9) is given by the following calculations. To understand these, one needs to be familiar with the exterior derivative  $d$ ; the interior product of a differential form  $\alpha$  with a (contravariant) vector field  $v$ , denoted  $i_v \alpha$ ; the Lie derivative of a differential form,  $\mathcal{L}_v \alpha = di_v \alpha + i_v d\alpha$ ; and the pull-back by a mapping  $\phi$ , denoted,  $\phi^*$ . Differential forms are skew-symmetric covariant tensor fields. The Piola transform is expressed as follows:

$$\gamma_y^{(4)} = \hat{J}^{(4)} \hat{\phi}^{(4)*} \gamma_x^{(4)}. \quad (\text{A.1})$$

By comparing this form of the Piola transform with (8), we recognize that the pull-back of a vector field is simply multiplication by  $\hat{F}^{(4)-1}$ .

With these preliminaries we can establish the following result which is the basis of the change of variables formula:

$$\begin{aligned} \hat{\phi}^{(4)*} i_{\gamma_x^{(4)}} dQ_x &= i_{\hat{\phi}^{(4)*} \gamma_x^{(4)}} \hat{\phi}^{(4)*} dQ_x \\ &= i_{\hat{\phi}^{(4)*} \gamma_x^{(4)}} \hat{J}^{(4)} dQ_y \\ &= i_{\hat{J}^{(4)} \hat{\phi}^{(4)*} \gamma_x^{(4)}} dQ_y \\ &= i_{\gamma_y^{(4)}} dQ_y \end{aligned} \quad (\text{A.2})$$

Note that  $dQ_x$  and  $dQ_y$  are space-time volume forms, that is 4-forms, and  $i_{\gamma_x^{(4)}} dQ_x$  and  $i_{\gamma_y^{(4)}} dQ_y$  are 3-forms. Vector fields in 4-dimensions are isomorphic to 3-forms, as given by the preceding expressions. This is written as  $\gamma_x^{(4)} \rightarrow *\gamma_x^{(4)} = i_{\gamma_x^{(4)}} dQ_x$  and  $\gamma_y^{(4)} \rightarrow *\gamma_y^{(4)} = i_{\gamma_y^{(4)}} dQ_y$ .

**Fig. 22** Flow in a patient-specific abdominal aorta with aneurysm. Magnitude of wall shear stress averaged over a cycle plotted in three different views

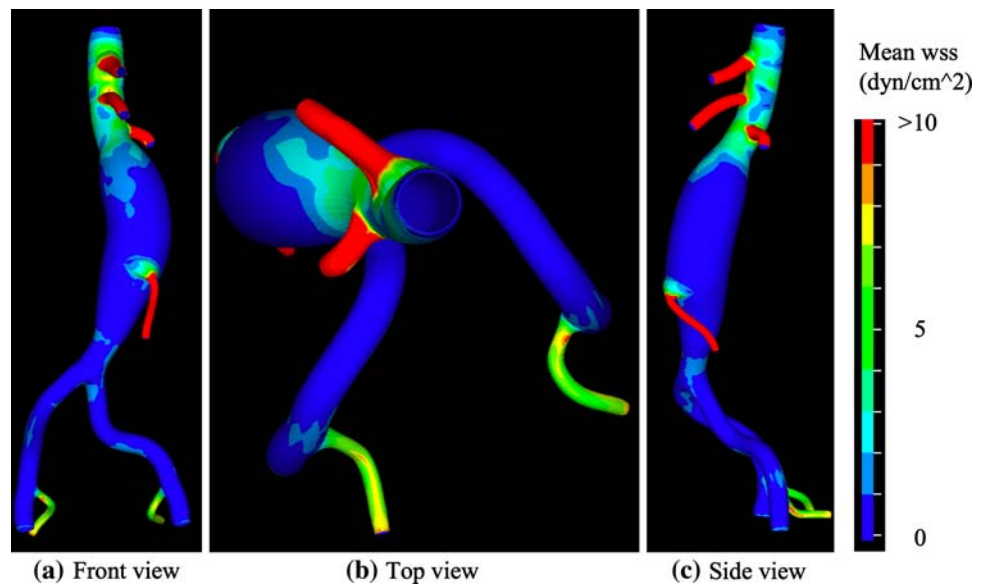
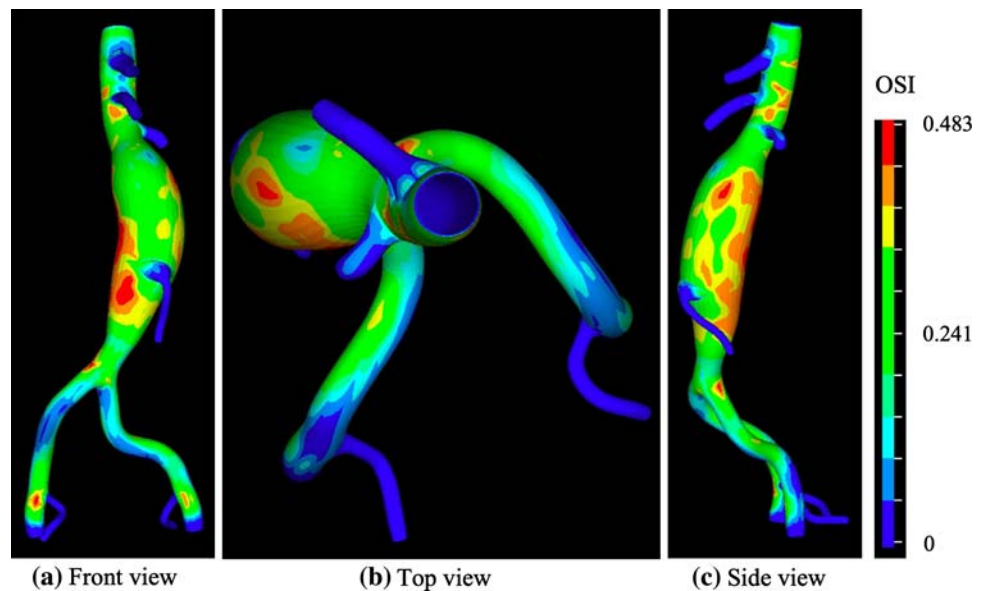


**Fig. 23** Flow in a patient-specific abdominal aorta with aneurysm. Oscillatory shear index (OSI) plotted in three different views



With these preliminaries we have

$$\begin{aligned}
 \nabla_y^{(4)} \cdot \gamma_y^{(4)} dQ_y &= \mathcal{L}_{\gamma_y^{(4)}} dQ_y \\
 &= d(i_{\gamma_y^{(4)}} dQ_y) \\
 &= d(\hat{\phi}^{(4)*} i_{\gamma_x^{(4)}} dQ_x) \\
 &= \hat{\phi}^{(4)*} d(i_{\gamma_x^{(4)}} dQ_x) \\
 &= \hat{\phi}^{(4)*} \mathcal{L}_{\gamma_x^{(4)}} dQ_x \\
 &= \hat{\phi}^{(4)*} (\nabla_x^{(4)} \cdot \gamma_x^{(4)} dQ_x) \\
 &= \nabla_x^{(4)} \cdot \gamma_x^{(4)} \circ \hat{\phi}^{(4)*} \hat{\phi}^{(4)*} dQ_x \\
 &= \nabla_x^{(4)} \cdot \gamma_x^{(4)} \circ \hat{\phi}^{(4)*} \hat{J}^{(4)} dQ_y. \tag{A.3}
 \end{aligned}$$

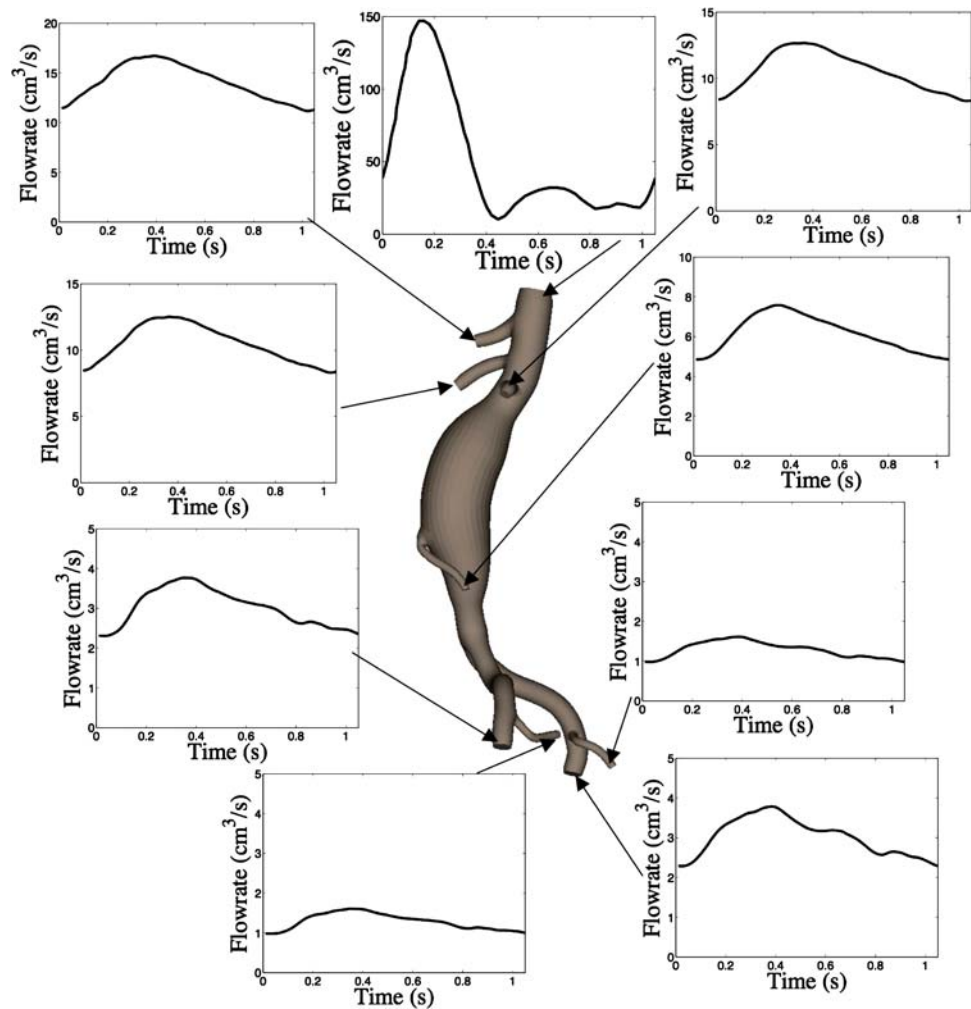
This results and the change of variables formula yields (9).

In the above we have utilized the commutativity of pull-back and exterior differentiation, and the fact that the exterior derivative of a 4-form, closed in four dimensions, is zero. That  $\mathcal{L}_{\gamma_y^{(4)}} dQ_y = \nabla_y^{(4)} \cdot \gamma_y^{(4)} dQ_y$  can be proved by assuming cartesian coordinates on  $\mathbb{R}^4 \supset Q_y$  and  $dQ_y = dy_0 \wedge dy_1 \wedge dy_2 \wedge dy_3$ , where  $\wedge$  is the wedge product. Likewise, the same construct can be used to prove  $\mathcal{L}_{\gamma_x^{(4)}} dQ_x = \nabla_x^{(4)} \cdot \gamma_x^{(4)} dQ_x$ . Curvilinear spatial coordinates can be accommodated by using the usual tensor transformation formulas on these coordinates (see Marsden and Hughes [47]). The time coordinate is unaffected in this case.

**Remark A.1** With differential forms, correct boundary integral expressions can be obtained without the necessity of unit normal vectors by using Stokes theorem and the change of



**Fig. 24** Flow in a patient-specific abdominal aorta with aneurysm. Flow rate distribution among the arterial branches during a heart cycle



variables formula. For example,

$$\begin{aligned}
 \int_{\partial Q_y} \mathbf{i}_{\mathbf{y}^{(4)}} dQ_y &= \int_{Q_y} d(\mathbf{i}_{\mathbf{y}^{(4)}} dQ_y) \\
 &= \int_{Q_y} \hat{\boldsymbol{\phi}}^{(4)} * d(\mathbf{i}_{\mathbf{y}^{(4)}} dQ_x) \\
 &= \int_{\hat{\boldsymbol{\phi}}^{(4)}(Q_y)} d(\mathbf{i}_{\mathbf{y}^{(4)}} dQ_x) \\
 &= \int_{Q_x} d(\mathbf{i}_{\mathbf{y}^{(4)}} dQ_x) \\
 &= \int_{\partial Q_x} \mathbf{i}_{\mathbf{y}^{(4)}} dQ_x. \quad (\text{A.4})
 \end{aligned}$$

**Remark A.2** The notations  $dQ_x$  and  $dQ_y$  are used under the integration sign in the main body of the paper, in contrast with the differential form notations to represent volume elements,

$dQ_x$  and  $dQ_y$ , respectively, in keeping with the standard usage.

## References

1. Abedi P, Patracovici B, Haber RB (2006) A spacetime discontinuous Galerkin method for linearized elastodynamics with element-wise momentum balance. *Comput Methods Appl Mech Eng* 195:3247–3273
2. Akkerman I, Bazilevs Y, Calo VM, Hughes TJR, Hulshoff S (2008) The role of continuity in residual-based variational multiscale modeling of turbulence. *Comput Mech* 41:371–378
3. Bazilevs Y, Calo VM, Zhang Y, Hughes TJR (2006) Isogeometric fluid-structure interaction analysis with applications to arterial blood flow. *Comput Mech* 38:310–322
4. Bazilevs Y, Calo VM, Cottrell JA, Hughes TJR, Reali A, Scovazzi G (2007) Variational multiscale residual-based turbulence modeling for large eddy simulation of incompressible flows. *Comput Methods Appl Mech Eng* 197:173–201
5. Bazilevs Y, Beiraoda Veiga L, Cottrell JA, Hughes TJR, Sangalli G (2006) Isogeometric analysis: approximation, stability and error estimates for  $h$ -refined meshes. *Math Models Methods Appl Sci* 16:1031–1090



6. Bazilevs Y, Hughes TJR (2007) Weak imposition of Dirichlet boundary conditions in fluid mechanics. *Comput Fluids* 36:12–26
7. Bazilevs Y, Michler C, Calo VM, Hughes TJR (2007) Weak Dirichlet boundary conditions for wall-bounded turbulent flows. *Comput Methods Appl Mech Eng* 196:4853–4862
8. Bishop R, Goldberg S (1980) *Tensor analysis on manifolds*. Dover, New York
9. Brezzi F, Fortin M (1991) *Mixed and hybrid finite element methods*. Springer, Berlin
10. Brooks AN, Hughes TJR (1982) Streamline upwind/Petrov-Galerkin formulations for convection dominated flows with particular emphasis on the incompressible Navier–Stokes equations. *Comput Methods Appl Mech Eng* 32:199–259
11. Calo VM (2004) Residual-based multiscale turbulence modeling: finite volume simulation of bypass transition. Ph.D. Thesis, Department of Civil and Environmental Engineering, Stanford University
12. Chung J, Hulbert GM (1993) A time integration algorithm for structural dynamics with improved numerical dissipation: The generalized- $\alpha$  method. *J Appl Mech* 60:371–75
13. Cottrell JA, Reali A, Bazilevs Y, Hughes TJR (2006) Isogeometric analysis of structural vibrations. *Comput Methods Appl Mech Eng* 195:5257–5297
14. Cottrell JA, Reali A, Hughes TJR (2007) Studies of refinement and continuity in isogeometric structural analysis. *Comput Methods Appl Mech Eng* 196:4160–4183
15. Dettmer W, Perić D (2006) A computational framework for fluid-structure interaction: finite element formulation and applications. *Comput Methods Appl Mech Eng* 195:5754–5779
16. Elguedj T, Bazilevs Y, Calo VM, Hughes TJR (2008) B-bar and F-bar projection methods for nearly incompressible linear and nonlinear elasticity and plasticity using higher-order NURBS elements. *Comput Methods Appl Mech Eng* 197:2732–2762
17. Farhat C, Geuzaine P, Grandmont C (2001) The discrete geometric conservation law and the nonlinear stability of ALE schemes for the solution of flow problems on moving grids. *J Comput Phys* 174(2):669–694
18. Farhat C, van der Zee K, Geuzaine P (2006) Provably second-order time-accurate loosely-coupled solution algorithms for transient nonlinear computational aeroelasticity. *Comput Methods Appl Mech Eng* 195:1973–2001
19. Fernandez MA, Moubachir M (2005) A Newton method using exact jacobians for solving fluid-structure coupling. *Comput Struct* 83:127–142
20. Figueroa A, Vignon-Clementel IE, Jansen KE, Hughes TJR, Taylor CA (2006) A coupled momentum method for modeling blood flow in three-dimensional deformable arteries. *Comput Methods Appl Mech Eng* 195:5685–5706
21. Flanders H (1963) *Differential forms with applications to the physical sciences*. Academic Press, London
22. Formaggia L, Nobile F (2005) Stability analysis of second-order time accurate schemes for ALE-FEM. *Comput Methods Appl Mech Eng* 193:4097–4116
23. Guillemin V, Pollack A (1974) *Differential topology*. Prentice-Hall, Englewood Cliffs
24. Heil M, Hazel J, Boyle J (2008) Solvers for large-displacement fluid-structure interaction problems: segregated vs. monolithic approaches. *Comput Mech*. doi:10.1007/s00466-008-0270-6
25. Heywood JG, Rannacher R, Turek S (1996) Artificial boundaries and flux and pressure conditions for the incompressible Navier-Stokes equations. *Int J Numer Methods Fluids* 22:325–352
26. Holzapfel GA (2004) Computational biomechanics of soft biological tissue. In: Stein E, De Borst R, Hughes TJR (eds) *Encyclopedia of computational mechanics, Solids and structures*, chap 18, vol 2. Wiley, London
27. Holzapfel GA (2000) *Nonlinear solid mechanics, a continuum approach for engineering*. Wiley, Chichester
28. Hughes TJR (2000) *The finite element method: linear static and dynamic finite element analysis*. Dover Publications, Mineola
29. Hughes TJR, Calo VM, Scovazzi G (2004) Variational and multiscale methods in turbulence. In: Gutkowski W, Kowalewski TA (eds) *In Proceedings of the XXI International Congress of Theoretical and Applied Mechanics (IUTAM)*, Kluwer, pp 153–163
30. Hughes TJR, Cottrell JA, Bazilevs Y (2005) Isogeometric analysis: CAD, finite elements, NURBS, exact geometry, and mesh refinement. *Comput. Methods Appl Mech Eng* 194:4135–4195
31. Hughes TJR, Hulbert GM (1988) Space-time finite element methods for elastodynamics: formulations and error estimates. *Comput Methods Appl Mech Eng* 66:339–363
32. Hughes TJR, Liu WK, Zimmermann TK (1981) Lagrangian–Eulerian finite element formulation for incompressible viscous flows. *Comput Methods Appl Mech Eng* 29:329–349
33. Hughes TJR, Wells GN (2005) Conservation properties for the Galerkin and stabilised forms of the advection-diffusion and incompressible Navier-Stokes equations. *Comput Methods Appl Mech Eng* 194:1141–1159
34. Hulbert GM, Hughes TJR (1990) Space-time finite element methods for second order hyperbolic equations. *Comput Methods Appl Mech Eng* 84:327–348
35. Idelsohn SR, Oñate E, Del Pin F, Calvo N (2006) Fluid-structure interaction using the particle finite element method. *Comput Methods Appl Mech Eng* 195:2100–2123
36. Jansen KE, Whiting CH, Hulbert GM (1999) A generalized- $\alpha$  method for integrating the filtered Navier-Stokes equations with a stabilized finite element method. *Comput Methods Appl Mech Eng* 190:305–319
37. Johnson AA, Tezduyar TE (1994) Mesh update strategies in parallel finite element computations of flow problems with moving boundaries and interfaces. *Comput Methods Appl Mech Eng* 119:73–94
38. Johnson AA, Tezduyar TE (1997) Parallel computation of incompressible flows with complex geometries. *Int J Numer Methods Fluids* 24:1321–1340
39. Johnson AA, Tezduyar TE (1999) Advanced mesh generation and update methods for 3D flow simulations. *Comput Mech* 23:130–141
40. Johnson C (1987) *Numerical solution of partial differential equations by the finite element method*. Cambridge University Press, Sweden
41. Johnson C, Nävert U, Pitkäntä J (1984) Finite element methods for linear hyperbolic problems. *Comput Methods Appl Mech Eng* 45:285–312
42. Küttler U, Förster C, Wall WA (2006) A solution for the incompressibility dilemma in partitioned fluid-structure interaction with pure Dirichlet fluid domains. *Comput Mech* 38:417–429
43. Kuhl E, Hulshoff S, de Borst R (2003) An arbitrary Lagrangian Eulerian finite element approach for fluid-structure interaction phenomena. *Int J Numer Methods Eng* 57:117–142
44. Lang S (1972) *Differential manifolds*. Addison-Wesley, Reading
45. Lang S (1995) *Differential and riemannian manifolds (graduate texts in mathematics, vol. 160)*. Springer, Heidelberg
46. Le Tallec P, Mouro J (2001) Fluid structure interaction with large structural displacements. *Comput Methods Appl Mech Eng* 190:3039–3068
47. Marsden JE, Hughes TJR (1993) *Mathematical foundations of elasticity*. Dover Publications Inc., New York
48. Masud A, Hughes TJR (1997) A space-time Galerkin/least-squares finite element formulation of the Navier-Stokes equations for moving domain problems. *Comput Methods Appl Mech Eng* 148:91–126

49. Michler C, van Brummelen EH, de Borst R (2006) Error-amplification analysis of subiteration-preconditioned GMRES for fluid-structure interaction. *Comput Methods Appl Mech Eng* 195:2124–2148
50. Michler C, van Brummelen EH, Hulshoff SJ, de Borst R (2003) The relevance of conservation for stability and accuracy of numerical methods for fluid-structure interaction. *Comput Methods Appl Mech Eng* 192:4195–4215
51. Nobile F (2001) Numerical Approximation of Fluid-Structure Interaction Problems with Application to Haemodynamics. Ph.D. Thesis, EPFL
52. Piperno S, Farhat C (2001) Partitined procedures for the transient solution of coupled aeroelastic problems. Part II: Energy transfer analysis and three-dimensional applications. *Comput Methods Appl Mech Eng* 190:3147–3170
53. Piperno S, Farhat C, Larrourou B (1995) Partitined procedures for the transient solution of coupled aeroelastic problems. Part I: Model problem, theory and two-dimensional application. *Comput Methods Appl Mech Eng* 124:79–112
54. Saad Y, Schultz MH (1986) GMRES: A generalized minimal residual algorithm for solving nonsymmetric linear systems. *SIAM J Sci Stat Comput* 7:856–869
55. Simo JC, Hughes TJR (1998) Computational inelasticity. Springer, New York
56. Babuška I (1973) The finite element method with Lagrange multipliers. *Numer Math* 20:179–192
57. Spivak M (1965) Calculus on manifolds. Benjamin, New York
58. Stein K, Tezduyar T, Benney R (2003) Mesh moving techniques for fluid-structure interactions with large displacements. *J Appl Mech* 70:58–63
59. Stein K, Tezduyar TE, Benney R (2004) Automatic mesh update with the solid-extension mesh moving technique. *Comput Methods Appl Mech Eng* 193:2019–2032
60. Texas Advanced Computing Center (TACC). <http://www.tacc.utexas.edu>
61. Taylor CA, Hughes TJR, Zarins CK (1998) Finite element modeling of blood flow in arteries. *Comput Methods Appl Mech Eng* 158:155–196
62. Taylor CA, Hughes TJR, Zarins CK (1998) Finite element modeling of three-dimensional pulsatile flow in the abdominal aorta: relevance to atherosclerosis. *Ann Biomed Eng* 26:975–987
63. Taylor CA, Hughes TJR, Zarins CK (1999) Effect of exercise on hemodynamic conditions in the abdominal aorta. *J Vasc Surg* 29:1077–1089
64. Tezduyar TE, Behr M, Liou J (1992) A new strategy for finite element computations involving moving boundaries and interfaces. The deforming-spatial-domain/space-time procedure. I. The concept and the preliminary numerical tests. *Comput Methods Appl Mech Eng* 94:339–351
65. Tezduyar TE, Behr M, Mittal S, Liou J (1992) A new strategy for finite element computations involving moving boundaries and interfaces. The deforming-spatial-domain/space-time procedure. II. Computation of free-surface flows, two-liquid flows, and flows with drifting cylinders. *Comput Methods Appl Mech Eng* 94:353–371
66. Tezduyar TE, Sathe S (2007) Modelling of fluid-structure interactions with the space-time finite elements: solution techniques. *Int J Numer Methods Fluids* 54:855–900
67. Tezduyar TE, Sathe S, Cragin T, Nanna B, Conklin BS, Pausewang J, Schwaab M (2007) Modelling of fluid-structure interactions with the space-time finite elements: Arterial fluid mechanics. *Int J Numer Methods Fluids* 54:901–922
68. Tezduyar TE, Sathe S, Schwaab M, Conklin BS (2008) Arterial fluid mechanics modeling with the stabilized space-time fluid-structure interaction technique. *Int J Numer Methods Fluids* 57:601–629
69. Tezduyar TE (2003) Computation of moving boundaries and interfaces and stabilization parameters. *Int J Numer Methods Fluids* 43:555–575
70. Tezduyar TE, Behr M, Mittal S, Johnson AA (1992) Computation of unsteady incompressible flows with the stabilized finite element methods—space-time formulations, iterative strategies and massively parallel implementations. In: *New methods in transient analysis, pVP, vol 246/AMD, vol 143*. ASME, New York, pp 7–24
71. Tezduyar TE, Sathe S, Keedy R, Stein K (2006) Space-time finite element techniques for computation of fluid-structure interactions. *Comput Methods Appl Mech Eng* 195:2002–2027
72. Vignon-Clementel IE, Figueroa CA, Jansen KE, Taylor CA (2006) Outflow boundary conditions for three-dimensional finite element modeling of blood flow and pressure in arteries. *Comput Methods Appl Mech Eng* 195:3776–3796
73. Wall W (1999) Fluid-Struktur-Interaktion mit stabilisierten Finiten Elementen. Ph.D. Thesis, Institut für Baustatik, Universität Stuttgart
74. Zhang Y, Bazilevs Y, Goswami S, Bajaj C, Hughes TJR (2007) Patient-specific vascular NURBS modeling for isogeometric analysis of blood flow. *Comput Methods Appl Mech Eng* 196:2943–2959